JAEA-Review
2008-040

JAEA-Review

Studies of Super-critical CO_2 Gas Turbine Power Generation Fast Reactor
(Contract Research, Translated Document)

(Eds.) Naoyuki KISOHARA, Shoji KOTAKE and Toshihiko SAKAMOTO

FBR Design Group
Advanced Nuclear System Research and Development Directorate

August 2008
Japan Atomic Energy Agency
日本原子力研究開発機構

本レポートは独立行政法人日本原子力研究開発機構が不定期に発行する成果報告書です。
本レポートの入手並びに著作権利用に関するお問い合わせは、下記あてにお問い合わせ下さい。
なお、本レポートの全文は日本原子力研究開発機構ホームページ（http://www.jaea.go.jp）
より発信されています。

独立行政法人日本原子力研究開発機構　研究技術情報部　研究技術情報課
〒319-1195　茨城県那珂郡東海村白方白根2番地4
電話029-282-6387, Fax 029-282-5920, E-mail:ird-support@jaea.go.jp

This report is issued irregularly by Japan Atomic Energy Agency
Inquiries about availability and/or copyright of this report should be addressed to
Intellectual Resources Section, Intellectual Resources Department,
Japan Atomic Energy Agency
2-4 Shirakata Shirane, Tokai-mura, Naka-gun, Ibaraki-ken 319-1195 Japan
Tel +81-29-282-6387, Fax +81-29-282-5920, E-mail:ird-support@jaea.go.jp

Studies of Super-critical CO_2 Gas Turbine Power Generation Fast Reactor
(Contract Research, Translated Document)

(Eds.) Naoyuki KISOHARA , Shoji KOTAKE and Toshihiko SAKAMOTO

FBR Cycle System Design Synthesis Unit
Advanced Nuclear System Research and Development Directorate
Japan Atomic Energy Agency
Oarai-machi, Higashiibaraki-gun, Ibaraki-ken

(Received June 12, 2008)

The following studies have been executed for a super-critical CO_2 turbine system of an SFR.

(1) Preliminary design of a SFR adopting a super-critical CO_2 cycle turbine

Preliminary system design of an SFR that adopts a super-critical CO_2 cycle turbine has been made. This SFR system eliminates secondary sodium circuits because of no sodium/water reaction. The power generation efficiency of the SFR has been estimated to be approximately 42%. Compared to a conventional SFR that adopts a steam Rankine cycle with secondary sodium circuits, the volume of the reactor building of the SC-CO_2 SFR has been reduced by 20%.

(2) Thermal-hydraulic experiment of a super-critical CO_2 cycle loop

A test loop that simulates a super-critical CO_2 whole cycle was fabricated. An electrical heater was used for a heat source of the test loop. The high efficiency of the compressor has been experimentally confirmed near the super-critical region. The temperature efficiencies of PCHE recuperators have been approximately 98-99% (hot leg), and the recuperators have exhibited high heat transfer performance. No significant flow instability has been observed in the test loop operation.

(3) Liquid sodium / CO_2 reaction test

Reaction tests have been executed by contacting a small amount of liquid sodium and CO_2 gas. Continuous sodium / CO_2 reactions with flame have occurred at the temperature higher than 570-580ºC. Main reaction products have been Na_2CO_3 and CO gas. The reaction heat has been also measured to be 50-75kJ/Na-mol.

(4) Computer code safety analysis for tube failure of sodium/CO_2 heat exchanger

Safety calculation has been done for one double ended guillotine tube failure (1 DEG) of a helical coil type sodium / CO_2 heat exchanger. The analysis has showed that the maximum pressure in the primary sodium circuit is 0.28MPa due to a gas leak. It has been, however, below the allowed level of the primary circuit structural integrity. The void reactivity of the reactor core has reached to 0.046$, and it has had no affect to the core safety. The layer thickness of the solid reaction product (Na_2CO_3) on fuel assemblies has been estimated to be at most 10mm, and no sodium flow blockage has occurred in the assemblies.

(5) Material test in super-critical CO_2

The corrosion and carbonization data of 12 Cr steel and 316FR have been acquired in high temperature super-critical CO_2 flow environment. No breakaway phenomenon has been observed in 5000hour test in both the materials. The corrosion of 12Cr steel has increased with parabolic curve, and the amount of the corrosion has been 170g/m^2 after an exposure of 600ºC -5000hours. The amount of corrosion of 316FR has been 5g/m^2 in the same test condition (600ºC-5000hours), and it has showed a good corrosion resistant property.

Keywords: Supercritical CO_2 Brayton Cycle, Sodium/CO_2 Reaction, PCHE, Recuperator, S-fin, SC-CO_2 Turbine, SC-CO_2 Compressor, 12Cr Steel Corrosion, 316FR Corrosion, Sodium Fast Reactor

---

This document is an English summary translation of the Innovative Nuclear Research and Development Program report "Studies of Super-critical CO_2 Gas Turbine Power Generation Fast Reactor". This program was funded by Ministry of Education, Culture, Sports, Science and Technology (MEXT). The study was performed by Tokyo Institute of Technology and Japan Atomic Energy Agency.

超臨界 CO_2 ガスタービン発電高速炉の技術開発

（受託研究・翻訳資料）

日本原子力研究開発機構
次世代原子力システム研究開発部門　設計統括ユニット
（編）木曽原 直之、小竹 庄司、阪本 善彦

（2008 年 6 月 12 日受理）

ナトリウム冷却型高速炉に適用する超臨界炭酸ガスタービンシステムについて、以下の研究が実施された。

(1) 超臨界炭酸ガスサイクルシステム SFR プラント予備設計

超臨界炭酸ガスタービンシステムを採用した SFR プラントの予備設計を行った。ナトリウム／水反応が無いため、2 次ナトリウム系削除型としている。本プラントの発電効率は約 42%であり、2 次ナトリウム系及び蒸気システムを保有する従来型 SFR に比べ、原子炉建屋容積は約 20%低減することがわかった。

(2) 超臨界炭酸ガスループ熱流動試験

超臨界炭酸ガスループ全体を模擬した試験装置を製作した。加熱源として電気ヒーターを使用した。臨界点近傍で圧縮機の高い効率が得られることを実験的に確認した。PCHE 再生熱交換器の温度効率は 98-99%であり、高い伝熱性能を示した。またループ運転性試験では、不安定な流動現象は発生しなかった。

(3) ナトリウム／炭酸ガス反応試験

少量の液体ナトリウムと炭酸ガスの接触試験により、反応の様相観察と反応生成物の分析を行った。ナトリウムと炭酸ガスの火炎を伴う連続的な反応は、570-580℃以上で発生し、反応生成物は Na_2CO_3 と CO であった。反応熱も測定し 50-75kJ/Na-mol であった。

(4) 伝熱管破損解析

シェル＆チューブ型（ヘリカルコイル型）ナトリウム／炭酸ガス熱交換器における、伝熱管 1 本ギロチン破断時の安全解析を行った。この結果、1 次ナトリウム系の圧力最大値は 0.28MPa で、構造健全性に影響ないこと、炉心への気泡移行による反応度上昇は、約 0.046$に達するが炉心に影響の無いことがわかった。反応生成物(Na_2CO_3)の燃料集合体への層厚みは最大でも約 10mm で、炉心閉塞には至らなかった。

(5) 超臨界炭酸ガス中材料試験

高温の超臨界炭酸ガス環境下において 316FR と 12Cr 鋼の腐食速度の基礎データを取得した。両材料とも 5000hr までの試験では剥離腐食は発生しなかった。12Cr 鋼の腐食は放物線状に増加し、600℃-5000hr で 180g/m^3 であった。一方、316FR の腐食量は同条件（600℃-5000hr）で 5g/m^3 であり、高い耐食性を示した。

本報告書は、革新的原子力システム研究開発事業の報告書『超臨界 CO_2 ガスタービン発電高速炉の技術開発』を英訳（要約）したものである。この事業は文部科学省によって資金提供されたもので、研究は東京工業大学と日本原子力研究開発機構が実施した。
大洗研究開発センター（駐在）：〒311-1393　茨城県東茨城郡大洗町成田町 4002

This is a blank page.

Contents

目次

1. Foreword

A study of a super-critical (SC) CO_2 cycle turbine has been performed by Tokyo Institute of Technology since 1999 in Japan. At the early stage of the study, a preliminary SC-CO_2 turbine design was made, and a small-sized recuperator thermal-hydraulic performance was examined. A fundamental test also exhibited that a CO_2 compressor load was reduced near super-critical region. Compared to a helium gas Brayton cycle, the SC-CO_2 Brayton cycle attains high efficiency because of the compressor load reduction. The efficiency of the SC-CO_2 cycle is almost equivalent to that of a steam Rankine cycle. In addition to that, the system of the super-critical CO_2 cycle is much simpler than that of the steam cycle system. The contact of sodium/CO_2 is considered to be no severe reaction. Therefore, the application of the super-critical CO_2 turbine system to a sodium fast reactor (SFR) has been suggested in Japan.

A new SC-CO_2 study project started in the "Innovative Nuclear Research and Development Program" funded by Ministry of Education, Culture, Sports, Science and Technology (MEXT). This new study was executed by Tokyo Institute of Technology, Japan Atomic Energy Agency, Advanced Reactor Technology Co., Ltd, and Fuji Electric systems Co., Ltd, 2003 though 2005.

This report shows the plant system design of a SFR adopting a SC-CO_2 system, experimental results and computer code analysis of the new study. The SFR system eliminates secondary sodium circuits because of no sodium/water reaction. The SFR system design and components sizing have been made to estimate the volume of the reactor building. Safety was evaluated for a CO_2 gas leak by a computer code analysis. Thermal-hydraulic experiment of a super-critical CO_2 cycle loop, liquid sodium / CO_2 reaction test and material test in super-critical CO_2 flow condition were executed to obtain fundamental data.

2. Preliminary design of SFR plant system adopting SC-CO_2 turbine

2.1 Introduction

Preliminary designs of sodium/CO_2 heat exchangers, a SC-CO_2 turbine system and a sodium/CO_2 reaction mitigation system for an SFR were made. The purpose of these designs was to roughly estimate the volume of a SFR system adopting a SC-CO_2 turbine and to prepare system data for safety evaluation in case of CO_2 gas leak. The designs were based on an existing study of SFRs that have a steam cycle system.

2.2 Primary sodium circuit and SC-CO_2 loop

The conceptual design of the SFR that adopts a SC-CO_2 cycle is shown in Figs. 2-1 and 2-2. The main specifications of the SFR are presented in Table 2-1. The SFR is a loop type reactor that consists of two primary sodium circuits, two sodium / CO_2 heat exchangers (HX), and one SC-CO_2 turbine system.

Primary hot leg sodium enters two sodium / CO_2 heat exchangers via two hot leg sodium pipes. A primary mechanical sodium pump is installed in the HX. The sodium is heat-exchanged in the HXs, and it is transported by the pump to the reactor through the cold leg sodium pipe.

Two CO_2 gas pipes from the two HXs join to one CO_2 loop outside a containment vessel. In the SC-CO_2 cycle system, the CO_2 is circulated through a CO_2 turbine, a recuperator, coolers and compressors. A portion of CO_2 that has passed through the hot leg of the recuperator diverges from the main CO_2 loop and directly enters a by-pass compressor. The CO_2 that has passed through the by-pass compressor flows in the cold leg of the recuperator. The CO_2 in the main loop enters a low-pressure compressor and then a high-pressure compressor after passing through respective coolers, and then it flows in the cold leg of the recuperator. The CO_2 that has passed through the cold leg of the recuperator is transported to the HXs.

One DRACS in the reactor and two PRACSs in the HXs are provided as a decay heat removal system.

2.3 Sodium / CO_2 heat exchanger

Preliminary designs of two types of sodium/CO_2 heat exchangers (HX) were made to estimate the size and the heat transfer areas. One was of a helical-coil tube type, and the other was of a printed circuit heat exchanger (PCHE) type. Illustrations and the main specifications of these HXs are presented in Figs. 2-3 and 2-4, respectively. Both the components incorporate mechanical primary sodium pumps in the center.

Two shells (inner shell and outer shell) are installed in the helical-coil tube HX (Fig. 2-3). The helical coil tubes are located between the inner shell and the outer shell. Down-comer tubes which connect CO_2 inlet plenums and helical coil tubes are between the outer shell and a HX vessel. CO_2 gas enters down-comer tubes through the inlet plenums, and then flows to the bottom of the helical coil tubes. The CO_2 gas goes upward in the helical coil tubes. The sodium flows downward in the tube bundle region, and then it turns upward at the bottom of the bundle. The primary mechanical sodium pump is installed in the center of the HX to reduce the volume of the component. The pump conveys the sodium from the tube bundle to a sodium outlet of the HX. The CO_2 inlet and outlet are each divided into three plenums. This is for to ensure the structural integrity of tube-sheets by reducing their diameter.

The purpose of the PCHE type sodium/CO_2 HX is to reduce the CO_2 pressure drop and to reduce the HX size. Thermal-hydraulic characteristics were calculated by a multi-dimensional CFD (Computational Fluid Dynamics) code which determines cross section area and length of flow path. Sodium and CO_2 flow path arrangements and dimensions in the PCHE are shown in Fig. 2-4. The dimensions of the PCHE module were estimated to be W300mm, L500mm, and H5000mm, and one HX contains 30 PCHE modules. Compared with the helical coil type HX, the pressure drop of the PCHE is reduced from 1.57MPa (helical coil type) to 0.1MPa (PCHE), and the heat transfer area of the PCHE is decreased by 20%.

2.4 Sodium/CO_2 reaction mitigation system

The SC-CO_2 gas cycle system is connected to the primary sodium circuit. In case of tube failure, the leak must be detected and the sodium/CO_2 reaction must be terminated soon for plant safety. A Sodium/CO_2 reaction mitigation system for a tube failure of the helical coil type HX is shown in Fig. 2-5. Rupture disks (R/D) and a reaction products storage tank are prepared to avoid excessive pressure rising in the primary sodium circuit due to a CO_2 gas leak. R/D (1) and R/D (2) are installed on the cover gas (C/G) region of the HX and on the reaction products storage tank, respectively. The storage tank also functions as a sodium drain tank. CO_2 gas blow valves and CO_2 circuit isolation valves are prepared to stop the CO_2 leak to the sodium circuit.

A cylindrical barrage is provided on the bottom of the inner shell in the HXs. Since the sodium flow velocity in the tube bundle region is low (0.1-0.3m/sec), most of the CO_2 gas leaking into the sodium flow is blocked by the barrage and the gas goes up through the bundle region to the cover gas of the HX due to its buoyancy. The CO_2 gas, however, cannot be completely trapped by the barrage. A small amount of the CO_2 gas is considered to be flow toward the primary pump.

An anti-reverse valve is equipped on the cold leg sodium pipe to prevent sodium backward flow after a CO_2 gas leak.

Several kinds of sensors and detectors are provided for a CO_2 gas leak. Acoustic signals, rupture disk release signals, and pressure rising signals are generated in the leak detection system for the plant safety. Ultrasonic void detectors, oxygen meters, and CO meters are used for a CO_2 leak warning system.

2.5 Layout of plant system

Figure 2-6 shows the layout of a proposed SC-CO_2 turbine module. The module contains a generator, a turbine, compressors, a recuperator and coolers. The size of the SC-CO_2 turbine module is roughly estimated to determine the necessary reactor building size.

The layout of the main components in a reactor building is indicated in Fig 2-7. The components are arranged as compactly as possible to reduce the volume of the building. Safety and ease of maintenance and repair were taken into account in the component layout design. The facilities other than the main components were arranged based on previous SFR design studies. This layout of sodium main pipes and CO_2 pipes is tentative, and needs structural evaluations such as thermal expansion analysis in the future.

The rectangular containment vessel that includes the reactor vessel and the HXs is located in the middle of the reactor building. Two drain tanks are in the bottom of the containment vessel. The SC-CO_2 turbine module is placed to the east of the containment vessel. The CO_2 pipes that connect the HXs and the SC-CO_2 turbine module are arranged at the north and south side of the containment vessel. A fuel handling facility, a waste disposal system and a central control room are in the west side of the reactor building.

From the size of the components and the layout, the reactor building dimensions were estimated to be W56.6m x D51.0m x H67.9m, and its volume was $1.35x10^5m^3$.

2.6 Conclusions

The size of the reactor building was preliminarily estimated. Compared with a conventional SFR system that has a secondary sodium circuit and a steam cycle system, the size of the SFR that adopts an SC-CO_2 system is reduced by approximately 20%. As the design is in a preliminary stage, further study is needed for a more detailed estimation. Data on a sodium/CO_2 reaction mitigation system was prepared for a sodium/CO_2 reaction computer analysis. (The safety analysis is reported in Section 5.)

Table 2-1 Specifications of super-critical CO_2 cycle SFR

Rector type	Sodium cooled fast reactor adopting super-critical CO_2 cycle in secondary circuit
Thermal output	600MWth (Electrical output 250MWe)
Turbine	Supercritical CO_2 turbine
Power generation efficiency	42%
Loop number of cooling system	2 loops
Reactor outlet / inlet sodium temperature Rector sodium flow rate	550°C / 425°C 1.367×10^7kg/h
CO_2 turbine inlet temperature / pressure CO_2 flow rate	527°C / 20MPa 1.261×10^7kg/h
Sodium primary pump	Vertical mechanical pump
Sodium / CO_2 heat exchanger	Primary sodium pump and heat transfer tube integrated component
Decay heat removal system	2 PRACS and 1 DRACS

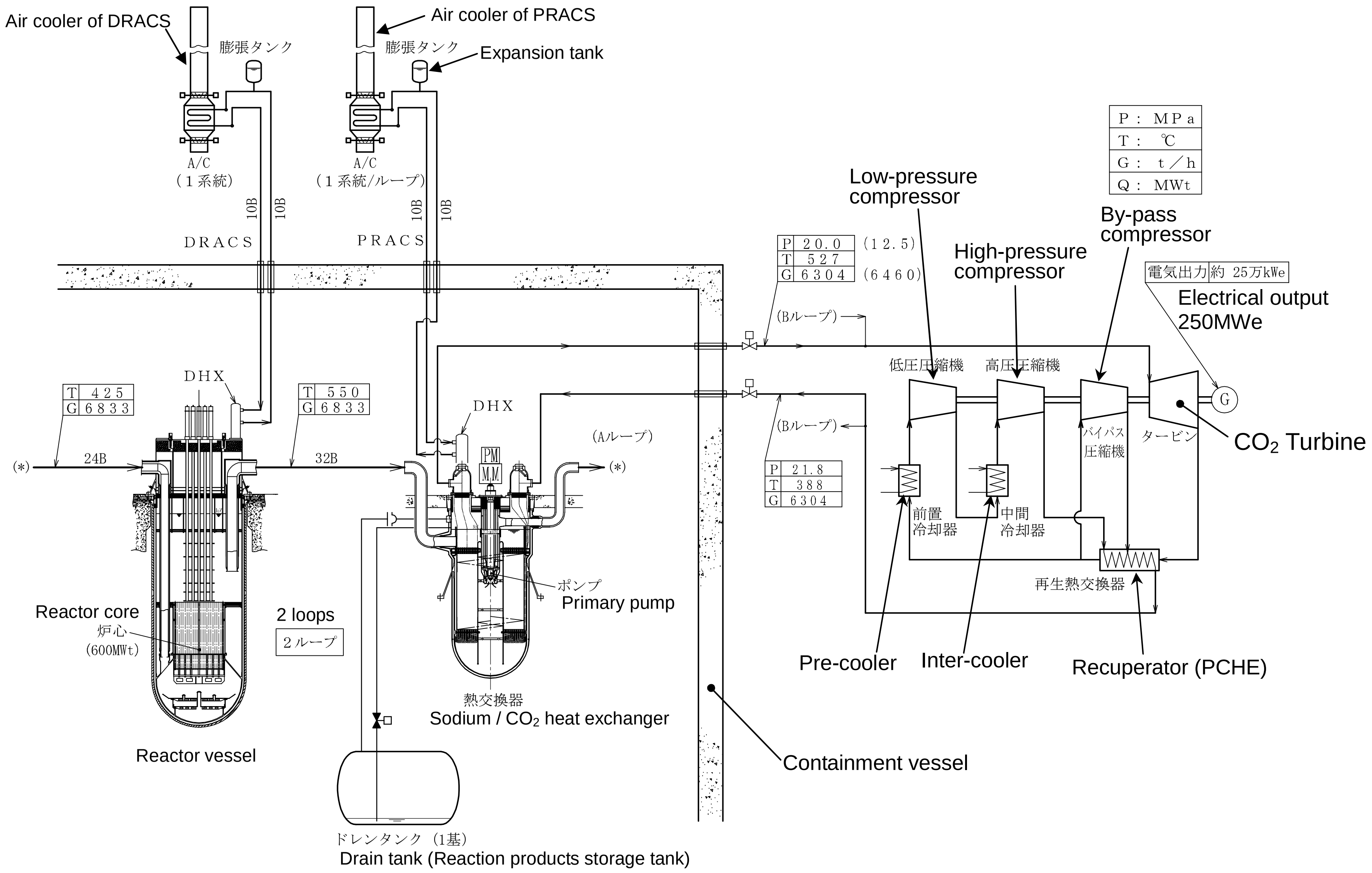

Fig. 2-1 Preliminary design of SFR adopting SC-CO_2 turbine system

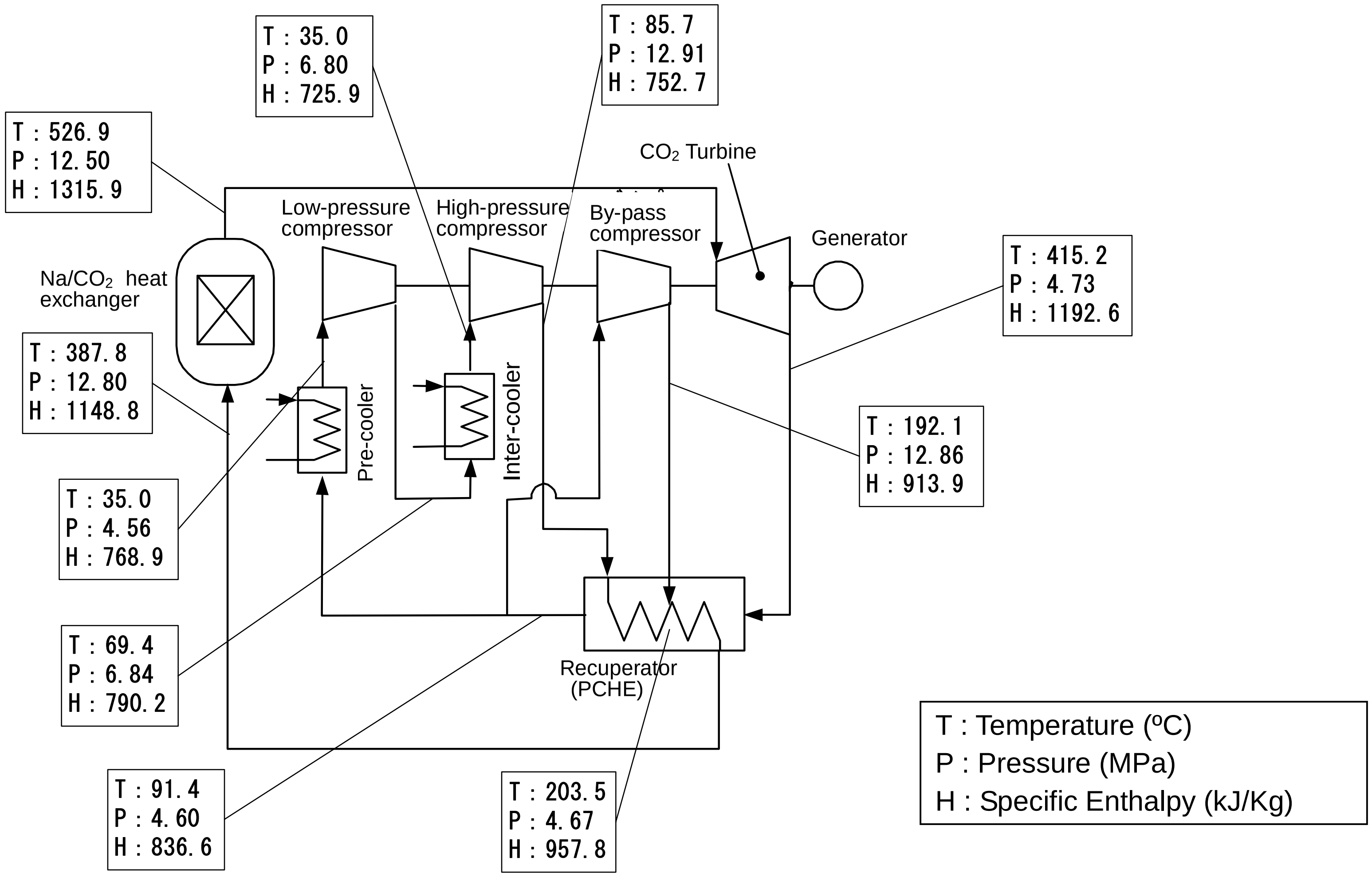

Fig. 2-2 Heat balance of SC-CO_2 cycle for SFR

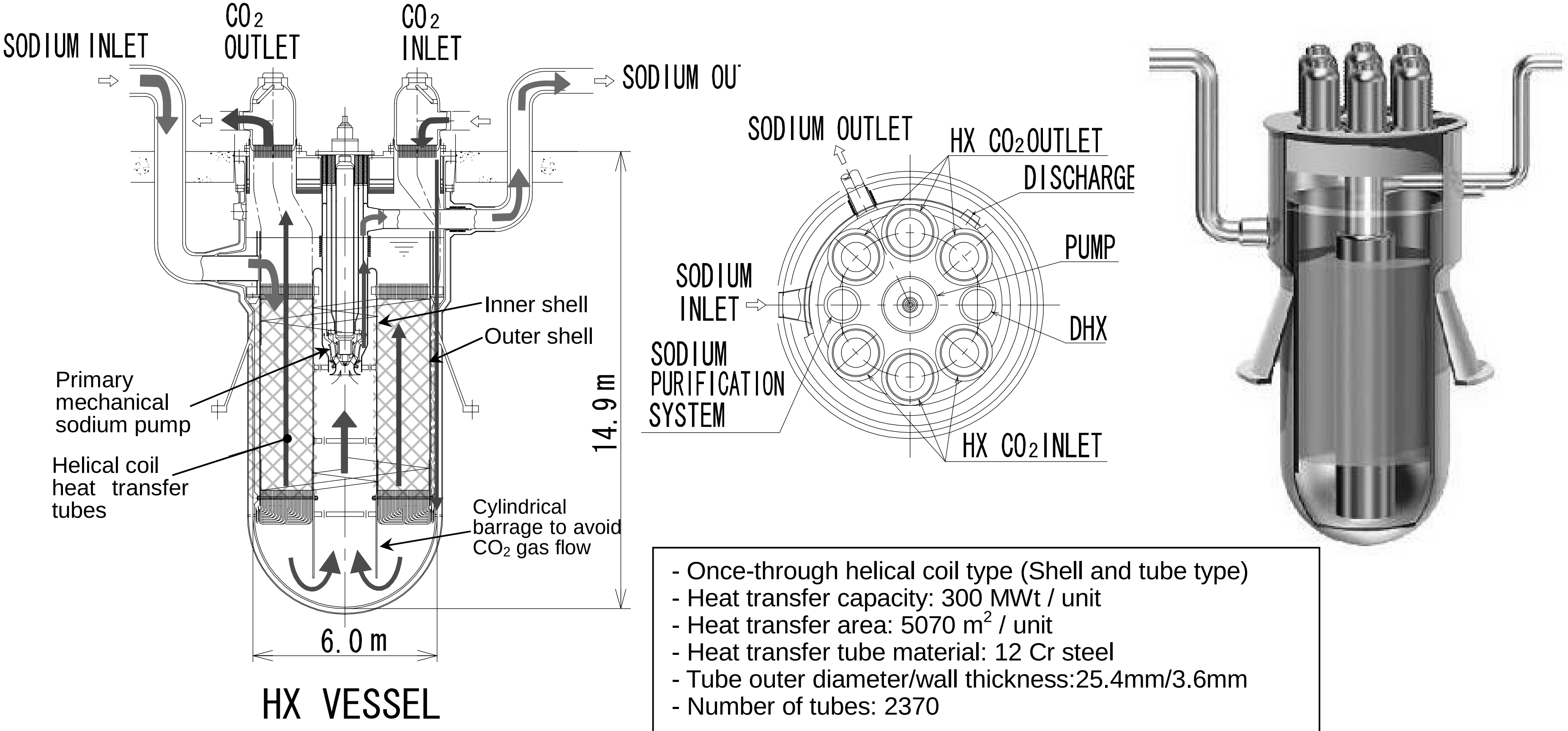

- Once-through helical coil type (Shell and tube type)
- Heat transfer capacity: 300 MWt / unit
- Heat transfer area: 5070 m^2 / unit
- Heat transfer tube material: 12 Cr steel
- Tube outer diameter/wall thickness:25.4mm/3.6mm
- Number of tubes: 2370

- Primary / secondary fluid: Sodium / CO_2
- CO_2 pressure (pressure drop): 20MPa (1.57 MPa)
- Sodium inlet / outlet temperature: 550°C/ 425°C
- CO_2 inlet / outlet temperature: 388°C/527°C
- Sodium / CO_2 flow rate: 6.83X10^6kg/hr / 6.30X10^6kg/hr

Fig. 2-3 Sodium/CO_2 helical coil shell and tube type heat exchanger

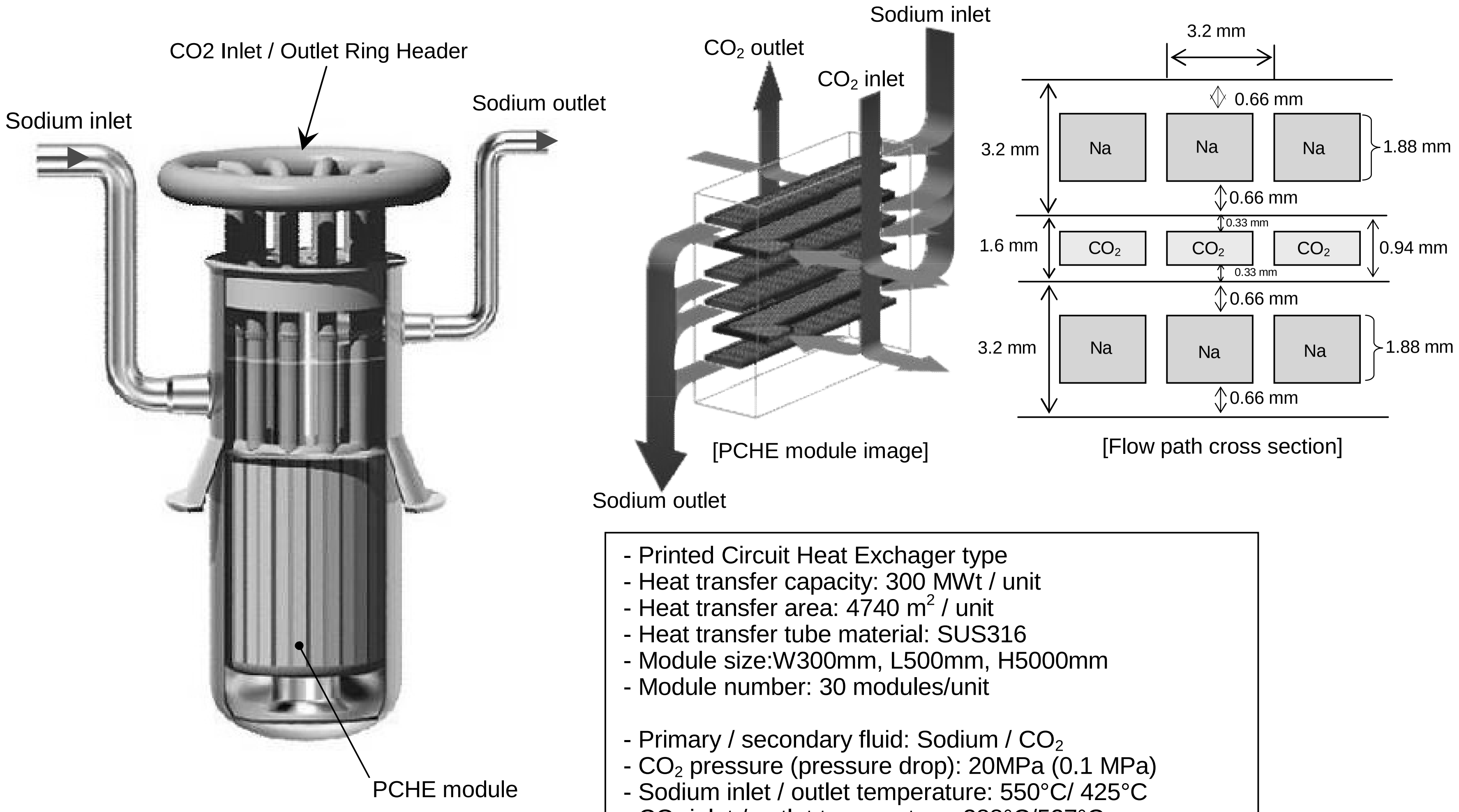

- Printed Circuit Heat Exchager type
- Heat transfer capacity: 300 MWt / unit
- Heat transfer area: 4740 m^2 / unit
- Heat transfer tube material: SUS316
- Module size:W300mm, L500mm, H5000mm
- Module number: 30 modules/unit

- Primary / secondary fluid: Sodium / CO$_2$
- CO$_2$ pressure (pressure drop): 20MPa (0.1 MPa)
- Sodium inlet / outlet temperature: 550°C/ 425°C
- CO$_2$ inlet / outlet temperature: 388°C/527°C
- Sodium / CO$_2$ flow rate: 6.83X10^{6}kg/hr / 6.30X10^{6}kg/hr

Fig. 2-4 Sodium/CO$_2$ Printed Circuit Heat Exchanger

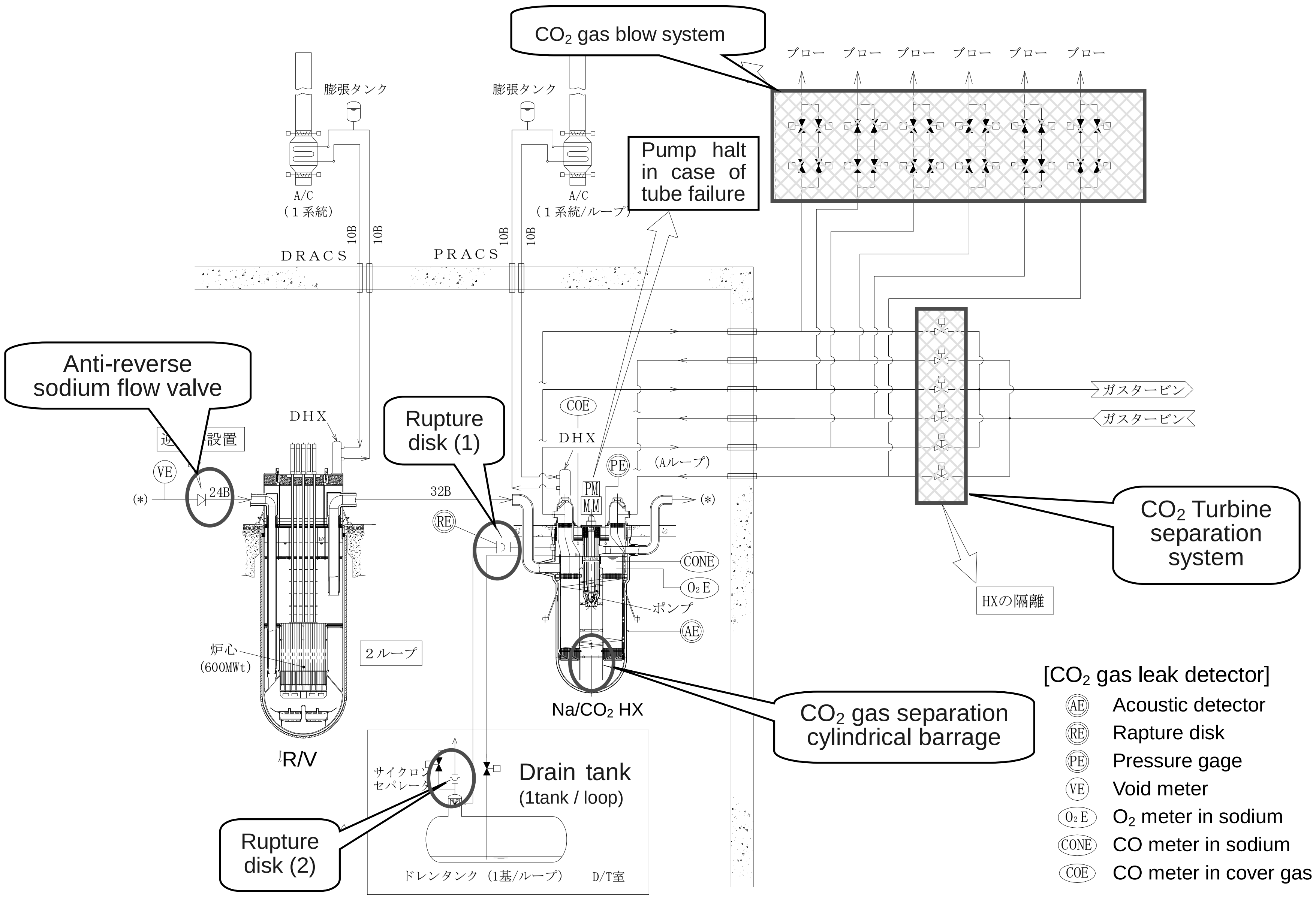

Fig. 2-5 Mitigation system for heat transfer tube failure

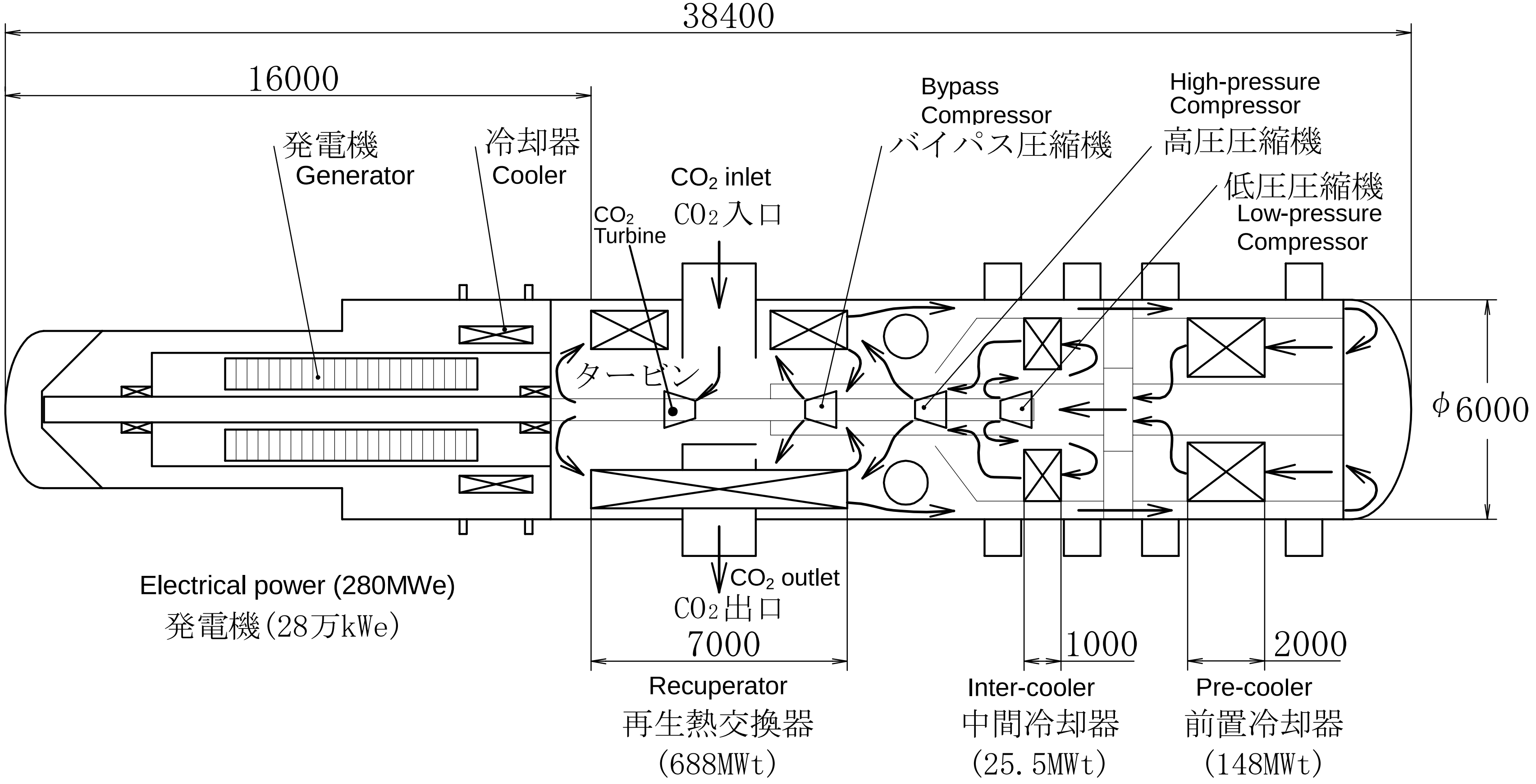

Fig. 2-6 SC-CO_2 turbine module

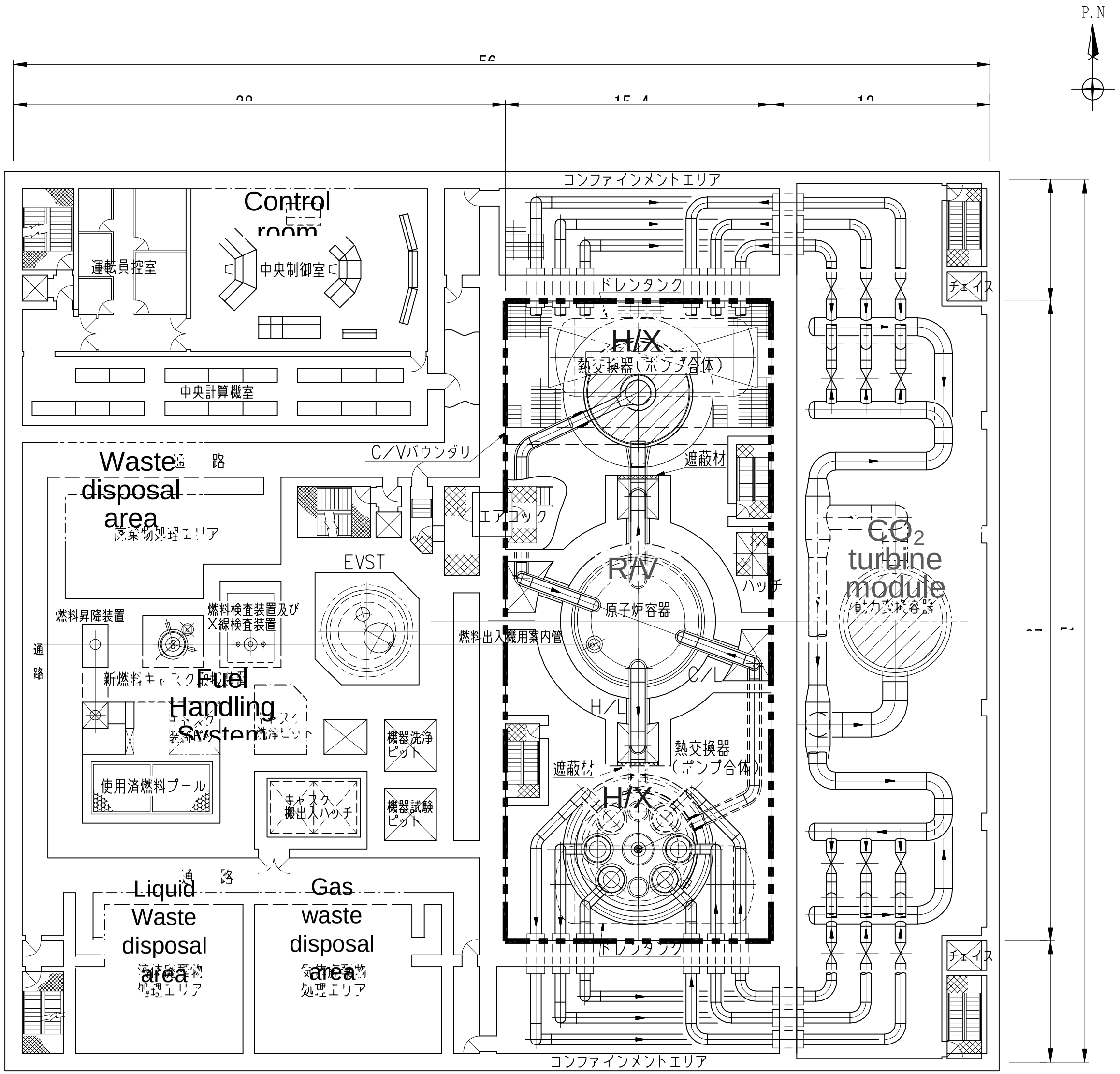

代表平面図

Fig. 2-7 Reactor building layout (Upper view)

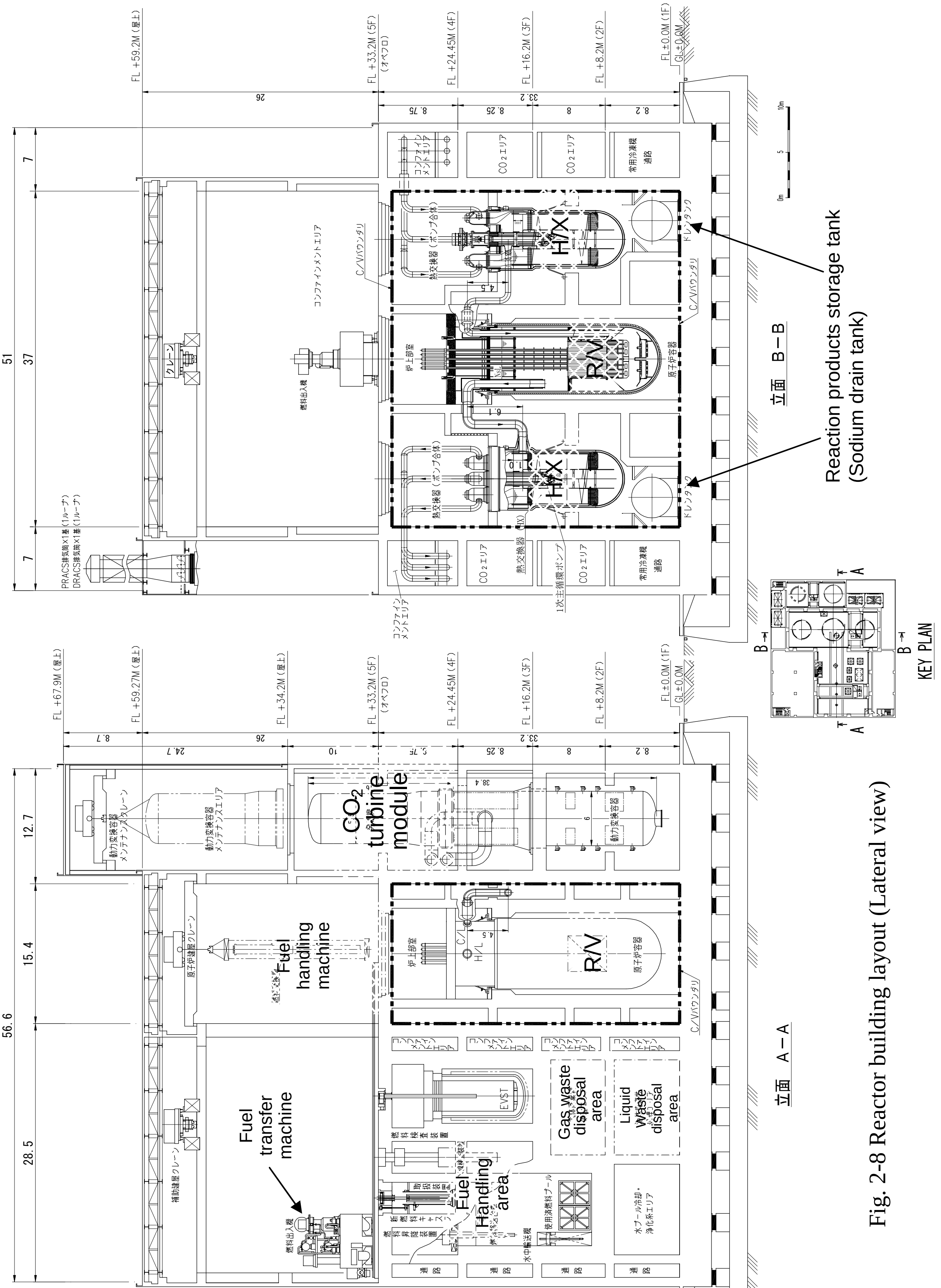

Fig. 2-8 Reactor building layout (Lateral view)

3. Thermal-hydraulic tests of super-critical CO_2 cycle

3.1 Introduction

A SC-CO_2 test loop that consisted of compressors, recuperators and coolers was fabricated to obtain fundamental data of the system performance. Although the test equipment is relatively small sized, all the main components of a SC-CO_2 cycle system were installed. The test has been executed to determine the thermal-hydraulic properties and efficiency of the SC-CO_2 cycle and the components.

3.2 Outline of tested devices

A schematic figure and an overall view of the SC-CO_2 cycle test loop are given in Figs. 3.1 and 3.2. The main components of the loop are three compressors, two recuperators (HX-3, 4), one pressure expander, an electrical heater (HX-5), a pre-cooler (HX-1), a cooler (HX-11), and an inter-cooler (HX-2). The compressors are a low pressure compressor, a high pressure compressor and a bypass compressor. The recuperators (HX-3, 4) are PCHE (Printed Circuit Heat Exchanger) types fabricated by etching and metal diffusion bonding techniques. The electrical heater which simulates a sodium/CO_2 heat exchanger generates 30kWth, approximately 1/20000 of the thermal

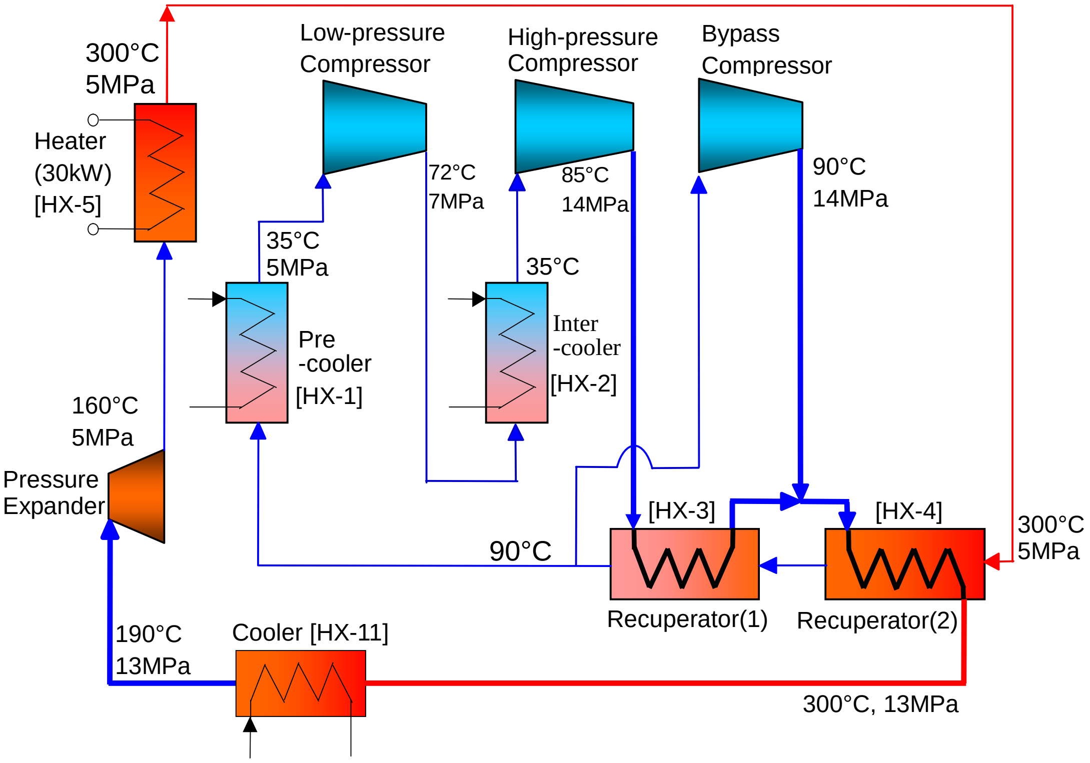

Red line: Hot leg,   Blue line: cold leg
Thick line: high pressure region, Thin line: low pressure region

Fig. 3.1 SC-CO_2 cycle test loop

capacity of the actual HX. The thermal capacity of HX-3 (recuperator 1) and HX-4 (recuperator 2) are 19kW and 21kW, respectively. The pressure expander simulates the decompression of a SC-CO_2 turbine. As the pressure expander can be used only under room temperature, a cooler (HX-11) is installed before the expander. (The pressure expander was not placed just after the heater.) The pre-cooler and the inter-cooler are the heat exchangers to approximate the CO_2 gas temperature to the super-critical condition.

The CO_2 heated by the heater(HX-5) enters the hot leg of the recuperators, and the hot CO_2 is heat-exchanged with the cold leg CO_2 here. The CO_2 cooled in the recuperators flows to the low pressure compressor and the high pressure compressor after passing through the pre-cooler and the inter-cooler, respectively. A portion of CO_2 branches away from the main CO_2 loop after passing through the recuperators, and directly flows into the by-pass compressor. The CO_2 that has passed through the compressors flows into the cold leg of the recuperators, and then is brought to the pressure expander after passing through the cooler (HX-1).

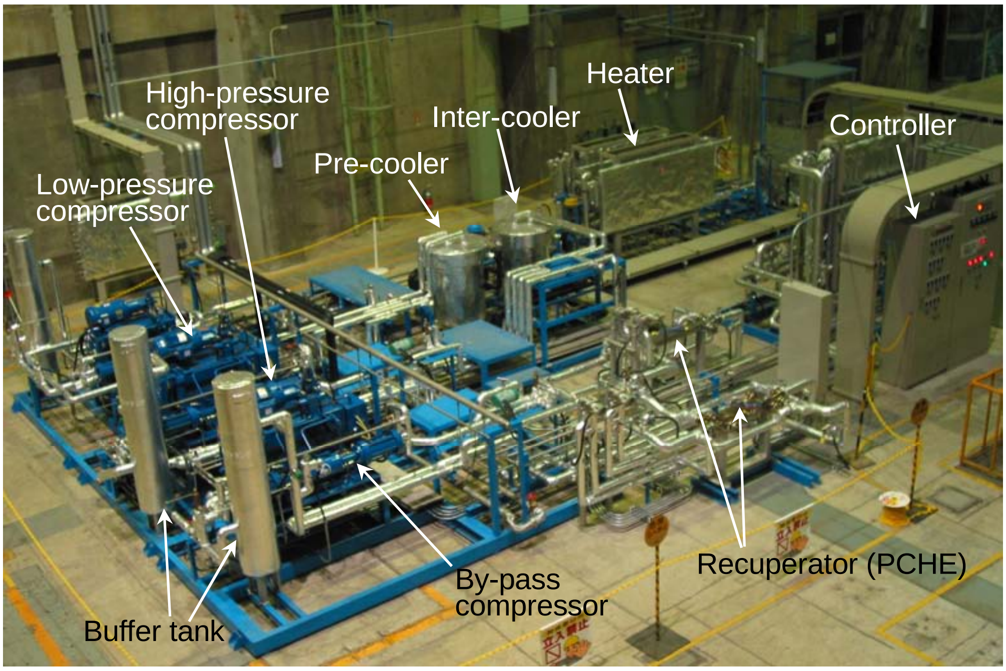

Fig.3.2 Overview of SC-CO_2 test loop

The purposes of the SC-CO_2 test loop are to confirm the followings:

- CO_2 compressor efficiency near the critical region
- PCHE recuperator thermal-hydraulic performance
- SC-CO_2 cycle operation stability.

3.3 Compressor efficiency tests

The reciprocating type CO_2 compressor shown in Fig. 3.3 was used in the test loop. Since a turbo machine compressor is made for high flow rate conditions, it cannot be applied in a test loop where the CO_2 flow rate is low (approx. 200~400kg/hr). The reciprocating type compressor generates flow fluctuations. Buffer tanks are equipped in the loop to decrease the fluctuations.

The ratio of inlet and outlet pressure (Po/Pi) of the compressor was set to be 1.7. The inlet and outlet temperatures are 35°C and 60°C, respectively. The CO_2 flow rate was maintained to be constant.

Table 3.1, Figs. 3.4 and 3.5 show the net power of the compressor used to compress CO_2. The test data were acquired at several points ranging from far from the super-critical region to near the super-critical region. The compressor net power can be calculated by subtracting the heat loss from the compressor electrical power. Table 3.1 and Fig. 3.4 show that the compressor net power decreased near the super-critical region. Comparing the net power at points where the outlet pressures were 5.8MPa (C-2-1) and 7.3MPa (C-2-4), it was reduced to approximately 1/2. Thus, it was experimentally confirmed that the CO_2 compression loss was lowered near the super-critical region.

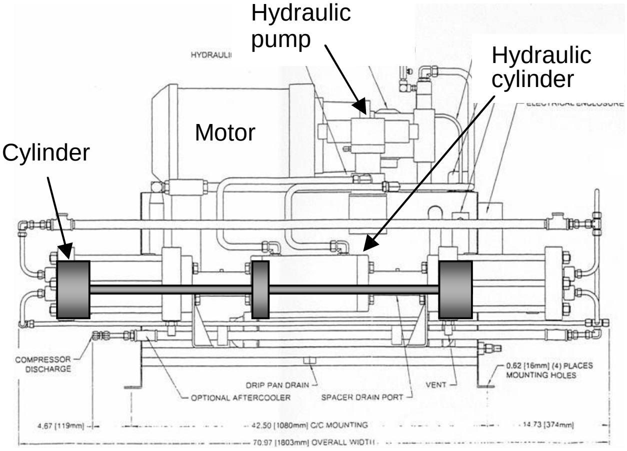

Stroke speed: 50spm
Rated pressure: 17.2MPa
Flow rate: $272Nm^3/h$
Cylinder: water cooling

Fig. 3.3 Reciprocating CO_2 Compressor

3.4 PCHE-type recuperator thermal hydraulic tests

(1) Specifications of recuperators

Two types of the recuperators were fabricated for the SC-CO_2 cycle tests. One was a zigzag fin type, and the other was an S-fin type (Fig. 3.6). The zigzag type was a conventional PCHE recuperator made by Heatric. Since the pressure drop of the conventional PCHE is relatively high due to its small flow diameter, a new S-fin type PCHE recuperator has been developed in Japan to reduce the pressure loss. [1]

Table3.1 High pressure compressor efficiency test result

Test No.	Inlet pressure MPa	Outlet pressure MPa	CO_2 flow rate kg/hr	Electrical power kW	Removal heat kW	Net power of the compressor kW
C-2-1	3.4	5.8	100.3	2.23	1.28	0.95
C-2-2	3.7	6.3	102.2	2.09	1.26	0.83
C-2-3	4.0	6.8	101.9	1.95	1.24	0.71
C-2-4	4.3	7.3	99.9	1.77	1.29	0.48

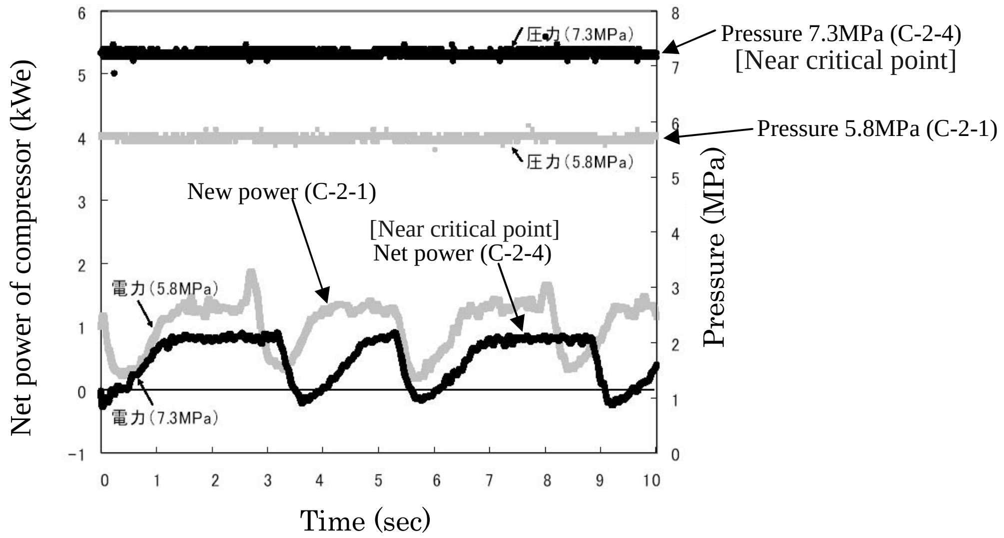

Fig. 3.4 Net power of high pressure compressor

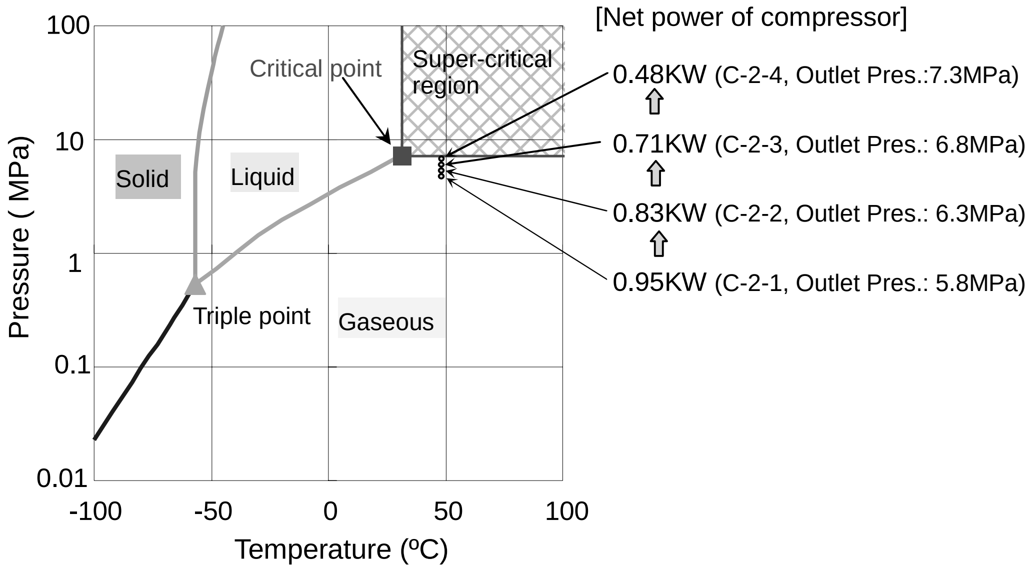

Fig. 3.5 High pressure compressor efficiency test result

Tables 3.2 and 3.3 give the main specifications of the zigzag fin type and S-fin type PCHE recuperators, respectively. The detail of the S-fin is shown in Fig. 3.7. Outside views of the PCHE test modules are given in Fig. 3.8.

3D computational fluid dynamic (CFD) analysis was employed to evaluate the thermal-hydraulic properties of several kinds of fin. Figure 3.9 shows the heat transfer performance and the pressure drop of an S-fin, a sine wave fin, a louver fin and a zigzag fin. The calculation revealed that the S-fin type was superior to the other type fins both for good thermal performance and for low pressure drop.

The CO_2 flow patterns in the zigzag fin and the S-fin are compared in Fig. 3.10. Eddy flows and local high flows were formed in the zigzag fin. These flow phenomena cause high pressure losses. The eddy flow disappeared and the CO_2 uniformly flowed in the S-fin. The CFD analysis predicted that the pressure drop of the S-fin PCHE is 1/6 of that of the zigzag fin PCHE. The analysis also showed that the heat transfer performance of the S-fin PCHE is almost the same as that of the zigzag fin PCHE.

Table 3.2 Specifications of Zigzag fin type recuperators (PCHE)

	HX-3	HX-4
Material	SUS316L	SUS316L
Plate thickness (mm)	1.63	1.63
PCHE size (mm)	100W×79H×896L	100W×109H×646L
Thermal capacity (kW)	21	19

Table 3.3 Specifications of S-fin type recuperators (PCHE)

	HX-3	HX-4
Material	SUS316L	SUS316L
Plate thickness (mm)	1.5/1.5	1.5/1.5
Plate number (hot leg / cold leg)	24/12	20/10
PCHE outside size (mm)	136W×64H×867L	136W×55H×867L
Flow cross section (hot leg / cold leg) (m^2)	$1.431/0.690\times10^{-3}$	$1.193/0.575\times10^{-3}$
Heat transfer surface (hot leg / cold leg) (m^2)	3.335/1.608	2.779/1.340
Equivalent hydro diameter (mm)	1.05	1.05
Thermal capacity (kW)	22	19

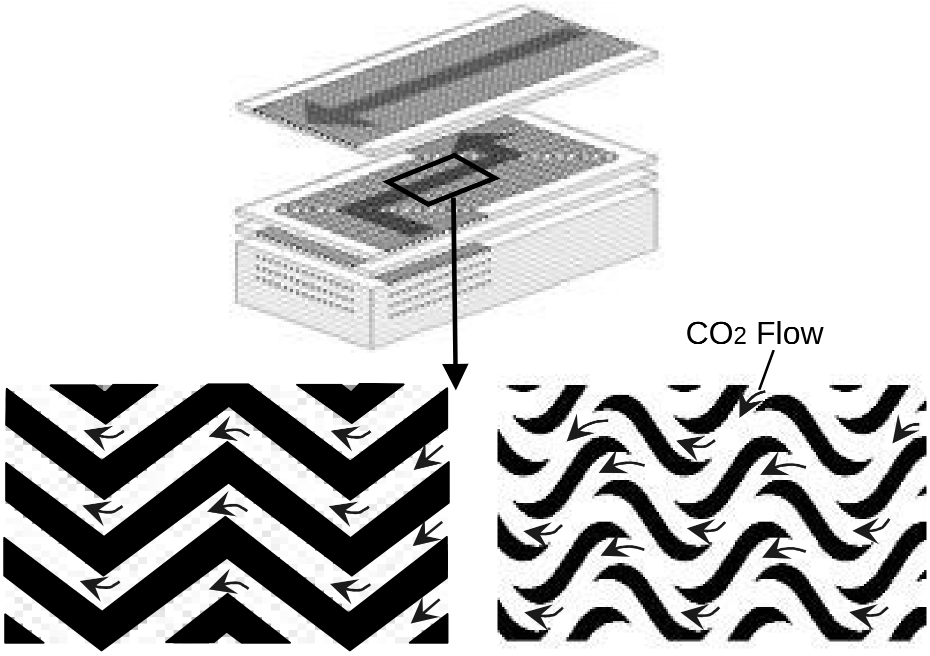

[Zigzag fin type]

[S-fin type]

Fig. 3.6 Fin shape of recuperatos

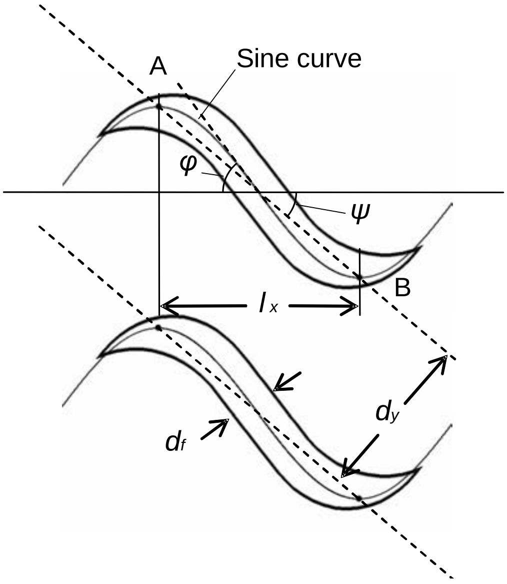

$\varphi = 52°$

$\psi = 38°$

$l_{AB} = 4.8$ mm

$l_x = 3.7825$ mm

$d_f = 0.8$ mm

$d_y = 2.7$ mm

Fig. 3.7 Detailed size of S-fin shape

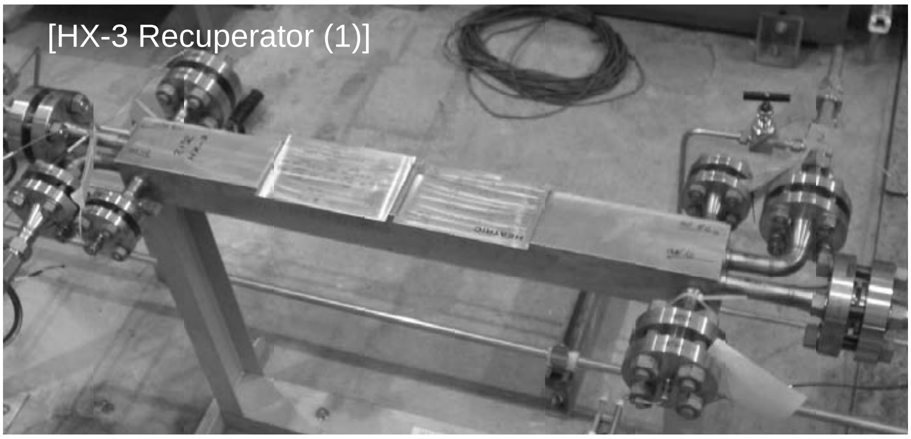

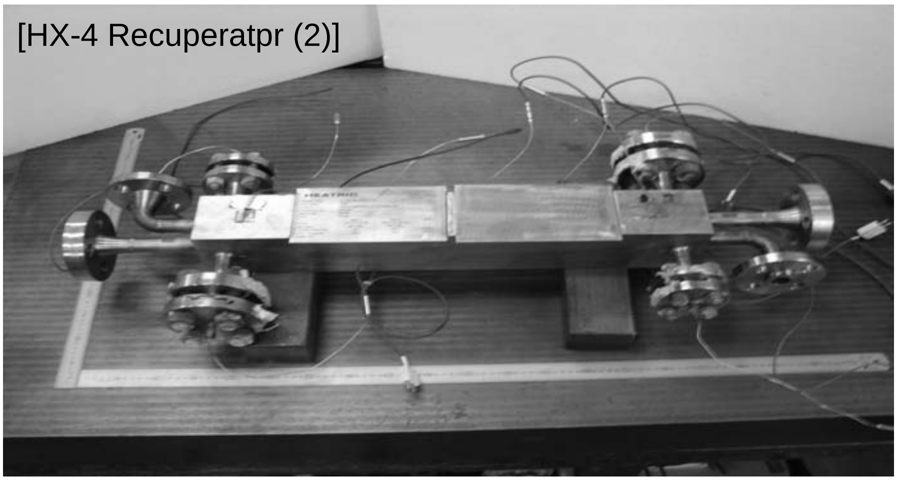

Fig. 3.8 Outside views of zigzag fin type PCHE recuperators

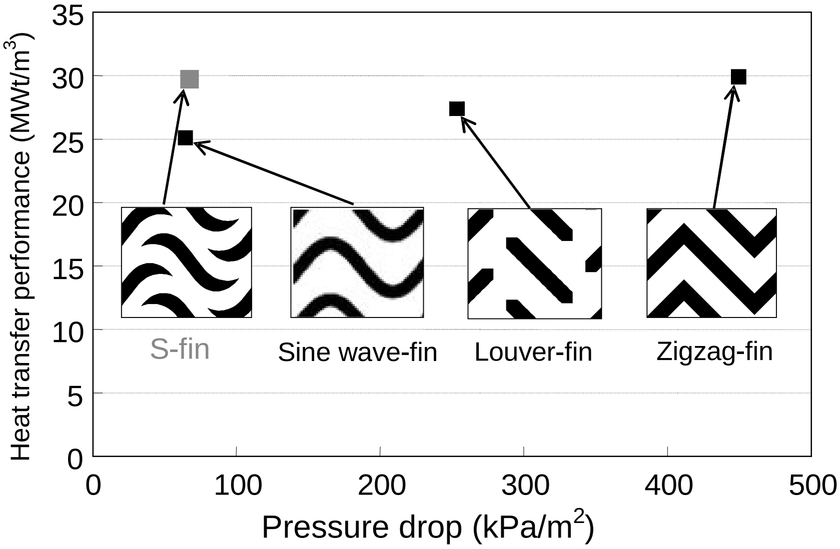

Fig. 3.9 Pressure loss and heat transfer performance of recuperator (Calculation results)

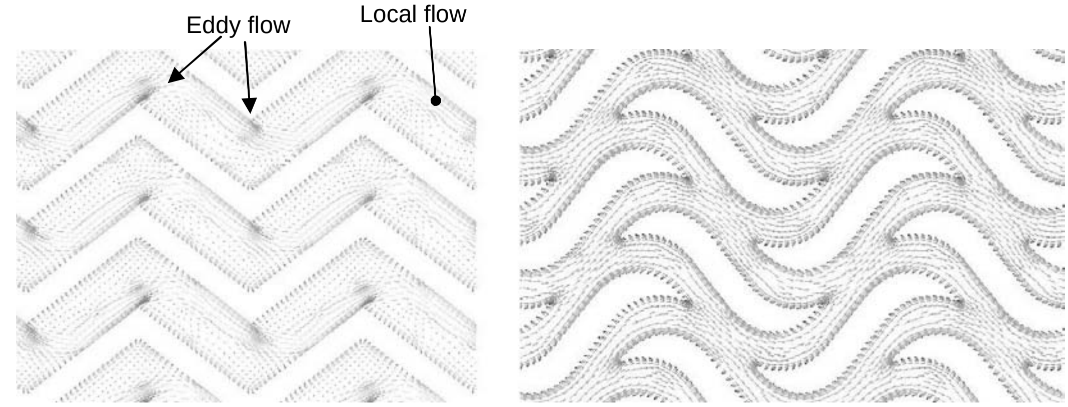

[Zigzag fin]

- Eddy flow at corners
- Local flow

[S-fin]

- Uniform flow

Fig. 3.10 Flow pattern in Zigzag-fin and S-fin (Calculation results)

(2) Definition of Reynolds number

Figure 3.11 shows the CO_2 temperature longitudinal distributions in the recuperator by 1D thermal-hydraulic calculation. The calculation was executed on the condition that the heat flux was constant in the longitudinal direction. The pressure gradient was assumed to be linearly distributed. Reynolds number, Prandtl number, thermal convection and CO_2 density of each calculation mesh cell can be obtained from these temperature and pressure distributions. The representative Reynolds number of the recuperators was defined as the average of each mesh cell Reynolds number.

The representative pressure loss coefficient was also obtained by averaging the pressure drop coefficient of each mesh cell. The pressure loss coefficient is defined by the following:

$$f_i = \Delta P_i \frac{2\rho}{G_i^2}\frac{D_i}{\Delta L_i}$$

ΔP : Pressure drop
ρ : CO_2 density
G : CO_2 mass flow
D : Equivalent diameter
ΔL : Flow path length.

The temperature efficiency ratios of the PCHE recuperators are defined by the formulas below.

Temperature efficiency ratio of hot leg : η_h

Temperature efficiency ratio of cold leg : η_c:

$$\eta_h = \frac{T_{hi} - T_{ho}}{T_{hi} - T_{ci}} \qquad \eta_c = \frac{T_{co} - T_{ci}}{T_{hi} - T_{ci}}$$

h : hot leg
c : cold leg
i : inlet
o : outlet

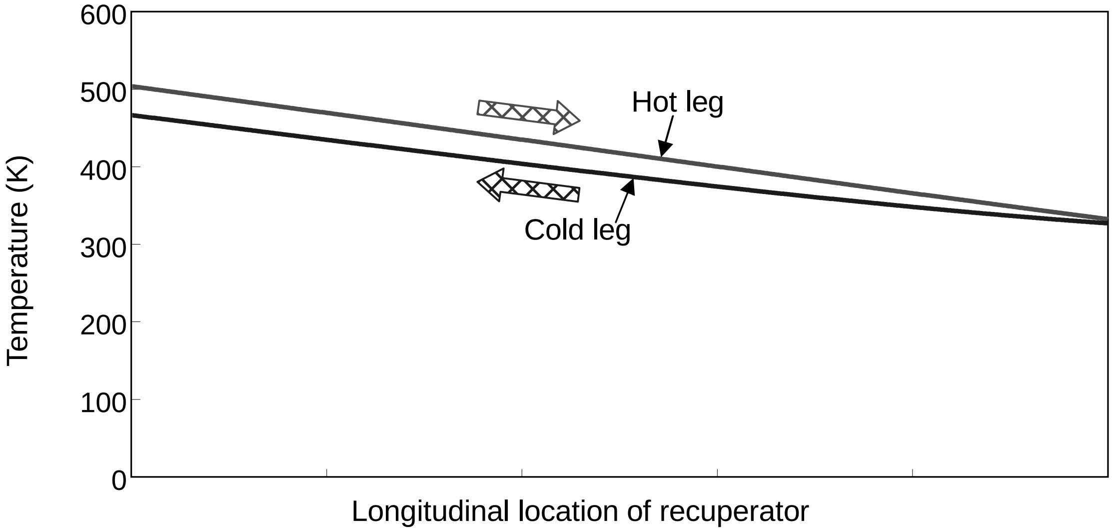

Fig.3.11 CO_2 Temperature longitudinal distribution in recuperator (1D calculation)

(3) Zigzag type PCHE (Recuperator) test results

The pressure drop, the temperature efficiency ratio and the overall coefficient of heat transmission (U) were measured to evaluate the fundamental thermal-hydraulic properties of the PCHE modules (Recuperators).

a) Pressure drop

Figures 3.12 (HX-4) and 3.13 (HX-3) show the pressure drops of the zigzag fin recuperators. The pressure drop coefficients are indicated in Figs. 3.14 (HX-4) and 3.15 (HX-3). The pressure drop coefficient of the cold leg is higher than that of the hot leg in both the recuperators. The pressure drop coefficient is dependent on the angle of the zigzag fin. As the angle of the cold leg fin is smaller than that of the hot leg fin, the pressure drop coefficient of the cold leg is larger than that of the hot leg.

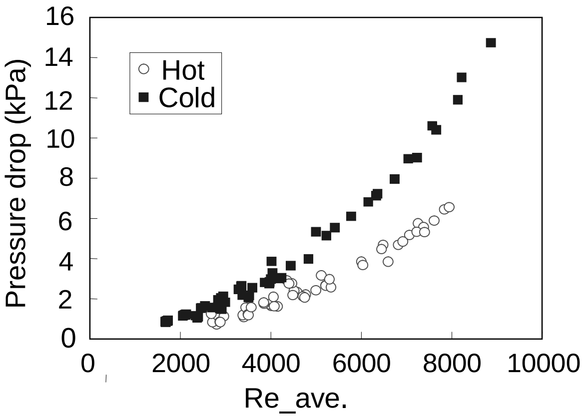

Fig. 3.12 Pressure drop
[Zigzag-fin recuperator (2):HX-4]

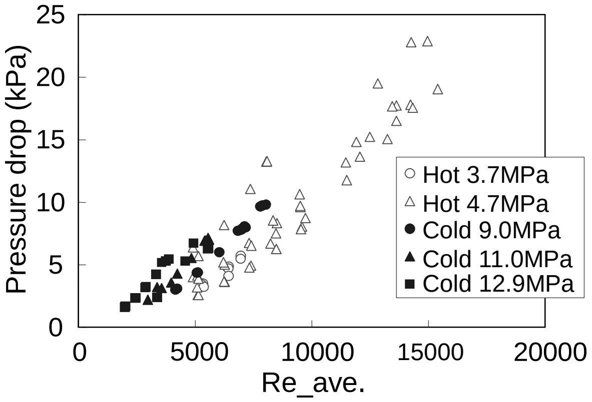

Fig. 3.13 Pressure drop
[Zigzag-fin recuperator (1):HX-3]

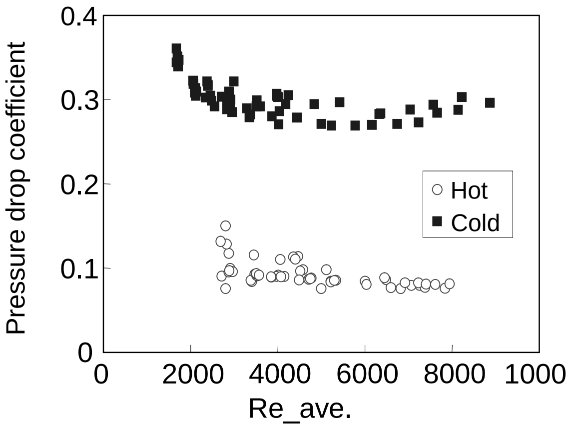

Fig. 3.14 Pressure drop coefficent
[Zigzag-fin recuperator (2):HX-4]

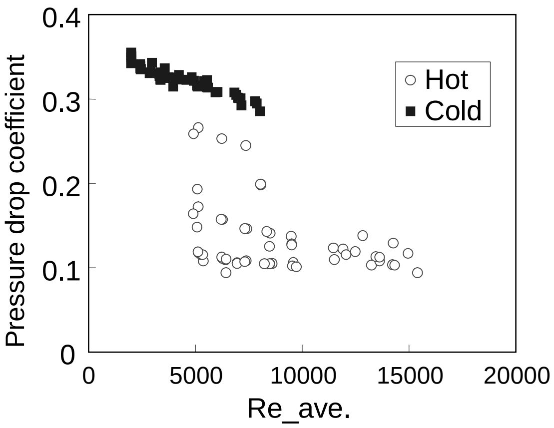

Fig. 3.15 Pressure drop coefficent
[Zigzag-fin recuperator (1):HX-3]

b) Temperature efficiency ratio

Figure 3.16 shows the temperature efficiency ratio of the zigzag fin recuperator (HX-4). The temperature efficiency ratio of the hot leg is 98~99%, and that of the cold leg is 50~75%. Since the pressure of the hot leg is lower than that of the cold leg, the CO_2 density in the hot leg is also lower than that in the cold leg. Therefore, the thermal capacity of the hot leg CO_2 is smaller than that of the cold leg CO_2. This thermal capacity difference brings about the effect that the hot leg outlet temperature is very close to the cold leg inlet temperature, the cold leg outlet temperature being somewhat below the hot leg inlet temperature. This can be explained by the 1D thermal-hydraulic analysis results shown in Fig. 3.11.

c) Overall coefficient of heat transmission

The overall coefficient of heat transmission U is defined as follows:

$$U = \frac{Q}{A \cdot \Delta T}$$

Q : Heat transfer of whole flow path

A : heat transfer area

ΔT : temperature difference between hot leg and cold leg.

Figure 3.17 shows the overall coefficient of heat transmission (U) of the zigzag fin recuperator (HX-4). The overall coefficient of heat transmission became higher as the pressure was increased, because the density and thermal transfer of CO_2 rose higher with high pressure.

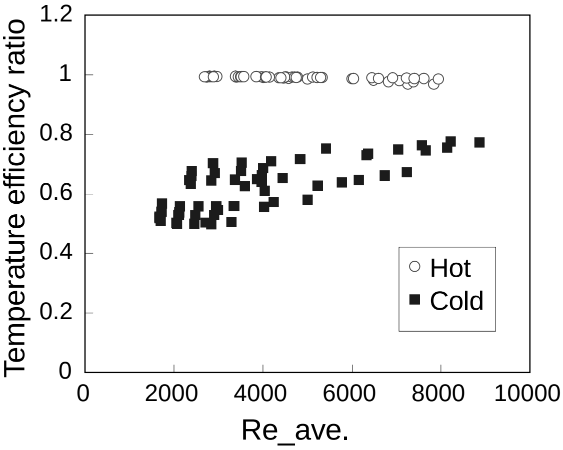

Fig. 3.16 Temperature efficiency ratio [Zigzag-fin recuperator (2): HX-4]

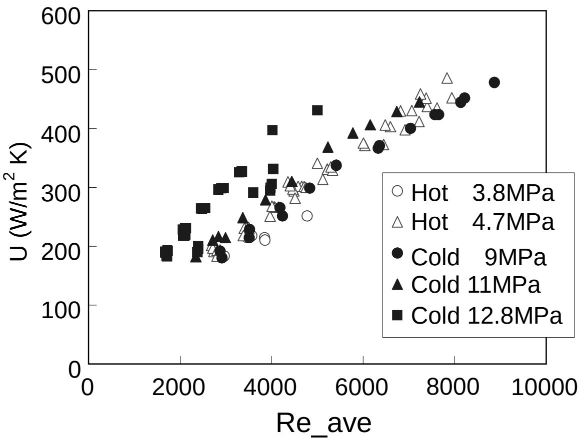

Fig. 3.17 Overall coefficient of heat transmission U [Zigzag-fin recuperator (2): HX-4]

(4) S-fin type PCHE (recuperator) test results

Figures 3.18 and 3.19 show the temperature efficiency ratio and the overall coefficient of heat transmission (U) of the S-fin recuperator (HX-4). The hot leg outlet temperature is close to the cold leg inlet temperature, and its temperature efficiency ratio is close to 1.0. The temperature efficiency ratio of the cold leg is approximately 0.6. The thermal capacity difference due to the different pressures caused this temperature efficiency difference. This is the same tendency as in the zigzag fin type recuperator.

There is no significant difference between the overall coefficient of heat transmission (U) of the zigzag-fin type and that of the S-fin type.

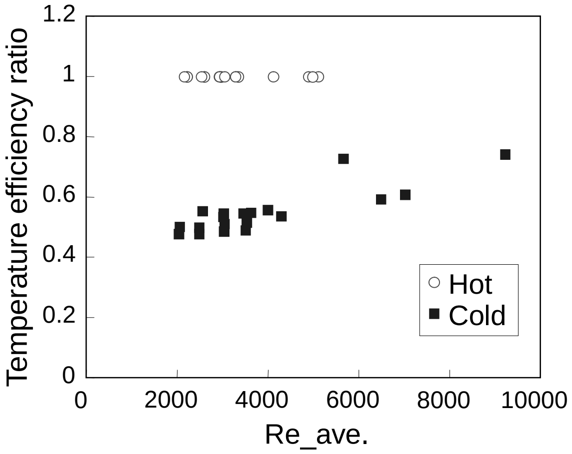

Fig. 3.18 Temperature efficiency ratio
[S-fin recuperator (2): HX-4]

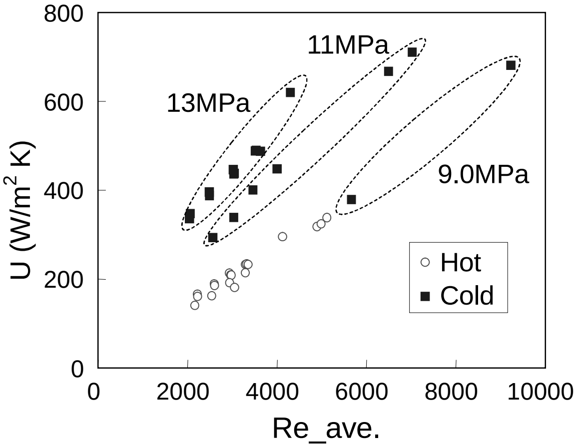

Fig.3.19 Overall coefficient of heat transmission (U)
[S-fin recuperator (2): HX-4]

3.5. Operation stability tests

The SC-CO_2 cycle stability tests were executed under both the transient and steady conditions. A transient test was done by changing from a sub-critical to a super-critical state. After that, the last of the transient conditions was maintained for the steady test.

(1) Transient condition

The test loop was operated taking the CO_2 from the sub-critical to the super-critical state at the compressor. The CO_2 was heated at the rate of 300°C/hr under the following constant conditions.

- Low pressure region of the loop: 4.7MPa
- High pressure region of the loop: 11.0MPa
- High pressure compressor CO_2 flow rate: 260kg/hr
- Bypass compressor CO_2 flow rate: 150kg/hr.

Figure 3.20 shows the inlet and outlet temperatures and the inlet and outlet pressure of the recuperators. No unusual temperature and pressure fluctuation occurred during the transition from the sub-critical to the super-critical region. The oscillation observed in the HX-4 hot leg inlet temperature was considered to be due to the heater control. The state of the inlet and outlet of the high pressure compressor and that of the bypass compressor are indicated in Figs. 3.21 and 3.22, respectively. The CO_2 flow rate was fluctuating. This was due to the reciprocating motion of the compressors. No significant flow instability caused by the transition from sub-critical to super-critical was observed in the flow rates, the pressures or the temperatures.

(2) Steady condition

The stability test during the steady state was executed under the constant conditions below.

- Heater outlet temperature: 300°C
- Low pressure region: 4.7MPa
- High pressure region: 11.0MPa
- High pressure compressor CO_2 flow rate: 260kg/hr
- Bypass compressor CO_2 flow rate: 150kg/hr.

The high pressure regions of the test loop are super-critical in the steady state. The inlet and outlet temperatures and the inlet pressure of the recuperators are shown in Fig. 3.23. A little fluctuation was observed in the HX-4 cold leg outlet temperature. The HX-3 cold leg inlet pressure was also slightly fluctuated. They were considered to be caused by the reciprocating motion of the compressors, not by the super-critical environment, because the temperature and pressure fluctuations were synchronized with the compressor reciprocating cycle.

The state of the inlet and outlet of the high pressure compressor and that of the bypass compressor are indicated in Figs. 3.24 and 3.25, respectively. No significant fluctuation was observed.

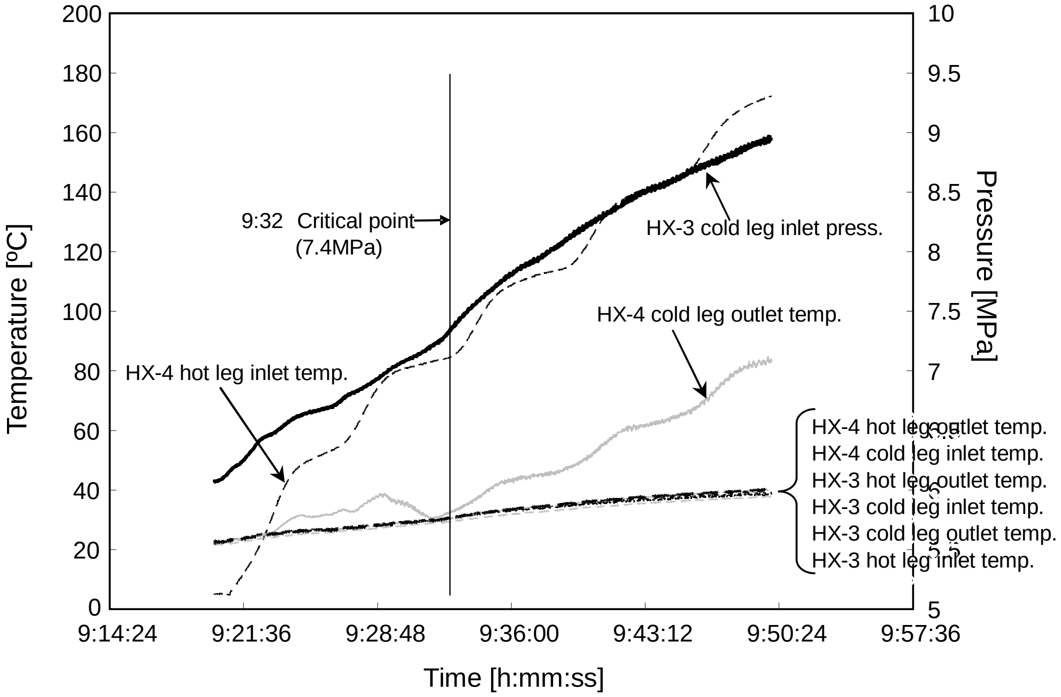

Fig. 3.20 Inlet and outlet state of recuperators (Transient)

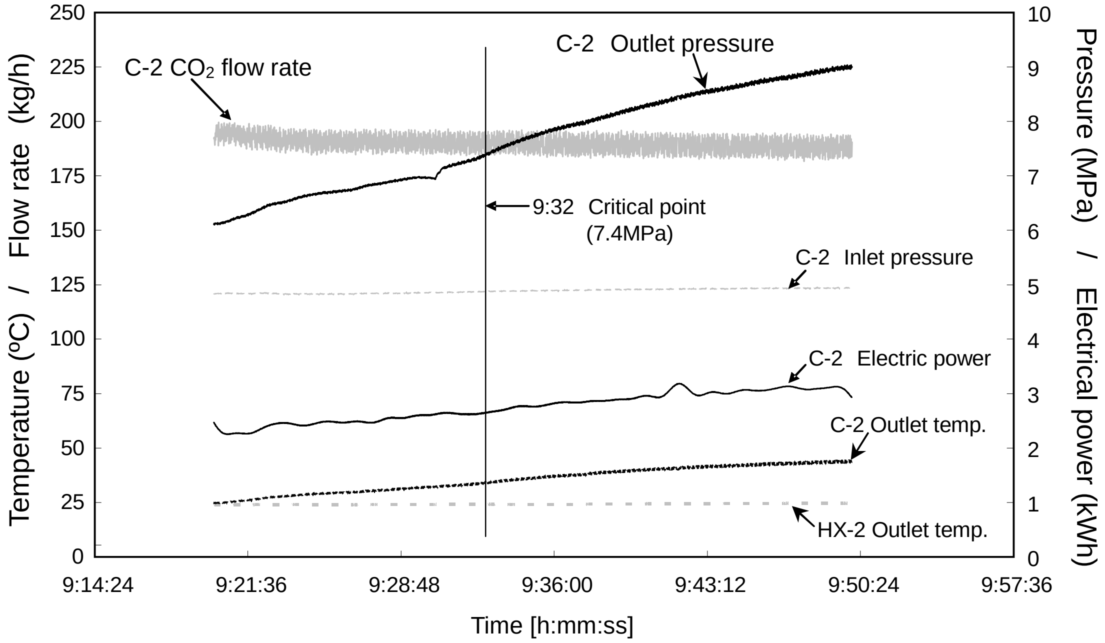

Fig. 3.21 Inlet and outlet state of high pressure compressor (Transient)

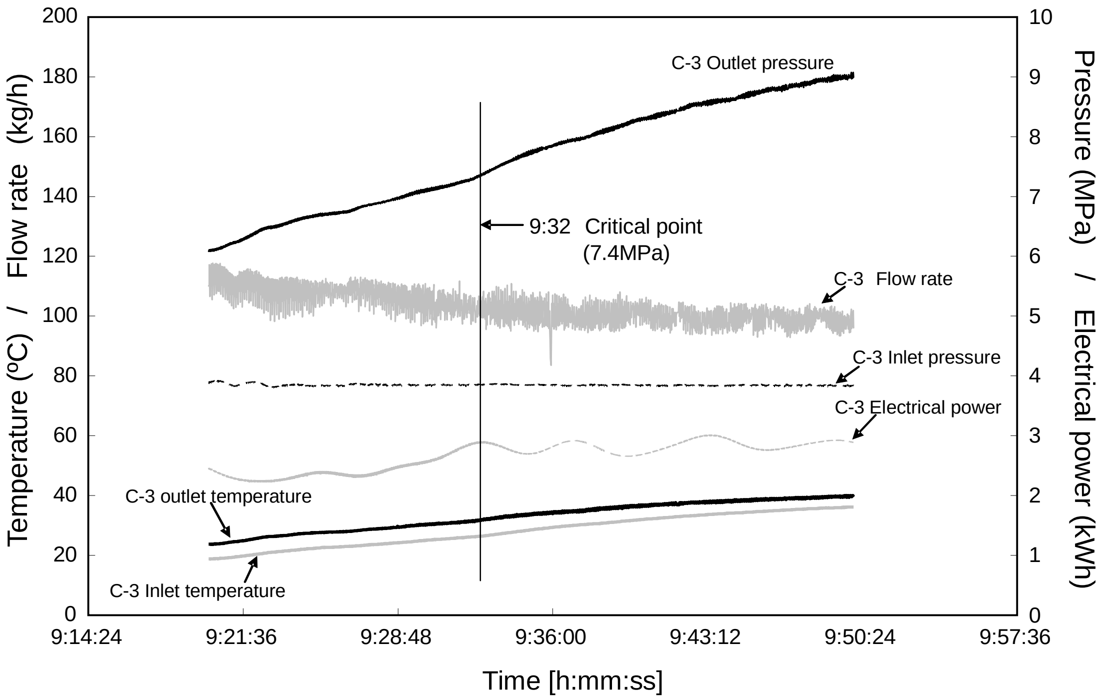

Fig. 3.22 Inlet and outlet state of bypass compressor (Transient)

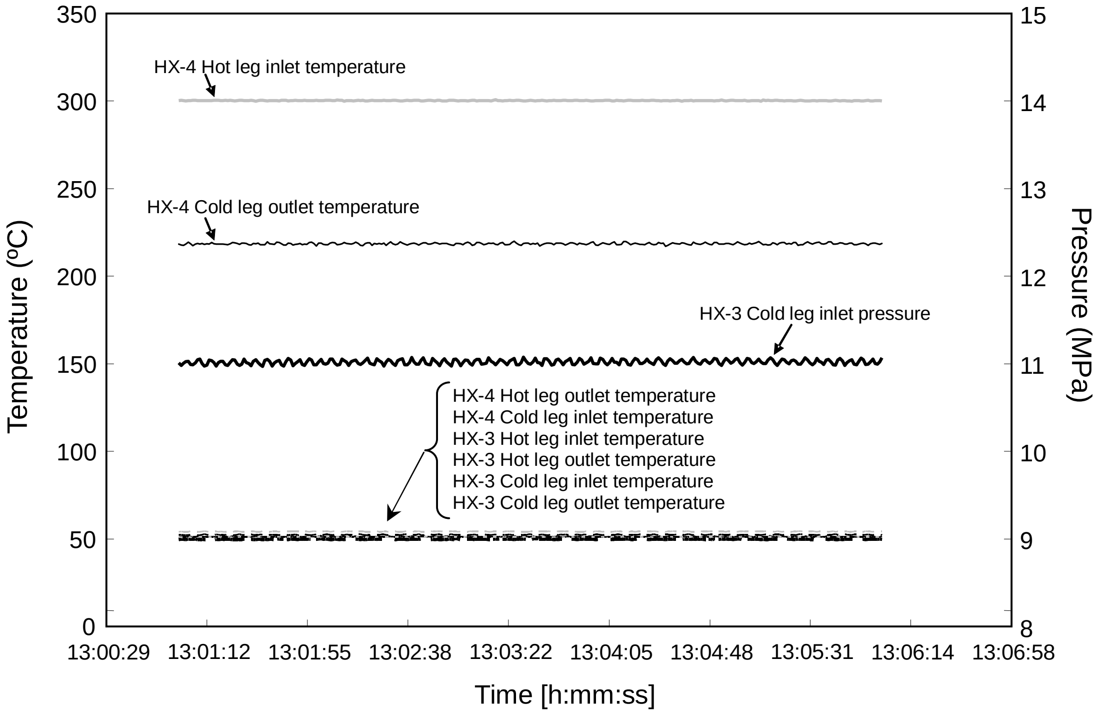

Fig. 3.23 Inlet and outlet state of recuperators (Steady)

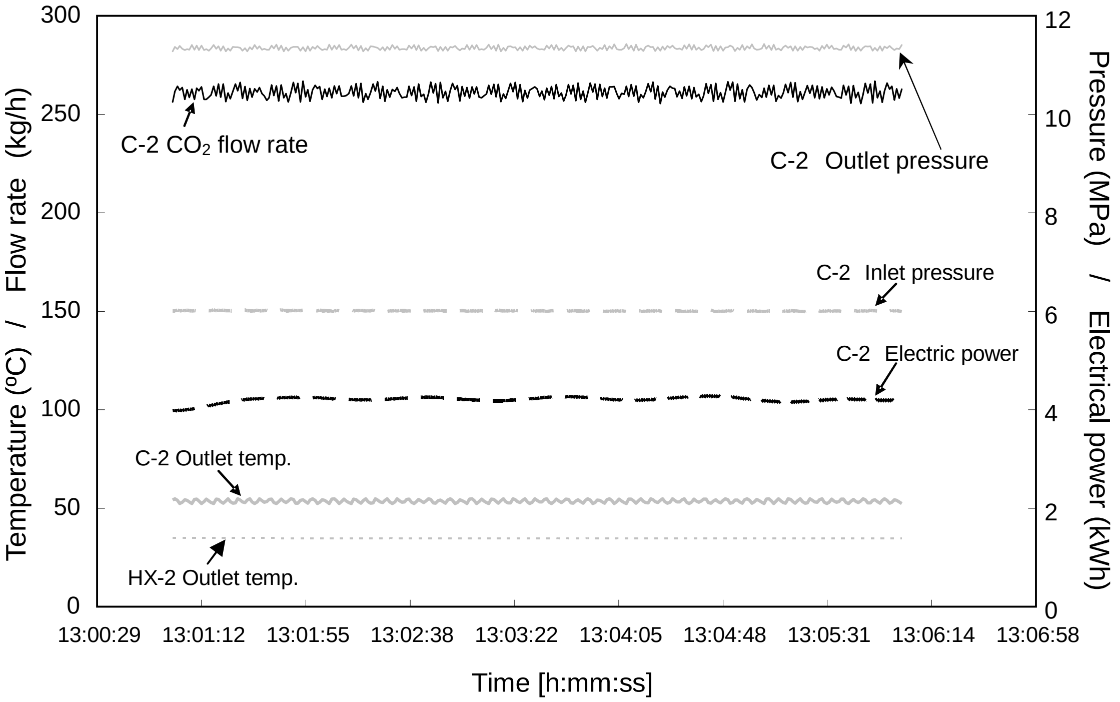

Fig. 3.24 Inlet and outlet state of high pressure compressor (Steady)

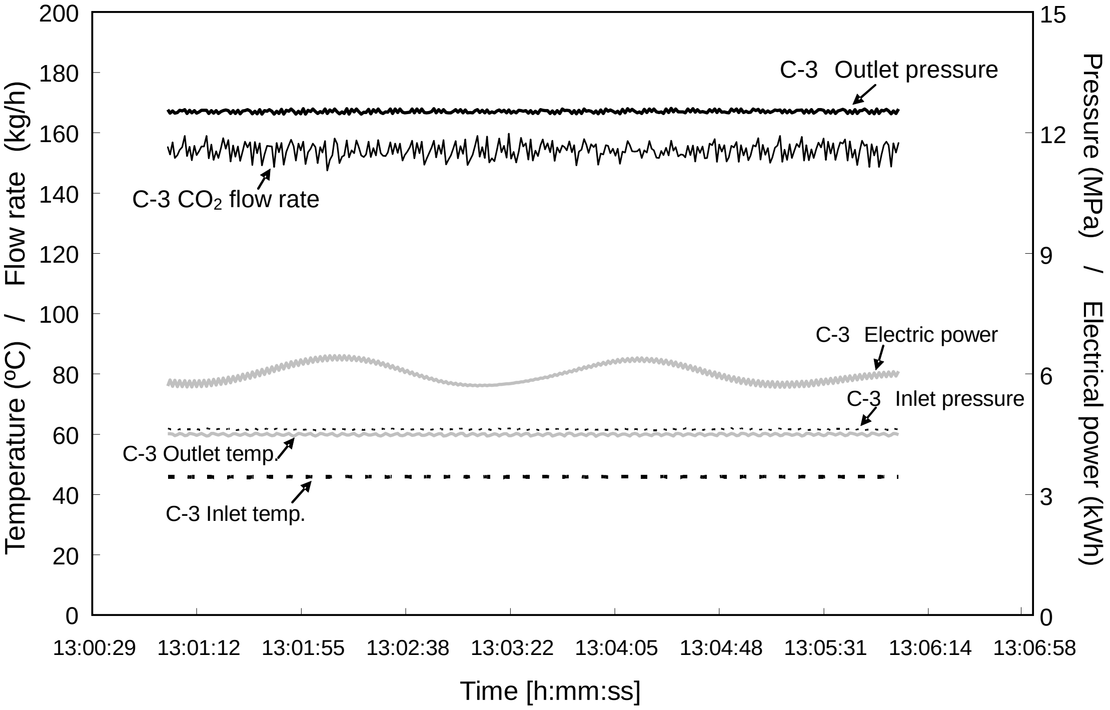

Fig. 3.25 Inlet and outlet state of bypass compressor (Steady)

3.6. Conclusions

The efficiency of the compressor, the thermal-hydraulic performance of the PCHE type recuperators and the flow stability were examined in the SC-CO_2 test loop.

The net power to compress CO_2 was reduced near the critical region, and the high efficiency of the compressor was experimentally confirmed. Two types of recuperator were fabricated, one of the zigzag fin type and the other of the S-fin type. The S-fin type is intended to lower the pressure drop for higher efficiency. The two recuperators exhibited similar heat transfer performance. In the stability tests, no significant fluctuation occurred in either steady or transient conditions. There were small fluctuations which were caused by the reciprocating motion of the compressor, not by the super-critical environment.

This SC-CO_2 cycle test was the preliminary stage for a full-dress investigation. In this test, the CO_2 flow rate was small, and the compressors and the turbine were not operated coaxially. To evaluate the SC-CO_2 cycle system performance in detail, another test which simulates an actual SC-CO_2 cycle system more precisely is necessary in the future.

4. Liquid sodium / CO_2 reaction test

4.1 Introduction

Sodium / CO_2 reaction tests were executed to elucidate fundamental phenomena as a preliminary stage. The purposes of the experiment were the observation of contact of liquid sodium with CO_2 gas, the analysis of reaction products and the measurement of a reaction heat.

4.2 Reaction tests

(1) Observation of liquid sodium / CO_2 gas contact tests

The test apparatuses for sodium / CO_2 gas contact tests are shown in Figs. 4.1 and 4.2. The test apparatus [A] shown in Fig. 4.1 was fabricated first. A small-sized holder filled with sodium and its stand was placed in a reaction test vessel. The stand was heated by an electric heater to set sodium temperature conditions. The CO_2 gas entered the bottom of the test vessel, and it flowed upward around the sodium holder. The temperatures of the sodium and the CO_2 gas were measured by several thermo-couples. The CO_2 gas temperature near the sodium surface could not be raised enough, and the highest temperature being approximately 70~150ºC. To increase the CO_2 gas temperature, a CO_2 gas blowing nozzle with a heater was installed above the sodium holder as shown in Fig. 4.2 (Test apparatus [B]). The CO_2 gas flow temperature then could be made around 600ºC.

The test conditions and results are shown in Table 4.1. Details of the test results of the apparatus [A] are shown in Fig. 4.3 (case 8) and Fig. 4.4 (case 12). The test cases 8 and 12 were selected to determine the effect of the CO_2 gas temperature. The sodium temperature in both the cases was 600ºC. The CO_2 gas temperature in the test cases 8 and 12 were 130ºC and 240ºC, respectively. No severe reaction occurred in the test case 8. In the test case 12, aerosol was produced and the temperature rapidly increased. The CO_2 gas temperature difference brought about these distinctive phenomena, the appearance of aerosol and the temperature rise.

The test results of the apparatus [B] are shown in Fig. 4.5 (case 15), Fig. 4.6 (case 16) and Fig. 4.7 (case 17). The temperatures of CO_2 gas blown over sodium in the test cases 15, 16 and 17 were 600 ºC, 580 ºC and 570 ºC, respectively. The sodium temperature is the same as the CO_2 gas blown over temperature in each test case.

In the test case 15 (600 ºC), aerosol was produced from the beginning. The sodium temperature began to increase and burned with flame in approximately 20 seconds.

The temperature was lowered by 20ºC in the test case 16 (580 ºC). Aerosol was similarly produced from the beginning, and after that the reaction seemed to stop for a while. The sodium, however, burned with flame in 185 seconds, and the temperatures also rose.

The temperature was further decreased by 10ºC in the test case 17 (570 ºC). Although aerosol appeared, no sodium burning was observed during the test period.

(2) Reaction products analysis

Analyzers and detectors for solid and gaseous reaction products are shown in Table 4.2. The analysis results of solid reaction products are shown in Tables 4.3 and 4.4. Table 4.3 gives the quantitative analysis results, and Table 4.4 gives qualitative analysis results.

The solid reaction products referred to in Table 4.2 were obtained from samples of the test cases 15 and 16. The main product was Na_2CO_3. A small amount of Na_2O_2 and amorphous carbon were detected, too. Potassium permanganate titration analysis was applied to analyze Na_2O_2. Since this analysis method also responds to FeO, the FeO of the sodium holder might have been detected instead of Na_2O_2.

SEM (Scanning Electron Microscope) / EDX (Energy Dispersive X-ray spectroscopy) and XRD (X-ray diffraction analysis) were applied to identify the "Others" in Table 4.3. The reaction product of the case 17 was analyzed. A black colored thin film was formed on the sodium surface in this test case (Fig. 4.8).

The EDX revealed that C, O and Na existed in the black film in their element forms. As shown in Table 4.4, metal-Na, NaOH, Na_2CO_3 and Na_2CO_3-H_2O were detected by the XRD. Moisture (H_2O) is necessary for the formation of NaOH and Na_2CO_3-H_2O. No moisture, however, was intentionally added in the reaction test. Moisture of the atmosphere might have produced NaOH and Na_2O_3-H_2O in the analysis process. Only a small amount of the main product, Na_2CO_3, was measured by the XRD as shown in Table 4.4. This is because the crystallization of Na_2CO_3 was low and its signal detected by the XRD is considered to be weak.

Gas chromatography revealed that the main gaseous reaction product was carbon monoxide (CO). Figure 4.9 shows the CO concentration changes in the test cases 12, 15 and 16. The test case 15 was executed at the highest temperature, and its CO concentration rapidly increased.

(3) Reaction heat measurement

The sodium/CO_2 gas reaction heat was measured by a Calvet Differential Scanning Calorimetry (DSC) method. The calorimetry system consists of a reaction vessel for the DSC, a SC-CO_2 supply system and a pressure regulator, which is shown in Fig. 4.10.

Sodium was set in the reaction vessel and the vessel was filled with Ar gas at room temperature at first. Secondary, the vessel was heated up and the Ar gas was gradually replaced to CO_2 gas under the 0.2MPa pressure condition. And then the calorific value transits were measured (DSC curve). The reaction heat was estimated to be approximately 50~75kJ/Na-mol.

4.3 Conclusions

The sodium / CO_2 reaction test was carried out to identify the fundamental phenomena. The analysis indicated that the main reaction product was Na_2CO_3. CO gas and a little amorphous carbon gas were also detected.

In the sodium/CO_2 gas contact test, CO_2 gas and sodium continuously reacted with flame at temperatures higher than 570~580°C. No continuous reaction and no flame occurred at the temperature less than 570~580°C. The temperature threshold of the reaction seemed to be between 570~580°C. The existence of this temperature threshold cannot be explained by a theoretical chemical reaction. The thin film formed on the sodium surface might restrict this reaction.

The CO_2 gas was blown over stationary sodium in this test. However, actually sodium flows at a certain flow rate in a tube bundle. Direct injections of CO_2 gas to flowing sodium might result in different phenomena. Further experiments that simulate sodium and CO_2 behavior in a heat exchanger are necessary to reveal this in detail.

Table 4.1 Sodium / CO_2 reaction test results

Test case No.	Test apparatus	Na initial temp. (ºC)	Na amount (g)	ID of Na holder (mm)	Supply CO_2 temp. (ºC)	Humidity in CO_2 (vppm)	Results	
							Aerosol (Reaction in surface)	Frame and continuous reaction)
1	A	200	1.2	16	Main flow: 70	< 5	no	no
2	A	300	1.2	16	Main flow: 90	< 5	yes	no
3	A	400	1.2	16	Main flow: 100	< 5	yes	no
4	A	550	1.2	16	Main flow: 110	< 5	yes	no
5	A	550	1.2	16	Main flow: 130	< 5	yes	no
6	A	550	1.2	16	Main flow: 130	2500	yes	no
7	A	550	1.2	16	Main flow: 130	6000	yes	no
8	A	600	1.2	16	Main flow: 130	< 5	yes	no
9	A	615	1.2	16	Main flow: 150	< 5	yes	yes
10	A	630	1.2	16	Main flow: 150	< 5	yes	yes
11	A	650	1.2	16	Main flow: 150	< 5	yes	yes
12	A	600	1.2	16	Main flow: 240	< 5	yes	yes
13	A	500	1.2	16	Main flow: 230	< 5	yes	no
14	B	600	1.2	16	Main: 240 + Blow over: 600	< 5	yes	yes
15	B	600	4.8	32	Main: 260 + Blow over: 600	< 5	yes	yes
16	B	580	4.8	32	Main: 240 + Blow over: 580	< 5	yes	yes
17	B	570	4.8	32	Main: 240 + Blow over: 570	< 5	yes	no

Table 4.2 Analyzer and detector for reaction products

Solid reaction products qualitative analysis	X-ray diffraction analysis (XRD)	
	Scanning Electron Microscope (SEM)	
	Energy Dispersive X-ray spectroscopy (EDX)	
Solid reaction products quantitative analysis	Mercury amalgamation analysis [Na]	
	Potassium permanganate titration analysis [Na_2O_2]	
	Total Organic Carbon analysis (TOC) [Na_2CO_3 , Amorphous Carbon]	
Gaseous reaction products quantitative analysis	Gas Chromato-graphy	Photo Ionization Detector (PID) [H_2, CO] Flame Ionization Detector (FID) [Hydro-carbon] Thermal conductivity detector (TCD) [CO_2 ,O_2]

Table 4.3 Solid reaction products quantitative analysis result (case15, case16)

Case No.	Na (wt-%)	Na_2CO_3 (wt-%)	Na_2O_2 (wt-%)	C (wt-%)	Others (wt-%)
case 15	18.3	72.0	0.5	0.4	8.8
case 16	13.0	67.8	0.4	0.7	18.1

Table 4.4 X-ray diffraction (XRD) qualitative analysis result (case17)

XRD analysis			
Metal Na	NaOH	Na_2CO_3	Na_2CO_3-H_2O
++++	A little	A little	A little

Table 4.5 Total Organic Carbon (TOC) quantitative analysis result (case17)

Na_2CO_3 (wt-%)	Amorphous Carbon (wt-%)
63	0.1

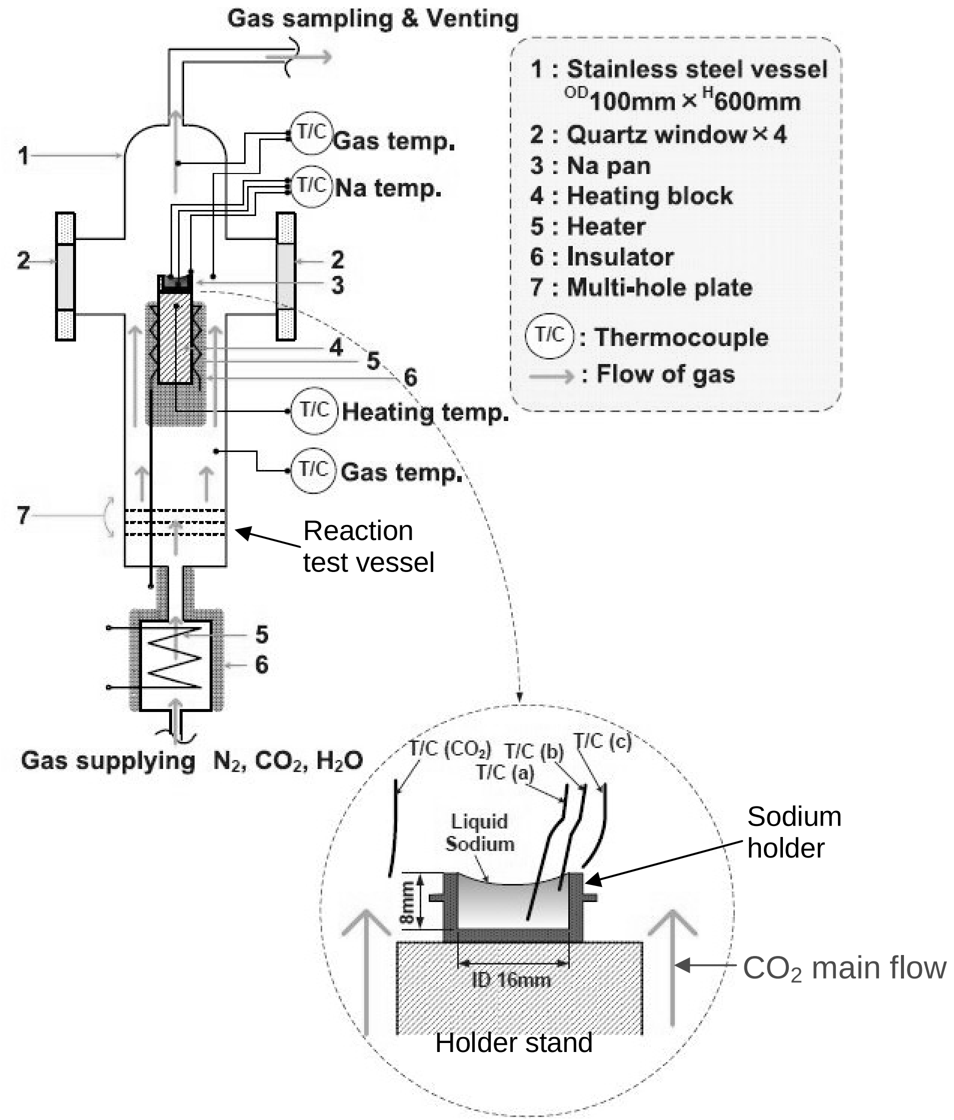

Fig. 4.1 Sodium / CO_2 reaction test apparatus [A]
(Test case 1~13)

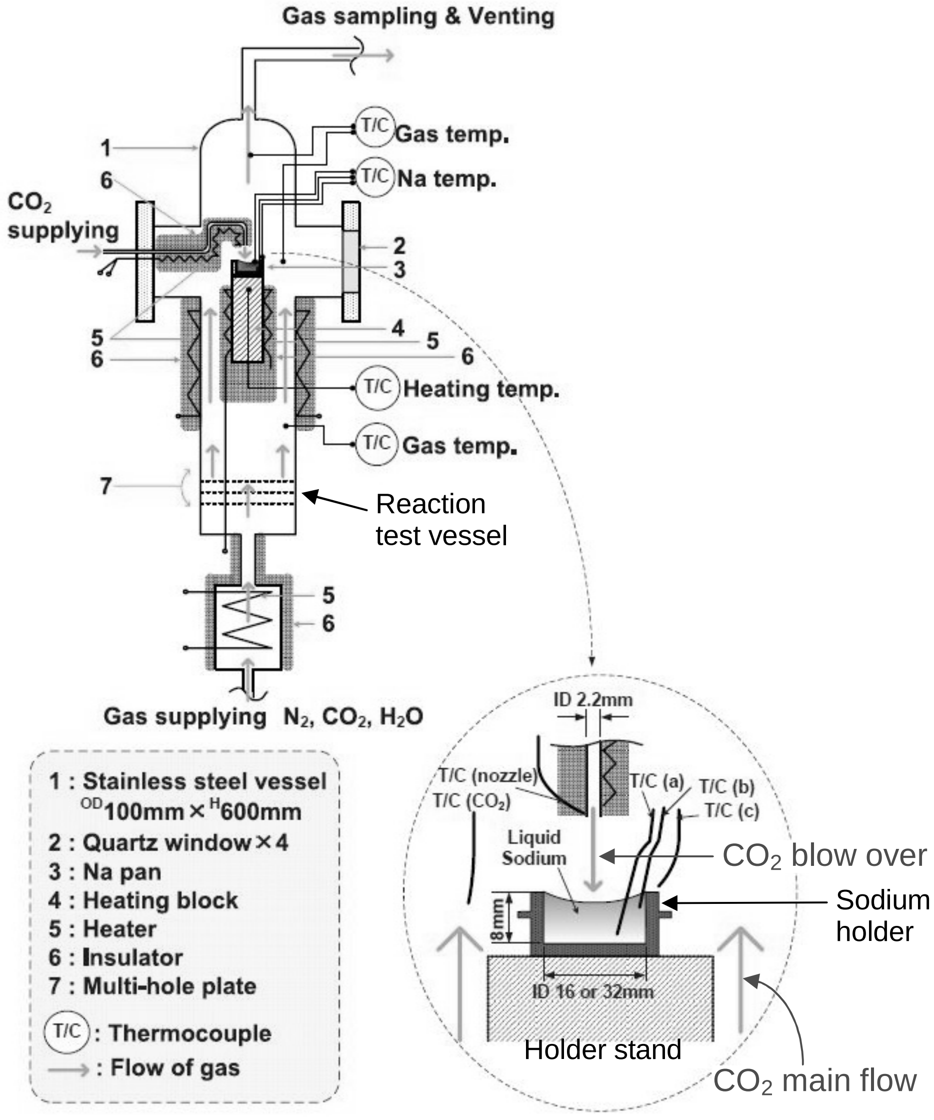

Fig. 4.2 Sodium / CO_2 reaction test apparatus [B]
(Test case 14~17)

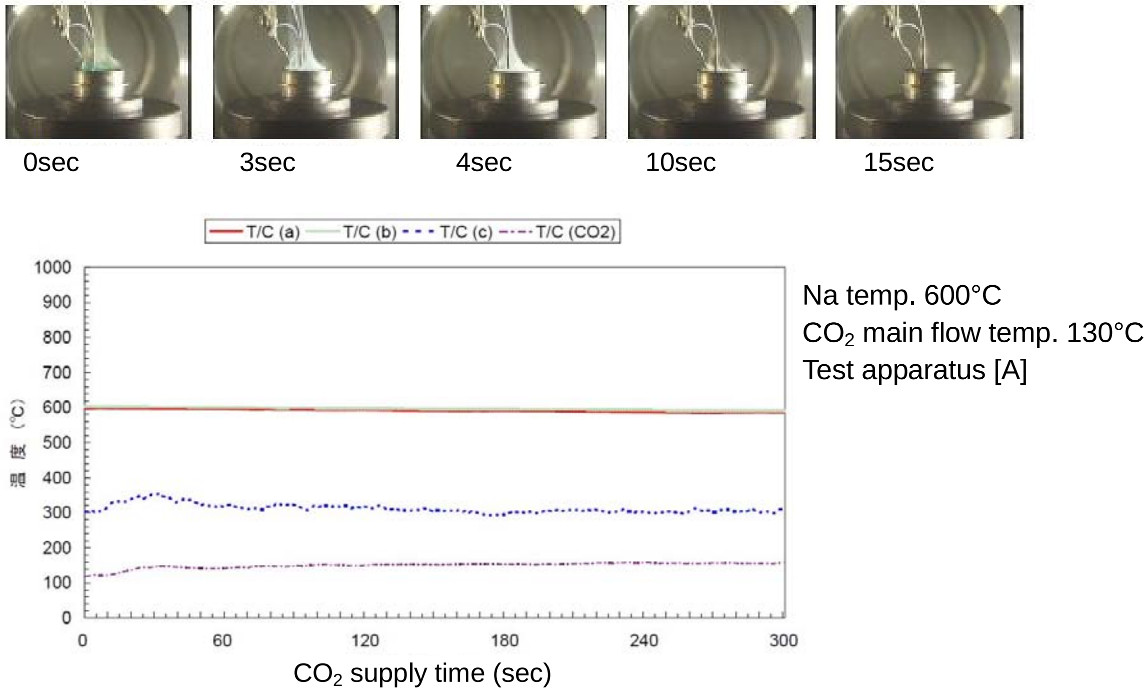

Na temp. 600°C
CO$_2$ main flow temp. 130°C
Test apparatus [A]

Fig. 4.3 Sodium / CO$_2$ reaction test (case8)

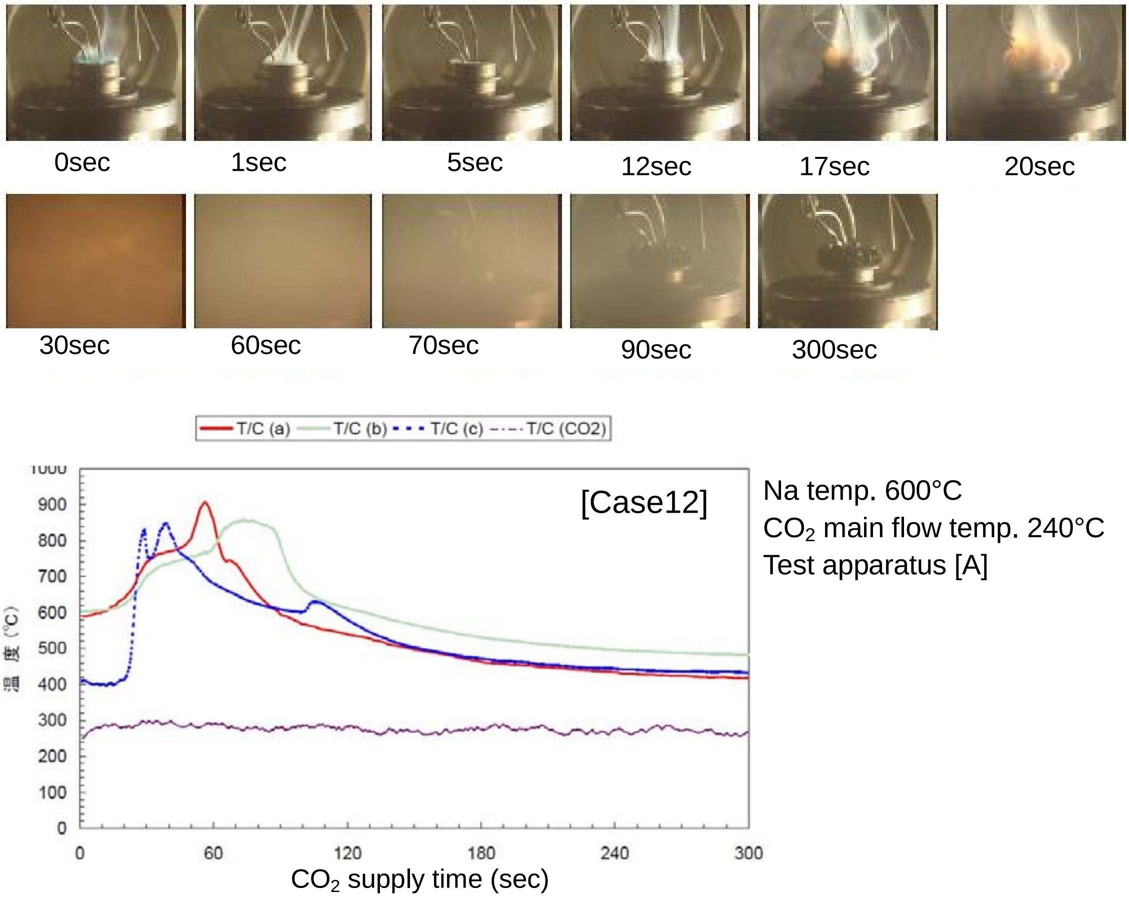

Na temp. 600°C
CO$_2$ main flow temp. 240°C
Test apparatus [A]

Fig. 4.4 Sodium / CO$_2$ reaction test (case12)

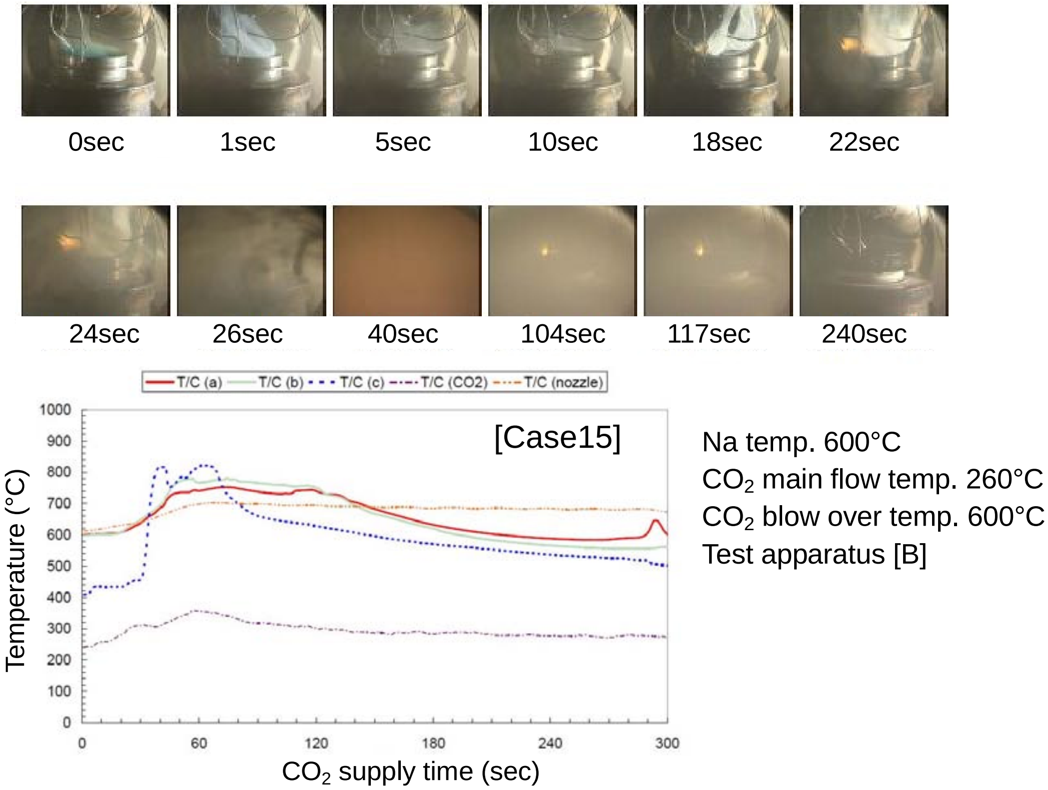

Na temp. 600°C
CO_2 main flow temp. 260°C
CO_2 blow over temp. 600°C
Test apparatus [B]

Fig. 4.5 Sodium / CO_2 reaction test (case15)

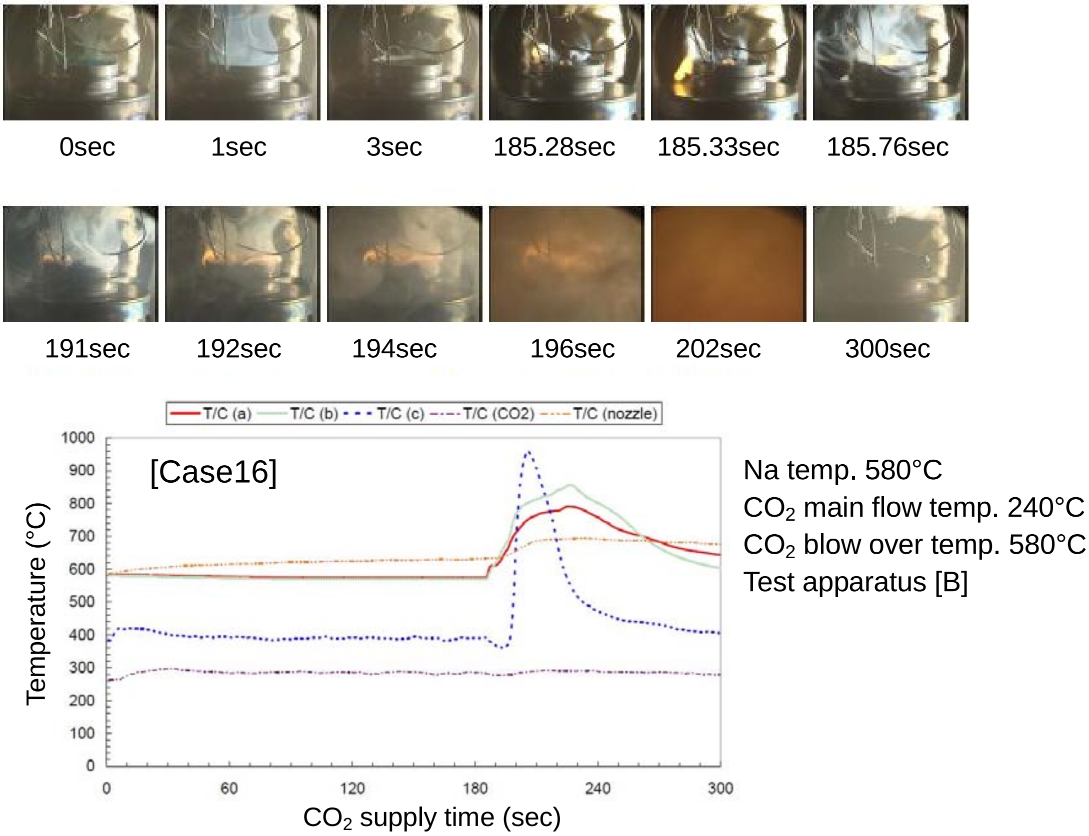

Na temp. 580°C
CO_2 main flow temp. 240°C
CO_2 blow over temp. 580°C
Test apparatus [B]

Fig. 4.6 Sodium / CO_2 reaction test (case16)

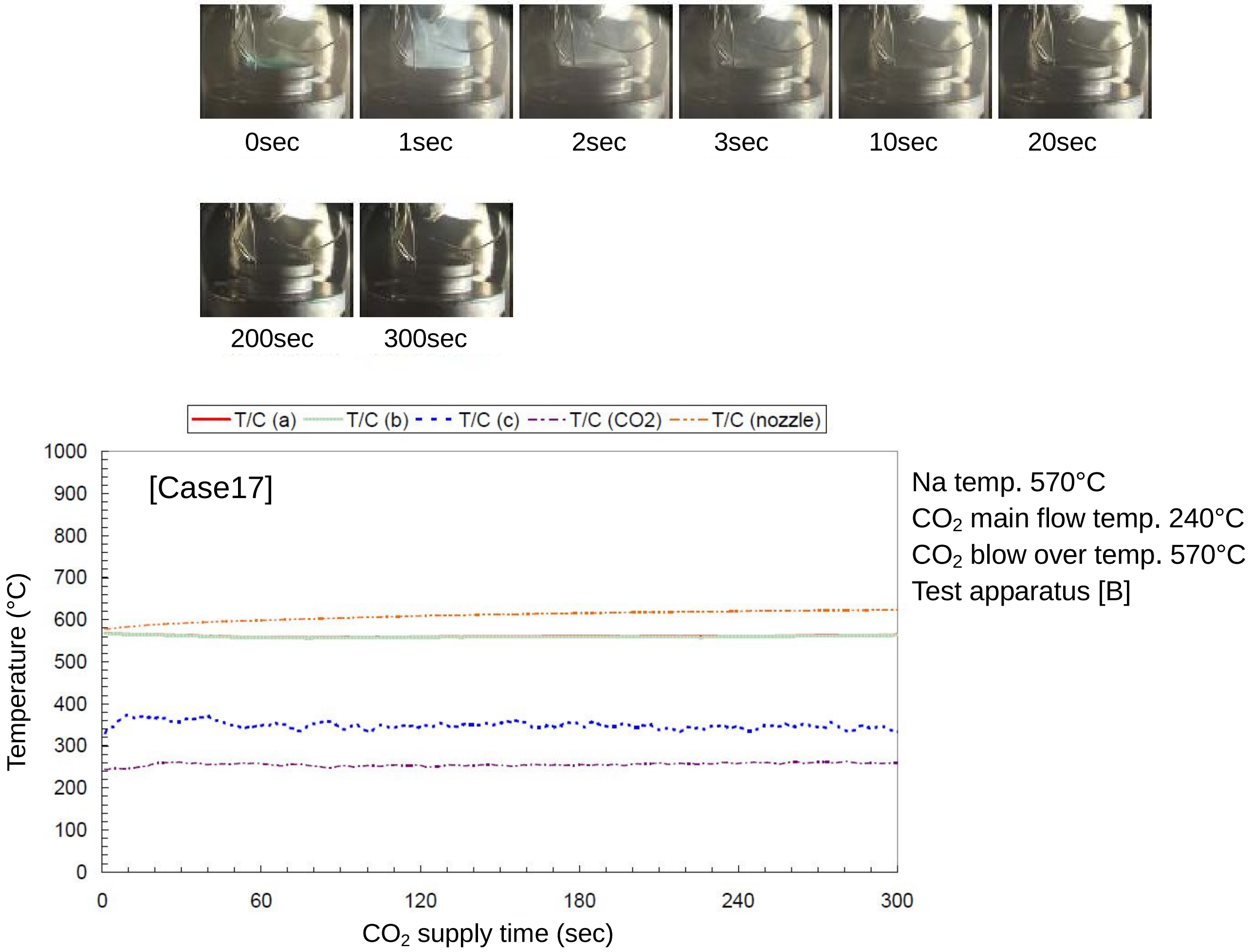

Fig. 4.7 Sodium / CO_2 reaction test (case17)

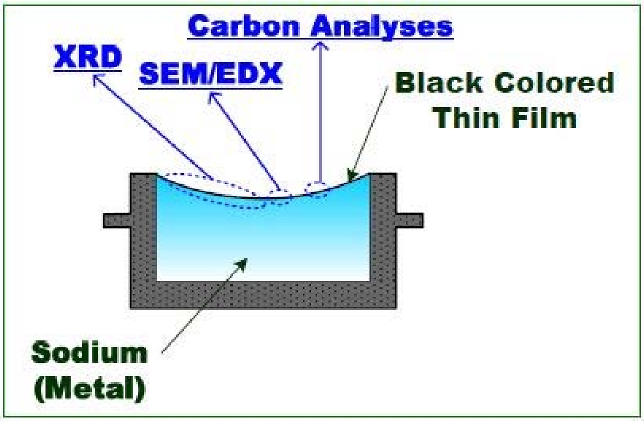

Fig. 4.8 Solid reaction products analysis of test case 17

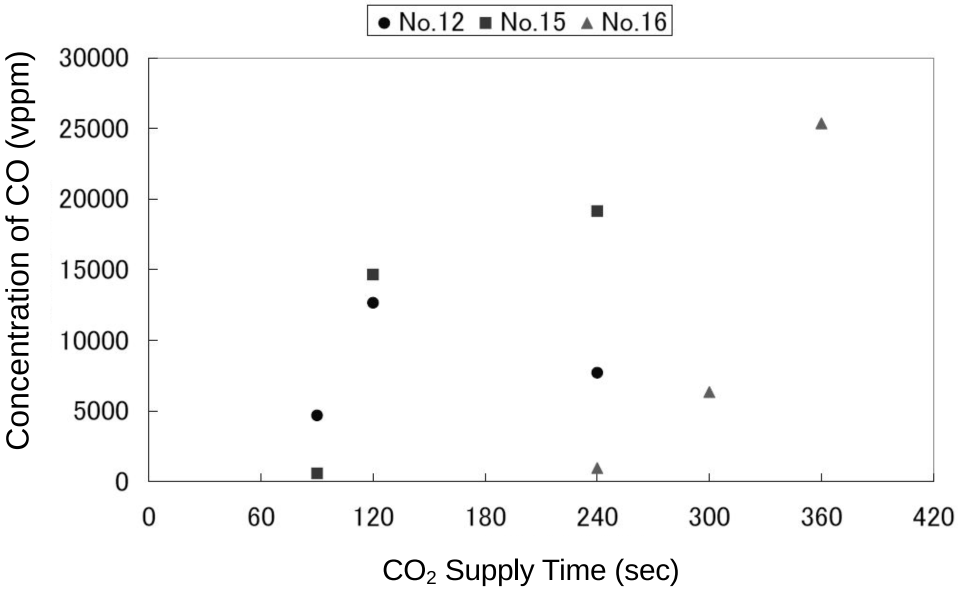

Fig. 4.9 CO gas concentration transient in Na/CO_2 reaction tests

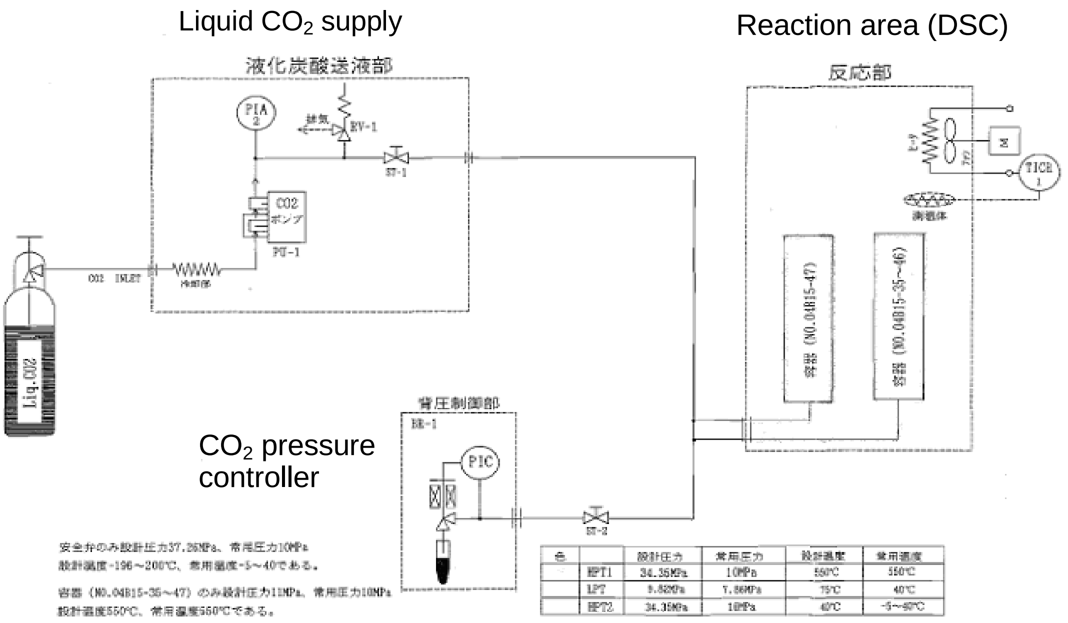

Fig. 4.10 Na/CO_2 reaction heat measurement system

5. Tube failure computer code analysis

5.1 Introduction

Sodium/CO_2 heat exchangers are connected to primary sodium circuits. A heat transfer tube failure thus affects the reactor core or the primary circuit. Safety evaluation is necessary to examine the prospects of an SFR adopting a SC-CO_2 system. The existing sodium/water reaction computer code has been applied for the safety evaluation in case of a CO_2 gas leak. The analysis models of the code were changed from sodium/water reaction models to sodium/CO_2 reaction models. Some of the sodium/CO_2 reaction analysis models were based on assumptions. The computer code predicted the behavior of reaction products, the changes in the pressure, and the temperature in the primary sodium circuit. Based on these results, safety was discussed.

5.2. Analytical model and conditions

(1) Key points and procedure of evaluation

The reactor core safety and the plant safety were evaluated with regard to the following key points.

a. Void reactivity in the reactor core by gaseous substances
b. Sodium flow blockage by solid reaction products in fuel assemblies
c. Temperature and pressure rising in the primary sodium circuit.

The procedure of the safety evaluation is indicated in Fig. 5.1. First, the analysis models for calculating the sodium/CO_2 reaction and the thermal-hydraulic properties were chosen and adjusted. Secondly, the sodium/CO_2 reaction mitigation system was designed and its operational sequence was determined. Finally, sodium/CO_2 reaction analysis for a DEG (Double Ended Guillotine) tube failure was done.

(2) Network model of analysis area

The network model for the computer analysis is shown in Fig. 5.2. The whole primary sodium circuit and the reaction products release system were modeled into paths and nodes. The paths are flow calculation areas, and nodes are pressure and temperature calculation areas. The network model consists of a CO_2 leak sodium loop, the reactor vessel and a non-CO_2 gas leak sodium loop. In the CO_2 leak sodium loop, the sodium/CO_2 heat exchanger (HX) was modeled in detail to calculate CO_2 gas leak behavior.

The leaking HX is divided to three areas for the calculation: the upper plenum, the tube bundle, and the lower plenum. The upper plenum includes the cover gas (C/G) region, the sodium surface (C/G and Na) region and the sodium region near the tube bundle. The tube bundle can be divided into the CO_2 leak channel and the non-leak channel, because the tube bundle area is separated into several sectors by tube support plates. The bundle region is also divided to three longitudinal regions. The CO_2 leak area was set to be in the lowest tube bundle part. The cylindrical barrage is installed at the bottom of the tube bundle (inner shroud) to restrain gaseous substance flow. Therefore, there are two analysis regions here, the inside and the outside of the barrage.

The reactor vessel has six regions from the C/G to the lower plenum. The non-CO_2 leak loop is incorporated into the network model to take into consideration the transition of the reaction products in the whole primary sodium circuit.

(3) Analysis conditions

a) Tube failure condition: one DEG (Double Ended Guillotine) tube failure

b) Initial CO_2 gas leak rate: 18.1kg/sec (1DEG)

The CO_2 gas leak rate was calculated by the critical flow formula

$$q_m = \alpha \rho_0 \sqrt{\gamma \frac{R}{M} T_0} \left(\frac{2}{\gamma + 1} \right)^{\frac{(\gamma+1)}{2(\gamma-1)}} A$$

q_m:CO_2 gas leak rate (kg/s) = 18.1
α: Flow coefficient (-) = 0.83
γ: Heat capacity ratio (-) = 1.3
ρ_0: Density (kg/m^3) = 175.1 (22MPa, 661K)
R: Gas constant (J/(kg·K)) = 188.92
M: Molecular weight (kg/mol)= 44.009×10^{-3}
T_0:Temperature (K) = 661
A: Cross section area (m^2) = $2.602\times10^{-3}\times2$

The CO_2 gas leak rate is lowered and finally is terminated in 60 seconds by the CO_2 gas isolation valves and the CO_2 gas blow system.

c) Chemical reaction formula:

The sodium/CO_2 reaction products and reaction heat were calculated based on the chemical reaction formula below.

$$Na + CO_2 \quad = \quad 0.5Na_2CO_3 \quad + \quad 0.5CO\uparrow \quad + \quad 1014\ (kJ/mol)$$

The behavior of the leaked CO_2 gas and the reaction products in the primary sodium circuit were predicted by taking account of the sodium circulation, the release of CO_2 to cover gas regions and the admixture of the non-leak sodium circuit. The release to the reaction products storage tank was also considered. The solid reaction product Na_2CO_3 was assumed to be conveyed by the sodium circulation, but its dissolution and deposition in sodium were not calculated in the code. These phenomena need to be investigated in future research.

d) Sodium primary mechanical pump:

The primary sodium pump of the leaking loop is coasted down by a pump trip signal and then is stopped. The pump of the non-leak loop is operated by its pony motor to maintain a certain sodium flow rate. The pump coast down curve is shown in Fig. 5.3.

5.3 Analytical results

(1) Temperatures and pressures behaviors in primary sodium circuits

The transitions of the sodium flow rates, the pressures and temperatures are shown in Fig. 5.4, 5.5 and 5.6, respectively. The computer analysis predicted the following event sequence after the 1 DEG tube failure.

[0.0 sec]	One DEG tube failure (CO_2 gas leak occurrence)
[7.7 sec]	Leak detection by R/D(1) of HX release signal
[8.7 sec]	Reactor trip
[9.7 sec]	Primary sodium pump trip
[14.4 sec]	R/D(2) of drain tank release
[15.0 sec]	Anti-reverse valve of leaking loop close
[17.7 sec]	CO_2 gas isolation valve closed, CO_2 gas blow valve open
[77.7 sec]	CO_2 gas leak termination.

a) Pressure transition (Fig. 5.5)

The cover gas (C/G) pressure of the leaking HX increased to 0.26MPa at 7.7 seconds and then the R/D(1) of the HX released. The tube failure was detected by the R/D release signal. The reactor and the primary pump were tripped at 8.7 seconds and 9.7 seconds, respectively. Nine seconds after the reactor trip, the SC-CO_2 cycle system was separated from the HX by the isolation valves, and depressurized by the CO_2 gas blow system.

The reaction products in the leaking HX flowed out to the drain tank through the released R/D(1), and therefore the increasing rate of the C/G pressure became small.

The drain tank pressure increased to 0.21MPa at 14.4 seconds and its R/D(2) also opened. After that, the C/G pressure began to decrease. Since the gaseous reaction substance (CO gas) continued to be produced after the R/D release, the C/G pressure gradually rose after 33 seconds. The CO_2 gas leak was stopped at 77.7 seconds, and the C/G pressure was kept below 0.18MPa. The pressure transition of the reactor vessel was almost similar to that of the HX, except the initial term. The maximum reactor pressure was 0.28MPa at 14.4 seconds. All the pressures in the primary circuit were below the allowed level. The pressure rises had no influence on the structural integrity.

b) Sodium flow rate transition (Fig. 5.4)

The reactor inlet sodium flow rate was increased by 3% at the beginning by a pressure rise due to the CO_2 gas leak, and then the sodium flow rate was decreased by the primary pump trip at 9.7 seconds. The reactor sodium flow rate was maintained at 270 kg/sec by the pony motor pump operation of the non-leak loop after 50 seconds.

The hot leg (H/L) sodium flowed backward due to the initial pressure rise in the leaking HX during the period from 2.7 to 9.4 seconds. After that, it returned to a forward flow because of a depressurization of the leaking HX due to the R/D(1) release.

The cold leg (C/L) sodium flow rate of the leaking loop was increased by 30% at the beginning due to the initial pressure rise. It was, however, decreased to zero when the anti-reverse flow valve closed at 15 seconds. Since the sodium head in the leaking HX was decreased due to the gas generation, the sodium flow of the non-leak loop forced backward the C/L sodium flow of the leaking loop.

c) Temperature transition (Fig. 5.6)

The tube bundle temperature arose by the reaction heat. Especially, the reaction channel temperature was rapidly increased to 1000ºC in 2 seconds. The other region (the reactor and sodium pipe), however, showed no extreme temperature rising.

d) Reaction products behavior (Fig. 5.7)

A reaction product was conveyed by a sodium circulation from the leaking HX to the reactor. The amount of the reaction product in the reactor is shown in Fig. 5.7. The amount in the lower plenum reached to its maximum (0.46kg) when the anti-reverse valve closed at 15 seconds. After that, the amount gradually decreased. The anti-reverse valve prevented any further inflow of the reaction products to the reactor vessel, and the sodium circulation of the non-leak loop carried the reaction product up to the reactor core. The reaction product in the core began to increase at 7 seconds. The maximum amount in the core was 117g at 30 seconds. The reaction product in the upper plenum rapidly increased until 10 seconds. This is because the reaction product entered the reactor vessel with the initial sodium backward flow from the H/L pipe, as shown in Fig. 5.4.

e) Void insertion (Fig. 5.8)

The void ratio in the reactor lower plenum reached a local maximum of 1.1% when the C/L sodium flow stopped at 15 seconds. Although the void in the lower plenum flowed to the core along with the non-leak loop sodium circulation, its void ratio increased still further to 1.5% at 32 seconds. This was because the lower plenum pressure was decreased by the R/D(1) release and the pump trip. The reactor core void ratio stayed at almost zero until 10 seconds, and then the void ratio began to increase. The core void ratio reached a maximum value of 0.94% at 33 seconds. After that, the void ratio gradually fell.

(2) Reactor core safety

The computer calculation indicated that the void ratio at the reactor core reached a maximum of 0.94% at 33 second. As the void reactivity with a 100% void ratio is 4.9$, the maximum void reactivity in case of one DEG CO_2 leak is calculated below.

4.9$ * 0.94% = 0.046$

The core is hardly affected at all by this level of void reactivity.

The solid reaction product (Na_2CO_3) in the core was estimated to be 117g at maximum. This amount of the reaction product formed a layer approximately 0.1mm thick on the fuel assembly.

Layer thickness of reaction product on fuel assemblies
= (Reaction product weight / Density) / (Flow cross section area of fuel assembly
* Number of fuel assemblies)
= 0.0088cm = 0.088mm (close to 0.1mm)

Reaction product weight: 117g
Density: 2.53g/cm^3
Cross section area of fuel assembly: 53.12cm^2
Number of fuel assemblies: 99

Such a 0.1mm thick layer causes no sodium flow blockage in the fuel assembly. Even positing that the reaction product is concentrated on only one fuel assembly for conservative evaluation, the layer thickness is approximately 10mm. Even this thickness doesn't block the sodium flow in the assembly.

5.4 Conclusions

The effect of the CO_2 leak on the reactor core and the primary sodium circuit was evaluated by the computer code. The analysis predicted that the rise of the void ratio and the reaction products have no serious impact on the core. The pressure and temperature rise also have no effect on the structural integrity of the primary sodium circuit.

The analysis was based on several assumptions regarding the sodium / CO_2 reaction. Therefore, the analysis must be regarded as sufficient only for the preliminary stage of planning. The sodium/CO_2 chemical reaction formula and the reaction product behaviors in sodium need to be experimentally investigated to improve the calculation accuracy.

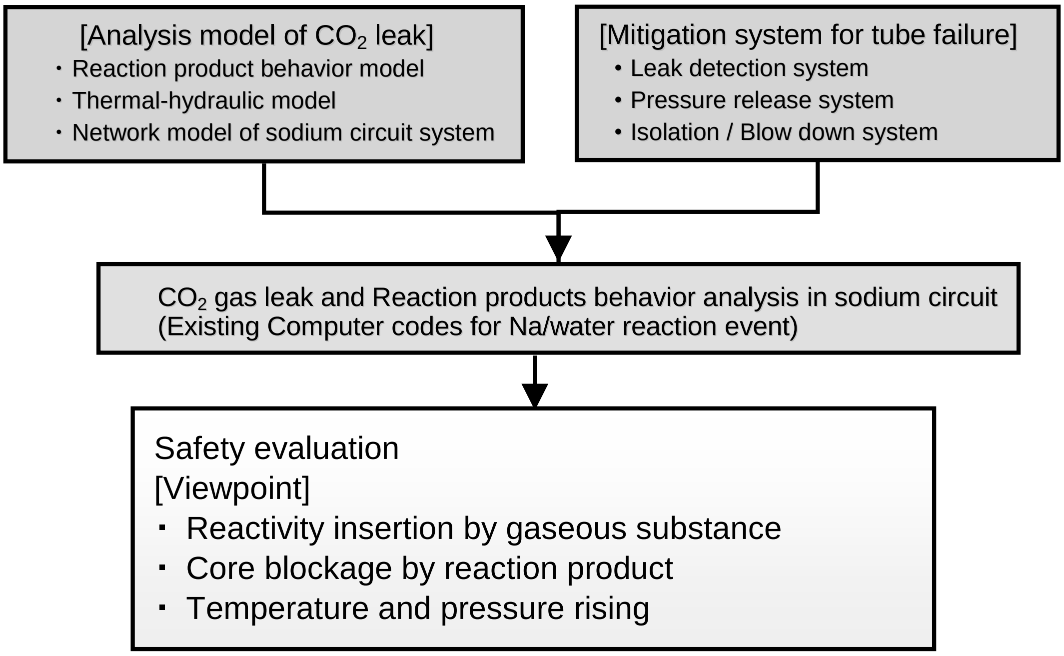

Fig. 5.1 CO_2 gas leak analytical evaluation procedure

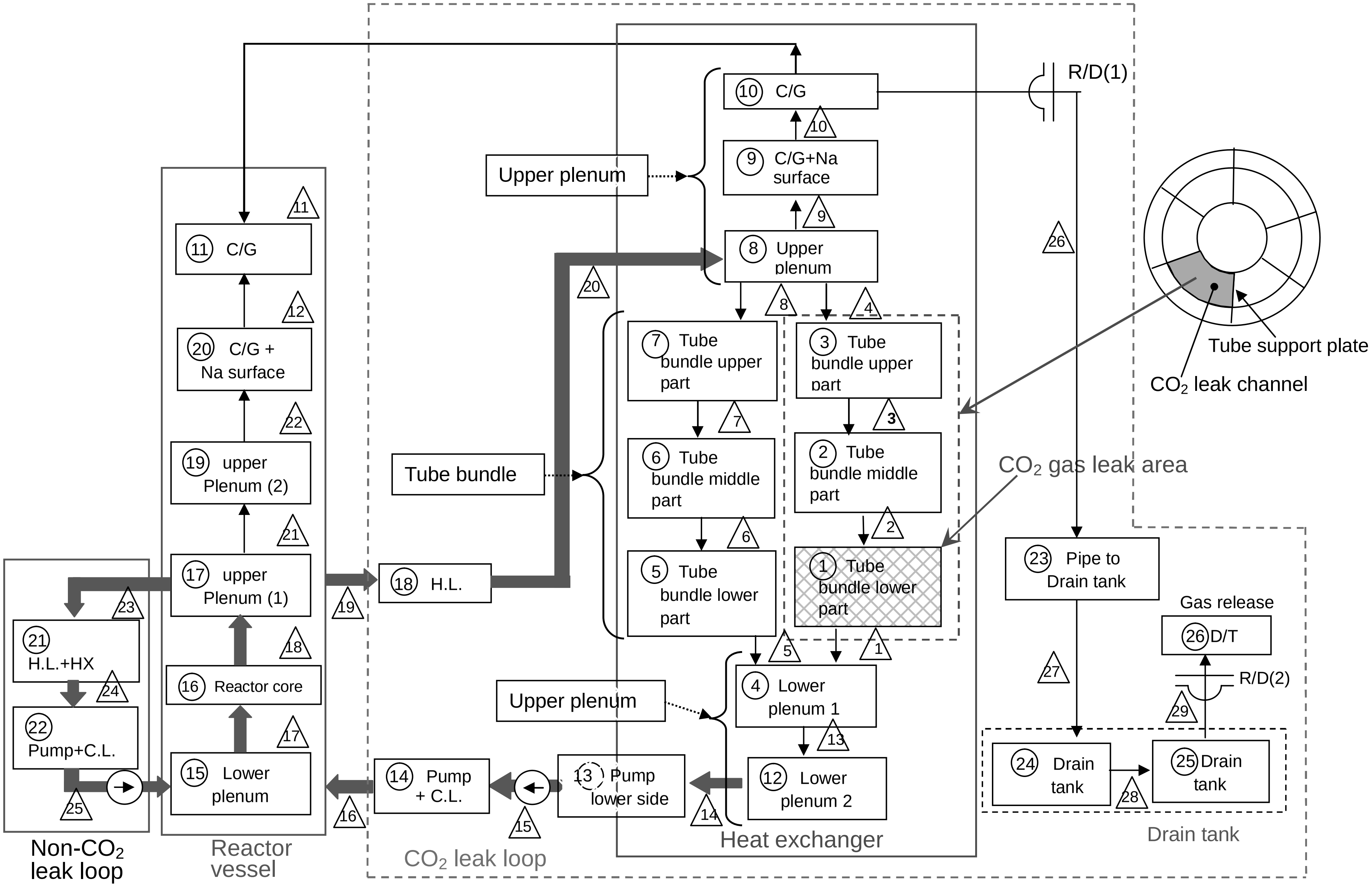

Fig. 5.2 Analytical model of reaction products behavior

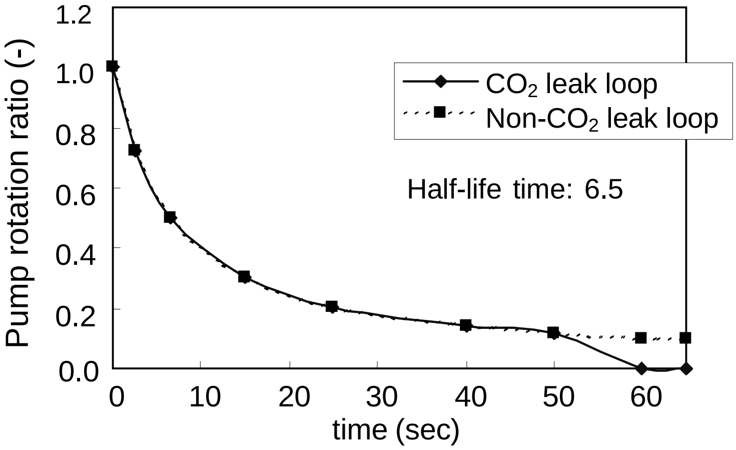

Fig. 5.3 Sodium primary Pump coast down curve

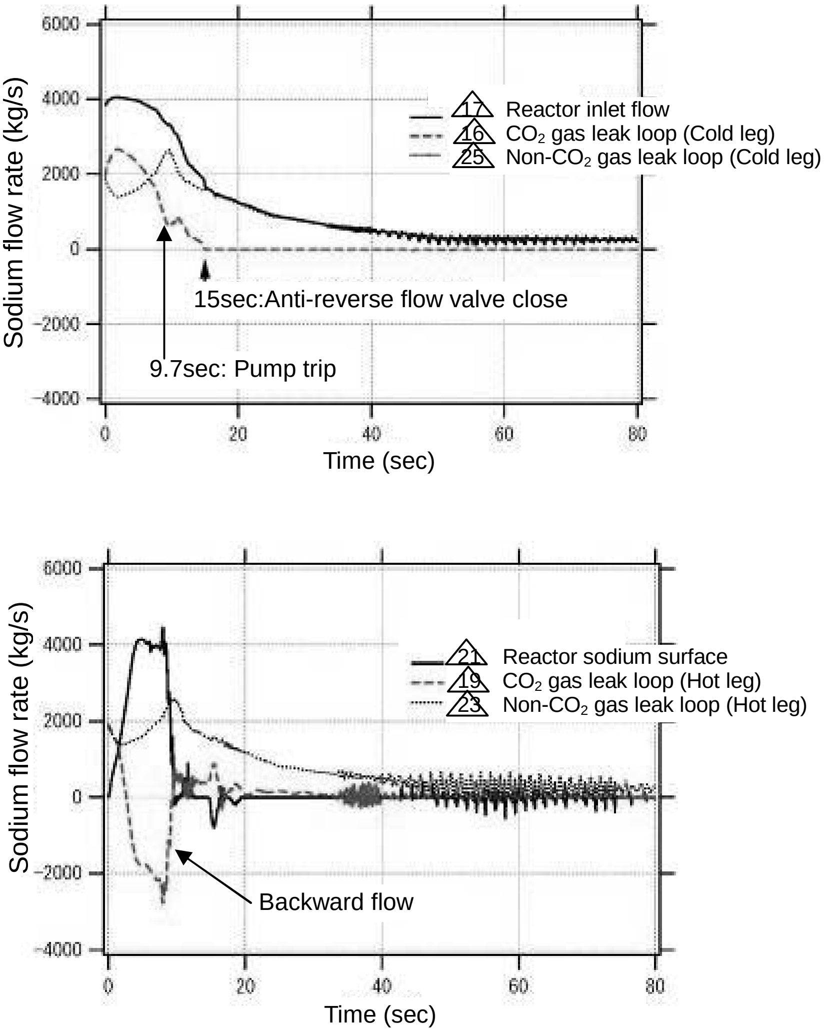

Fig. 5.4 Sodium flow rate transition

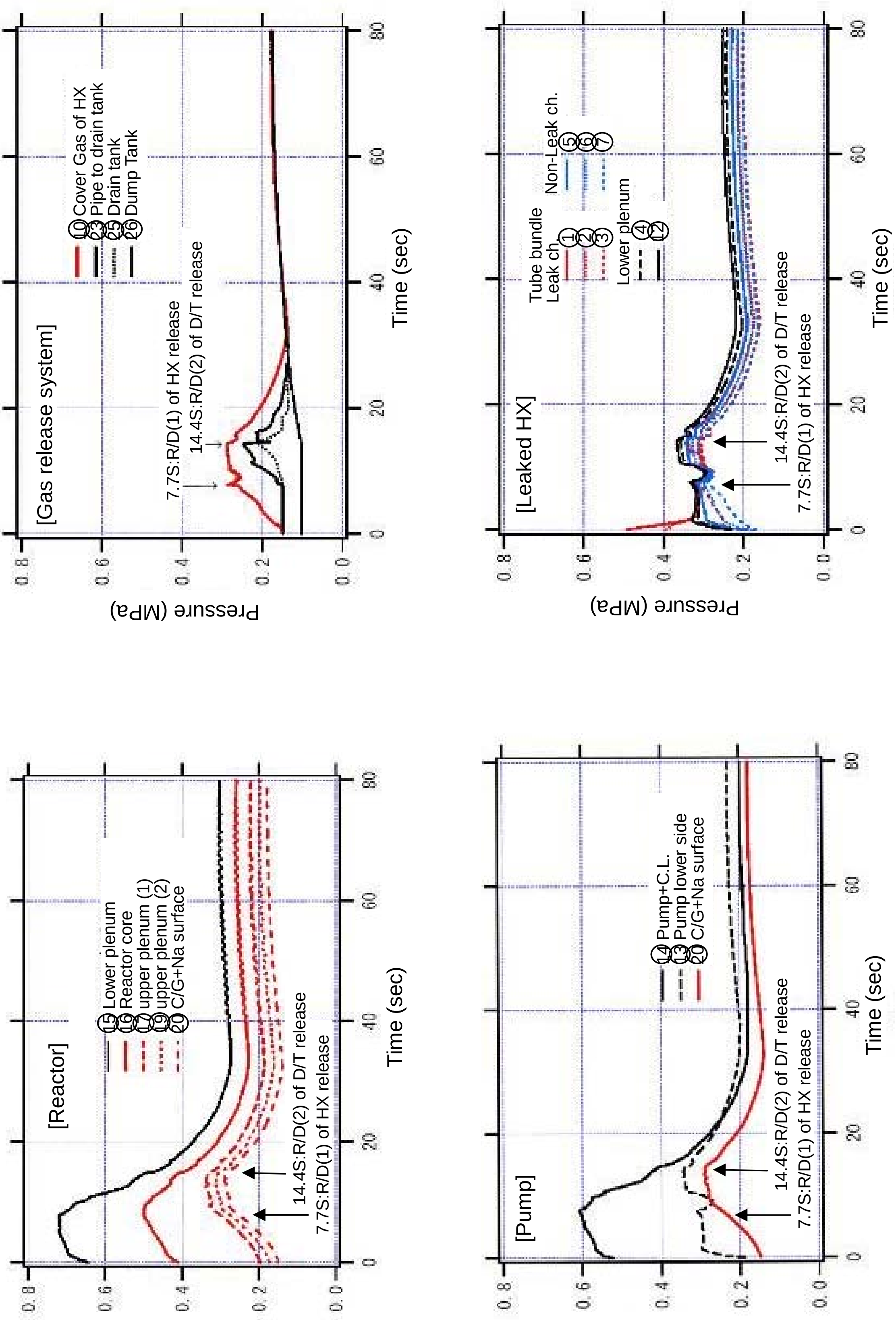

Fig. 5.5 Pressure transient

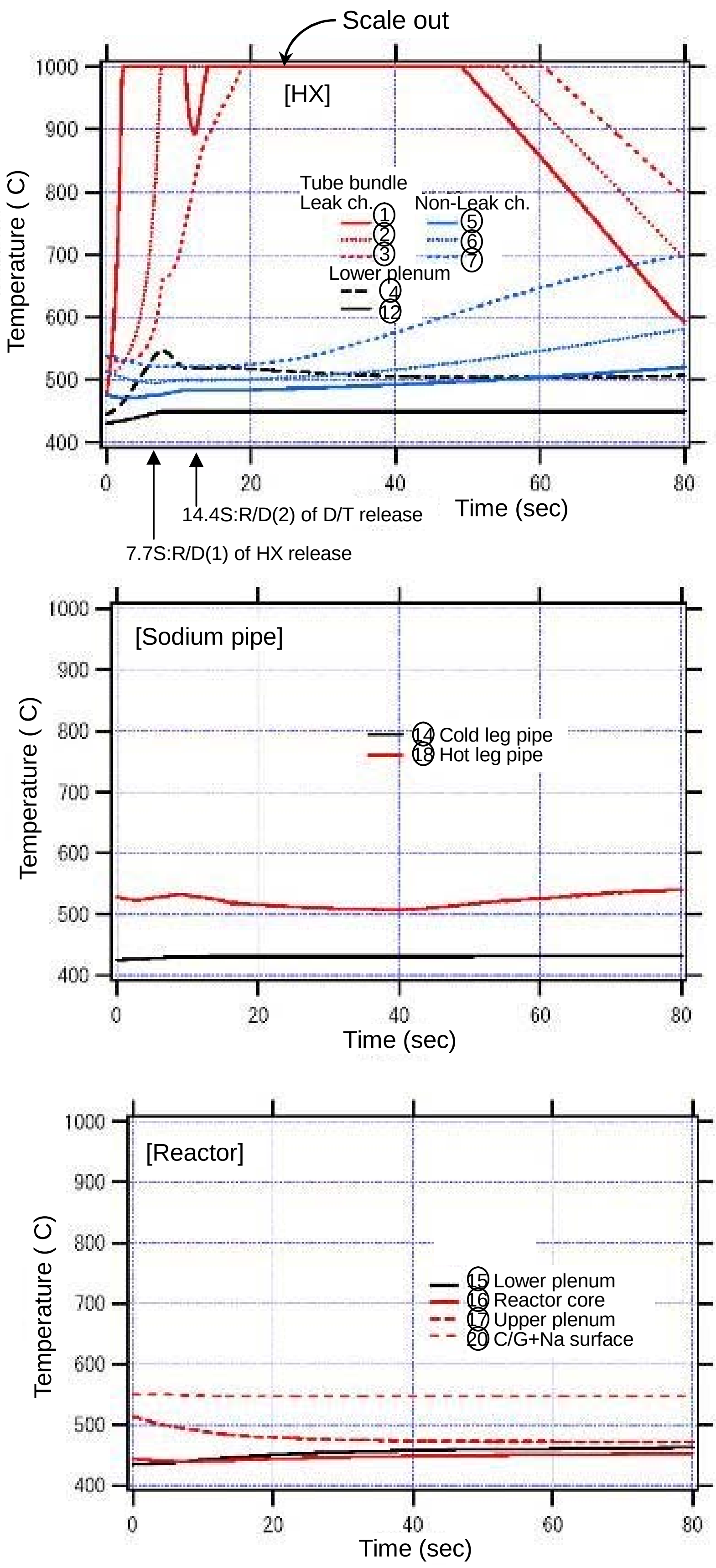

Fig. 5.6 Temperature transient

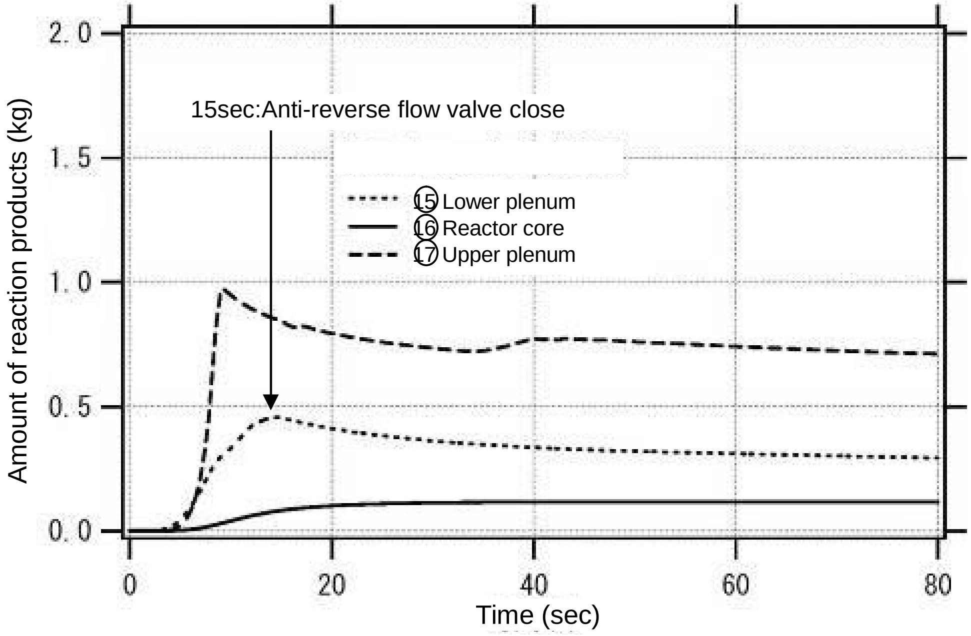

Fig. 5.7 Reaction product behavior in reactor

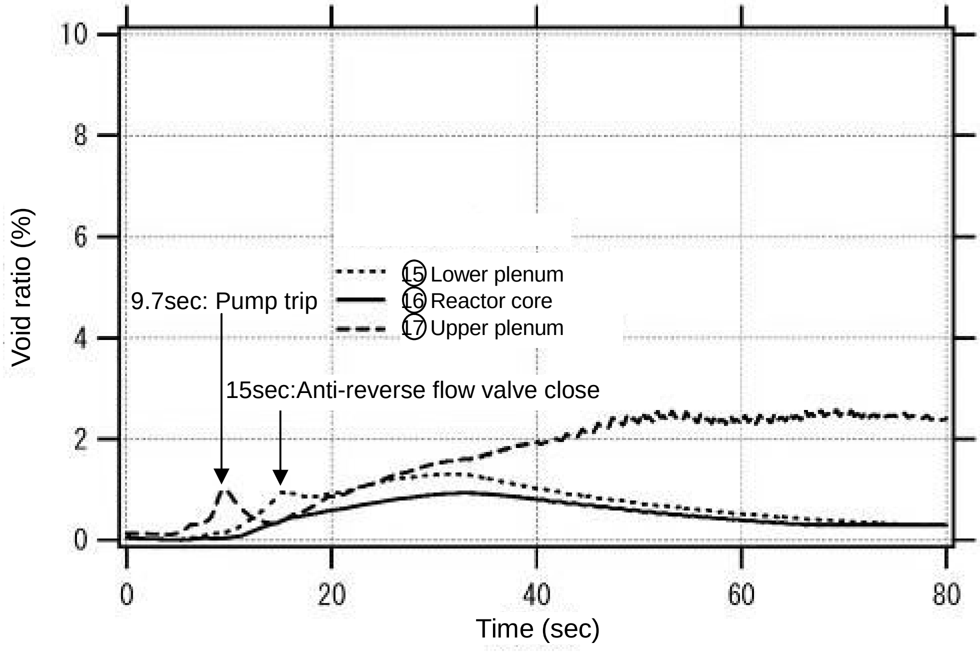

Fig. 5.8 Void ratio transient in reactor

6. Material tests in super-critical CO_2 environment

6.1 Introduction

Austenitic steel and ferritic steel material tests had been executed in a CO_2 environment for gas cooled reactors. [2]~[4] These studies, however, had been mainly done under sub-critical conditions.

New tests of materials have been carried out in super-critical conditions. The tested materials were 12Cr steel and 316FR, candidates for fast reactors. Material weight changes due to corrosion have been measured, and tentative corrosion and carbonization formulas were obtained. The one of the most significant corrosion issues is that oxide formation and oxide separation occur alternately and repeatedly. This phenomenon potentially causes rapid corrosion (”breakaway”). Therefore, the material tests also have been conducted, observing for breakaway.

6.2 Test apparatus and test conditions

Figure 6.1 is a schematic layout and an outside view of the super-critical CO_2 material test apparatus. The test apparatus consists of a CO_2 supply area, a corrosion test area and a CO_2 circulation loop. The CO_2 gas pressure was controlled by a compressor and a pressure regulator at the CO_2 supply area. The CO_2 gas is heated up to 200°C by a pre-heater before entering the test area. The CO_2 flow is divided into five lines, and temperatures of the lines in the test section were set at 400°C, 500°C, 550°C or 600°C. The test specimens were taken out every 1000hr to be inspected. A moisture meter and an oxygen meter are installed in the CO_2 circulation loop.

More than 99.995% CO_2 gas was used for the test, and its purity was confirmed before testing. The oxygen concentration and water vapor condensation temperature were below 5ppm and -76°C, respectively (Table 6.1).

Chemical components of the test materials before testing are shown in Tables 6.2 and 6.3. 316FR is the austenitic steel developed in Japan, and it has been applied to the heat exchangers of "JOYO" reactor. 12Cr steel is a candidate for the next SFR due to its good thermal conductivity and high temperature strength.

6.3 Test results

(1) Cross section observation

Cross sections of the 12Cr steel specimen are shown in Fig. 6.2(a),(b). Two oxide layers were formed on the surface. The inner layer was a fine oxide, and the outer layer was a porous oxide. The layer developed more under high temperature conditions. A diffusion layer was partially formed between the lower oxide layer and the base metal.

The thickness of the diffusion layer was less than 10μm, and it was hardly dependent on the test temperatures and time periods.

EPMA (Electron Probe Microscopic Analyzer) analysis results of 12Cr steel are shown in Fig. 6.3(500°C), Fig. 6.4(550°C) and Fig. 6.5(600°C). The upper graphs of each figure show the distributions of Fe, Cr, Ni, Cu and O, and the lower graphs show the Carbone distributions. Three phases (Fe-Cr phase, Fe-Cr-O phase and Fe-O phase) were observed in the material surface. The Fe-Cr phase is the base metal. The Fe-Cr-O phase is the inner fine oxide layer, and the Fe-O phase is the outer porous oxide. X-ray diffraction analysis showed that the outer porous Fe-O phase consisted of Fe_2O_3 and Fe_3O_4. The inner fine Fe-Cr-O phase was assumed to be $Fe(Fe_{1-x},Cr_x)_2O_4$ judging from its dual oxide layer structure. [5] The base metal surface was carbonized at ~500μm in depth.

Figure 6.4 shows an unusual distribution. The phases were stacked in the sequence [$Fe_2O_3 \bullet Fe_3O_4$ – $Fe(Fe_{1-x},Cr_x)_2O_4$ – $Fe_2O_3 \bullet Fe_3O_4$ – $Fe(Fe_{1-x},Cr_x)_2O_4$ – Base metal]. This distribution indicates that once an oxide layer was formed on the surface, the layer was detached, and then a new oxide layer appeared again at the same area. Repetition of oxide layer removal and regeneration leads to "breakaway". It was, however, concluded from microscopic observations and weight change measurements that no breakaway occurred under this test condition (<600°C, <5000hr).

Figure 6.6 shows cross sections of the 316 FR specimens. Although oxides were partially observed on the surface, an oxide layer structure was not formed. EPMA analysis results are shown in Fig. 6.7(500°C), Fig. 6.8 (550°C) and Fig. 6.9 (600°C). The concentrations of the base metal constituents on the surface (Fe, Cr and Ni) indicated no change. The material surface was, however, a little carbonized at ~100μm in depth.

(2) Weight change measurement

Weight changes of the 12Cr steel and 316FR test specimen are shown in Figs. 6.10 and 6.11, respectively. The 12Cr steel weight increased with time, tracing a parabolic curve. The oxide detachment and regeneration was indicated in the EPMA analysis. This however didn't lead to breakaway, because no rapid weight change was observed in the corrosion curves.

Compared with the 12Cr steel weight change, the 316FR exhibited good corrosion resistance. The weight seemed to have rapidly increased at 600°C and 550°C after 4000 hours, continuing up to 5000 hours. This was considered to be affected by a little moisture mixing from atmosphere due to a CO_2 gas cylinder exchange.

(3) Corrosion and carbonization behavior of 12 Cr steel

The formulas of corrosion and carbonization of the 316 FR could not be determined, because their amounts were too small. The formulas of corrosion and carbonization of the 12Cr steel could be described.

As shown in Fig. 6.10, the 12Cr steel corrosion behavior follows parabolic curves (1). Oxidation rate constant *Kp* of the formula (1) was assumed to be derived from the Arrhenius type equation (2), and the values of K_0 and Q therein were determined by the experimental data.

$$\Delta W = Kp\sqrt{t} \quad \cdots\cdots (1)$$

$$Kp = K_0 \exp\left(-Q / RT\right) \quad \cdots\cdots (2)$$

ΔW: Material weight change (g)
Kp: Oxidation rate constant
t: Time (sec)
K_0: Constant [81.995]
Q: Activation energy (J/K·mol) [5.525e4]
R: Gas constant (J/K·mol)
T: Temperature (K)

Figure 6.12 shows both the *Kp* of each temperature level (400°C, 500°C, 550°C, 600°C) and the fitting line determined by the *Kp* formula (the Arrhenius type equation) (2). The *Kp* formula (2) was very consistent with the experimental data.

The carbonization formula of the 12Cr steel was obtained in a way similar to that of the 12Cr corrosion formula. The carbon concentration distributions (Figs. 6.3~6.5) were integrated to determine carbonization amounts on the material surface. The relation of the carbonization amounts and temperatures is shown in Fig. 6.13. Figure 6.14 shows the carbonization rate coefficient at each temperature level (500°C, 550°C, 600°C). This graph also shows the fitting line determined by the Arrhenius type equation (3) below. The *Kp(c)* formula (3) also exhibits good agreement with the experimental data.

$$Kp_{(C)} = 317.65\exp\left(-7.918\times10^{4} / RT\right) \quad \cdots\cdots (3)$$

6.4 Conclusions

[12Cr-steel]

(1) Two oxide layers were stably formed on the surface.

(2) No breakaway occurred (<600°C, <5000hr).

(3) An amount of corrosion was 170g/m^2 after an exposure of 600°C-5000hours.

(4) Corrosion and carbonization formulas were determined by experimental data.

[316FR]

(1) 316FR exhibited good corrosion resistance.

(2) The amount of corrosion was 5g/m^2 after an exposure of 600°C-5000hours.

Table 6.1 CO_2 analysis before testing

purity	CO_2	> 99.995%
impurities	O_2	< 5ppm
	N_2	< 25ppm
	H_2	< 5ppm
	CH_4	< 10ppm
	H_2O	< −76℃
	C_2H_6	< 1ppm

inspected by Japan fine Products Co. Ltd

Table 6.2　316FR constituent before testing

(mass %)

C	Si	Mn	P	S	Cu	Ni	Cr
0.01	0.59	0.84	0.026	0.003	0.26	11.19	16.87

Mo	V	N	B	T	As	Co	O
2.23	0.08	0.08	0.0006	0.007	0.004	0.06	0.0037

Table 6.3　12Cr steel constituent before testing

(mass %)

C	Si	Mn	P	S	Cu	Ni	Cr
0.11	0.26	0.64	0.016	0.002	1.03	0.39	10.87

W	Mo	V	Nb	Al sol	N total	B
1.86	0.31	0.20	0.054	0.001	0.064	0.0034

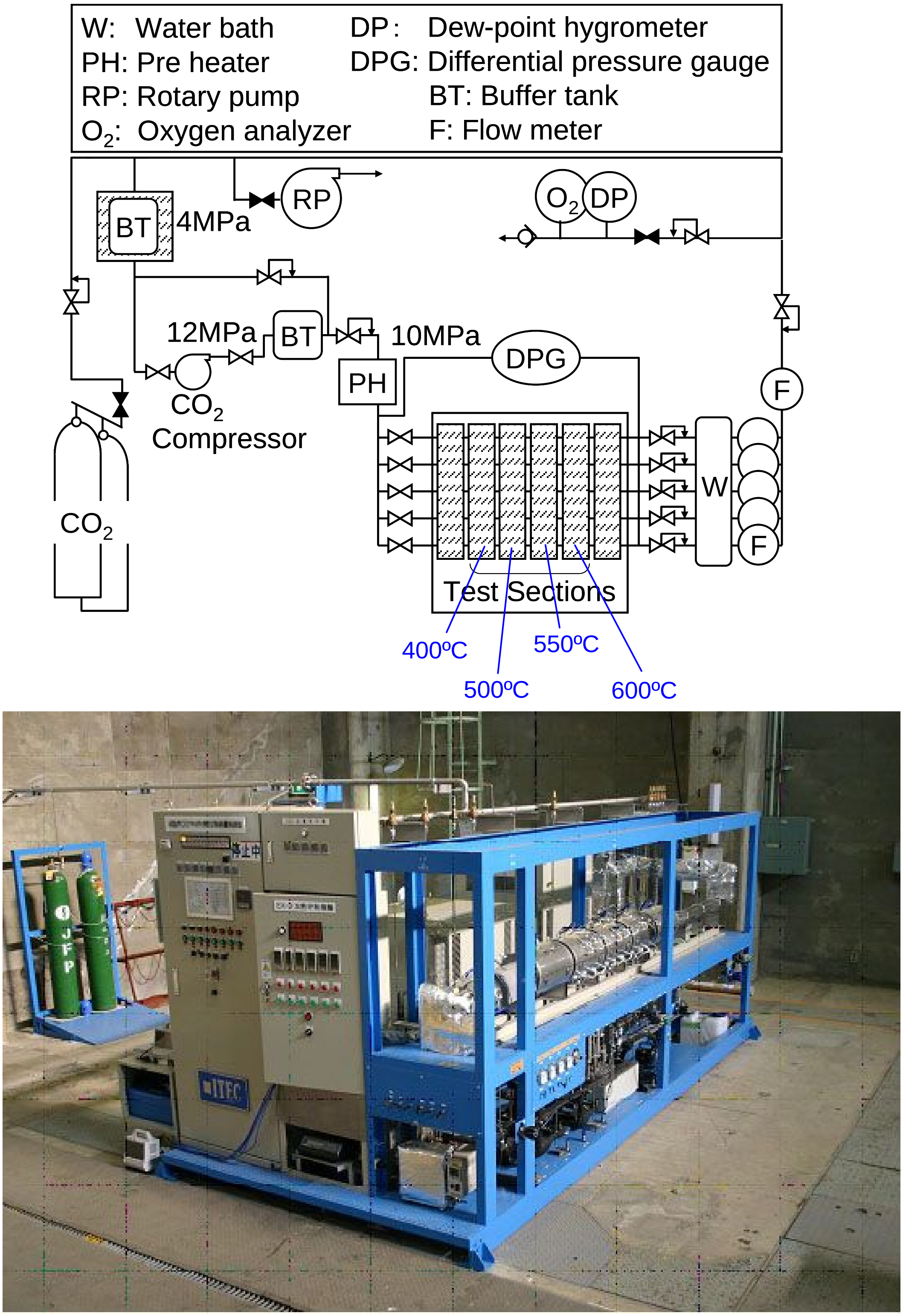

Fig. 6.1 Super-critical CO_2 Corrosion Test Apparatus

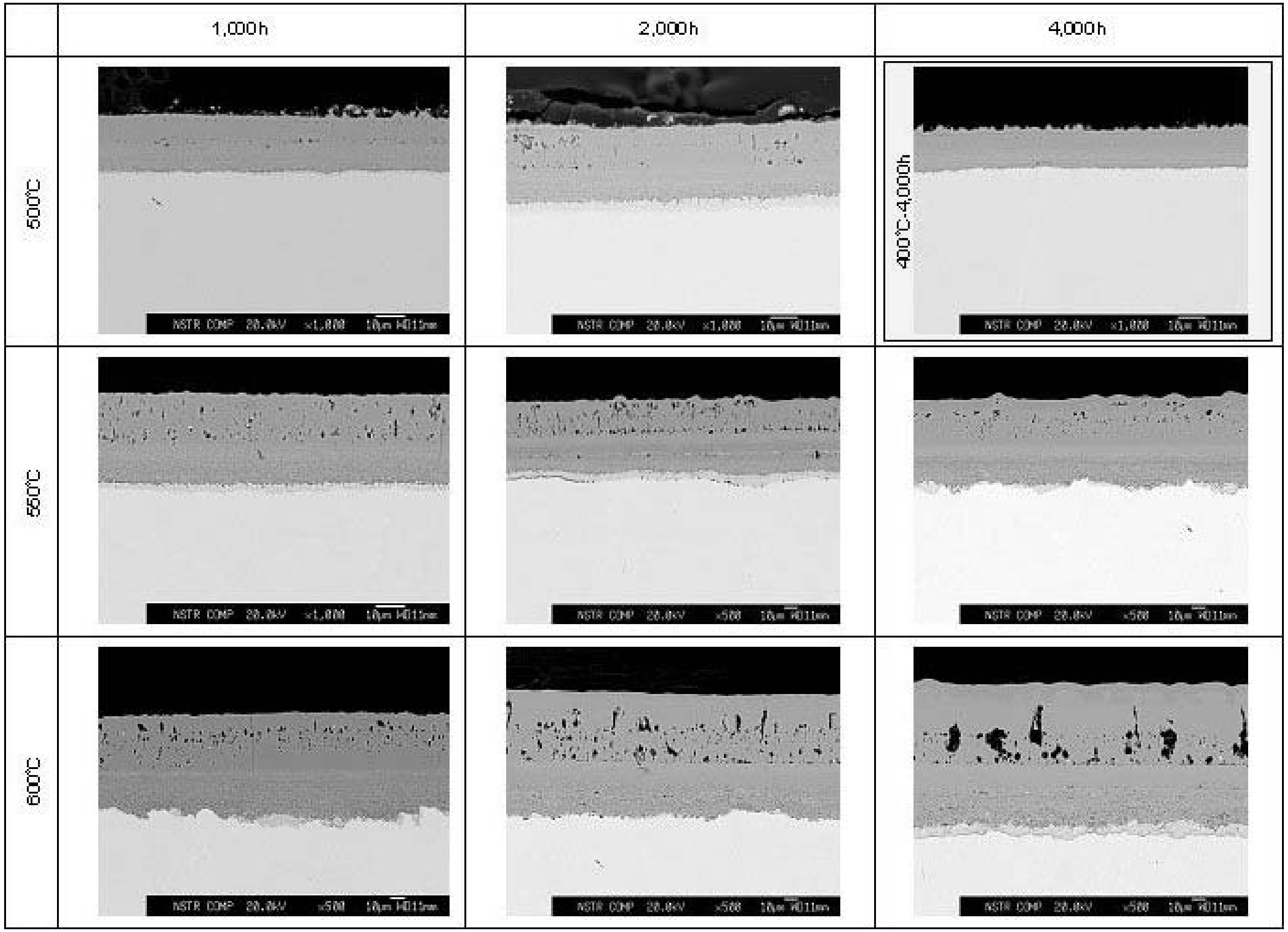

Fig. 6.2(a) Cross section of 12Cr steel test specimen

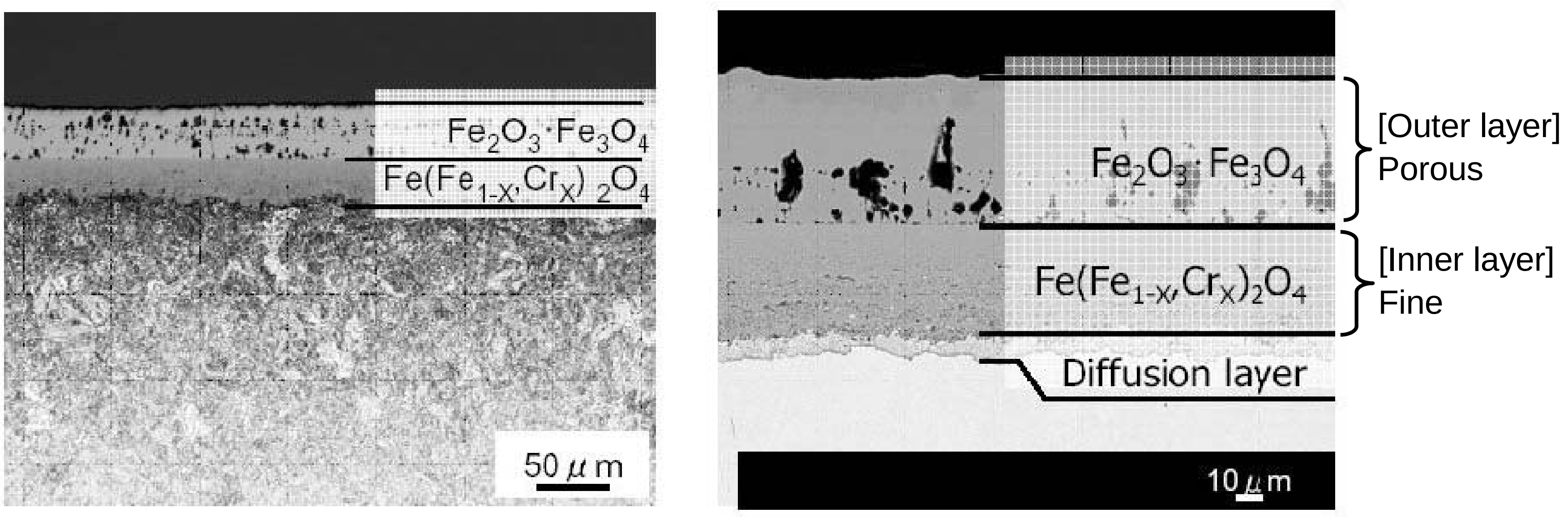

12Cr-steel, 600°C-1,000h

12Cr-steel, 600°C-4,000h

Fig. 6.2(b) Cross section of 12Cr steel test specimen

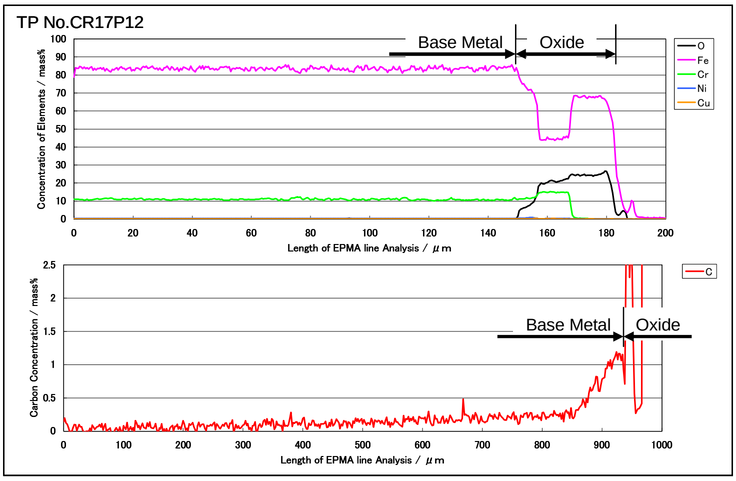

Fig. 6.3 EPMA analysis (12Cr steel 500°C 2000hr)

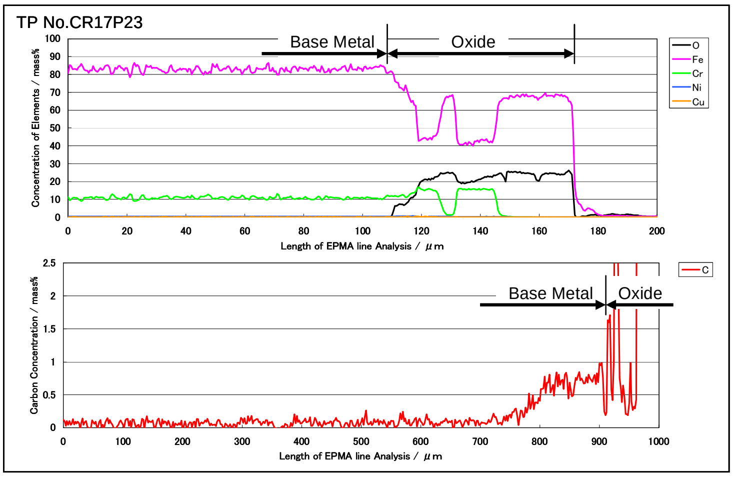

Fig. 6.4 EPMA analysis (12Cr steel 550°C 2000hr)

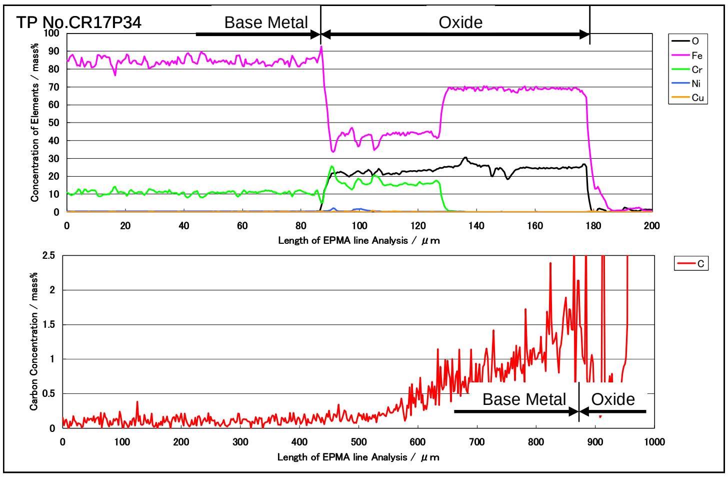

Fig. 6.5 EPMA analysis (12Cr steel 600°C 2000hr)

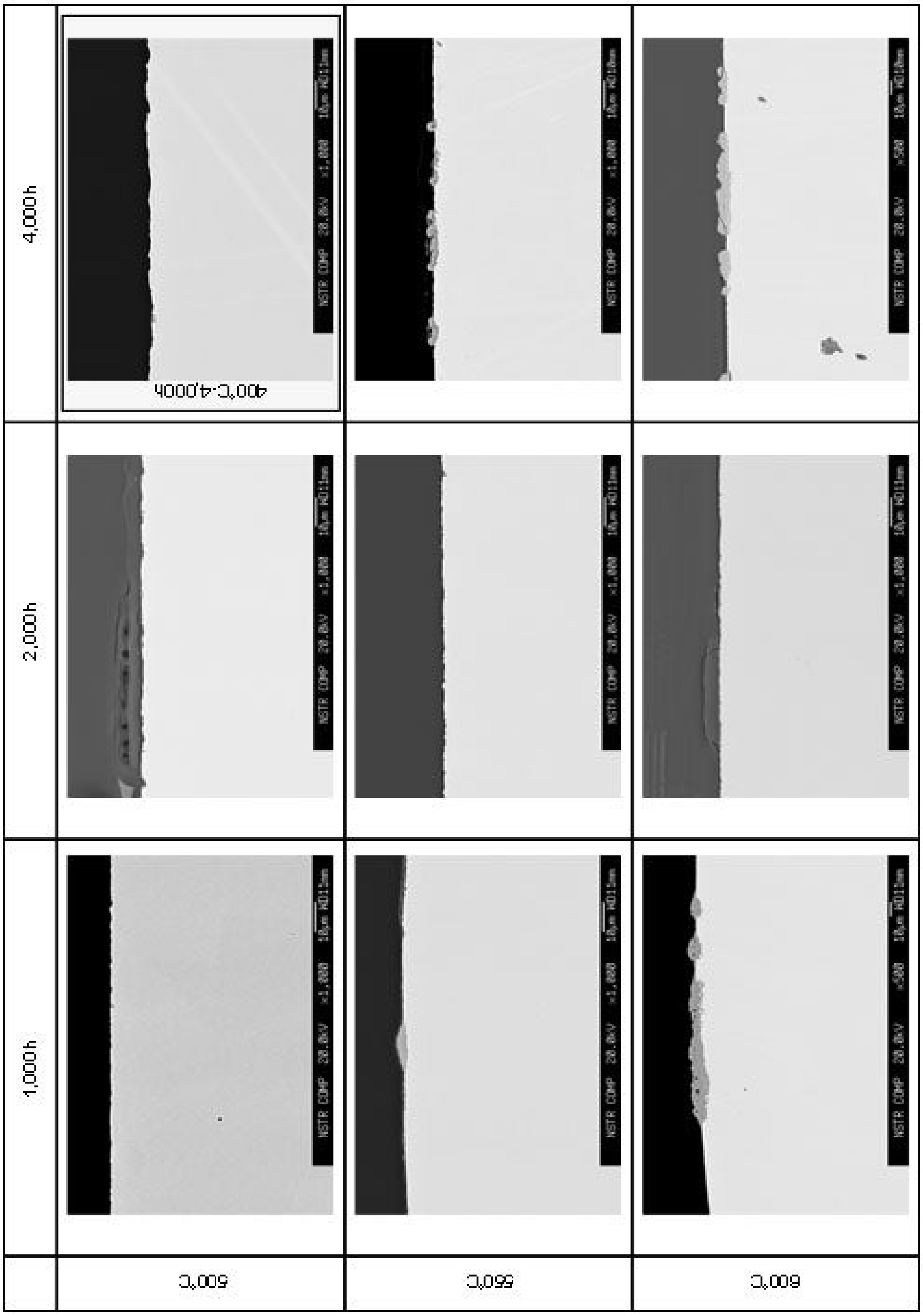

Fig. 6.6(a) Cross section of 316FR test specimen

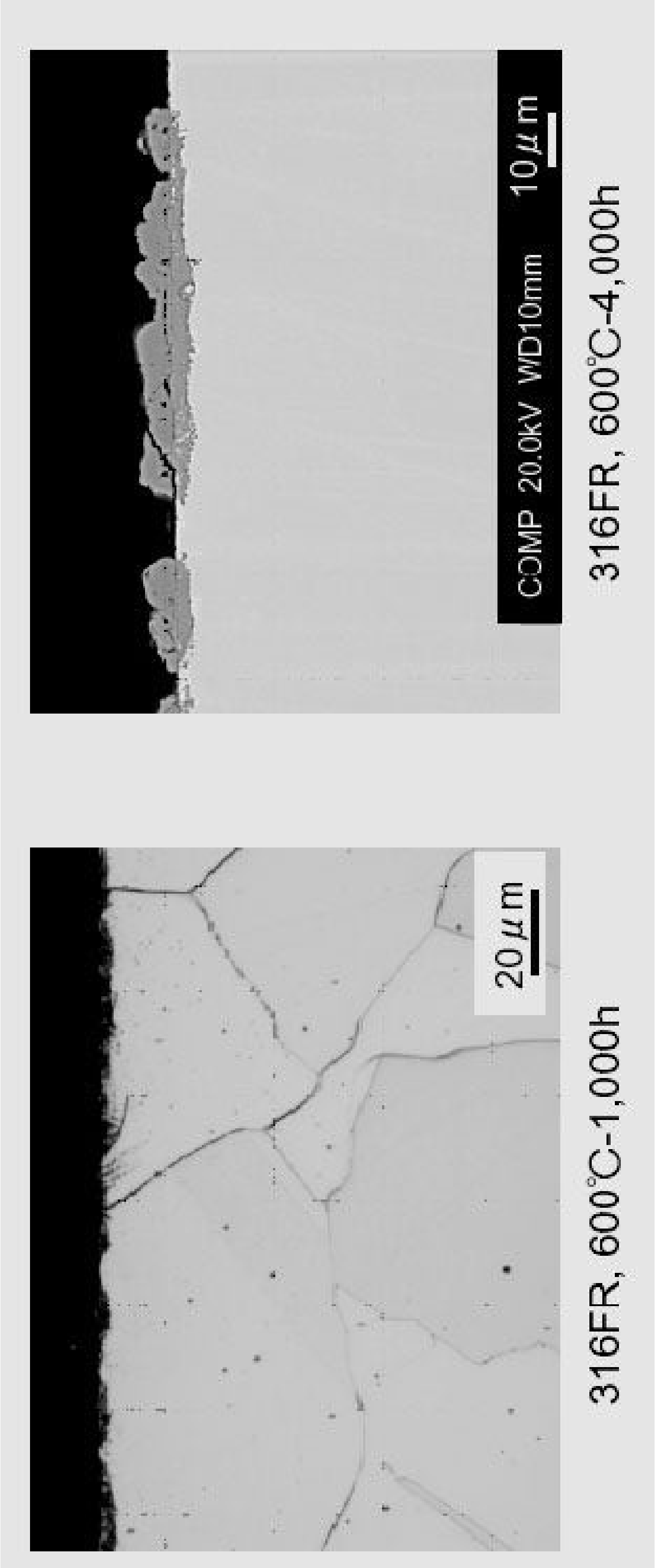

Fig. 6.6(b) Cross section of 316FR test specimen

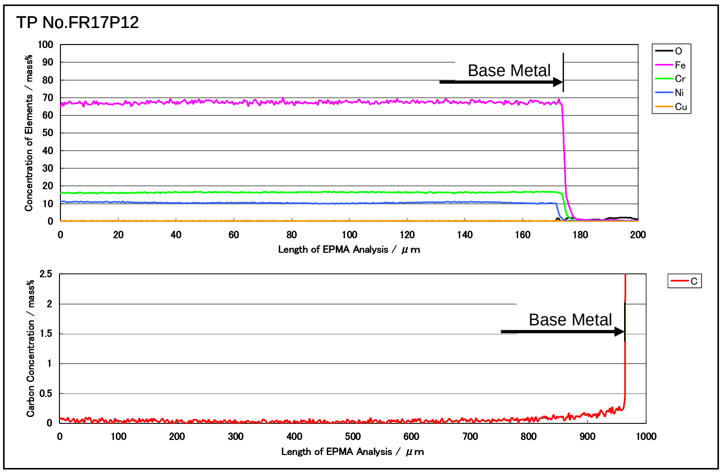

Fig. 6.7 EPMA analysis (316FR 500°C 2000hr)

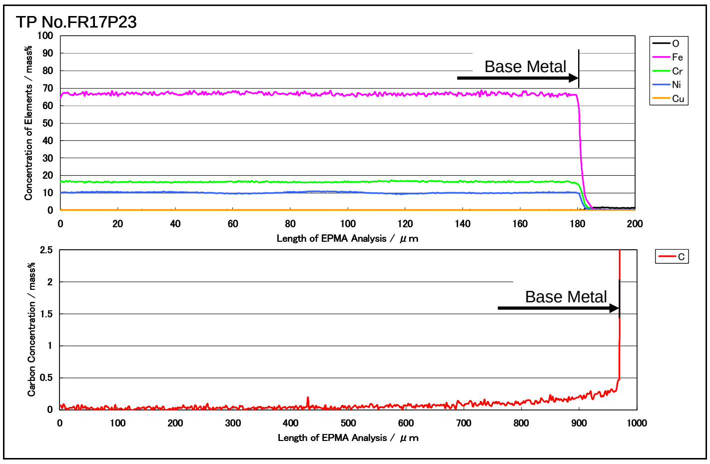

Fig. 6.8 EPMA analysis (316FR 550°C 2000hr)

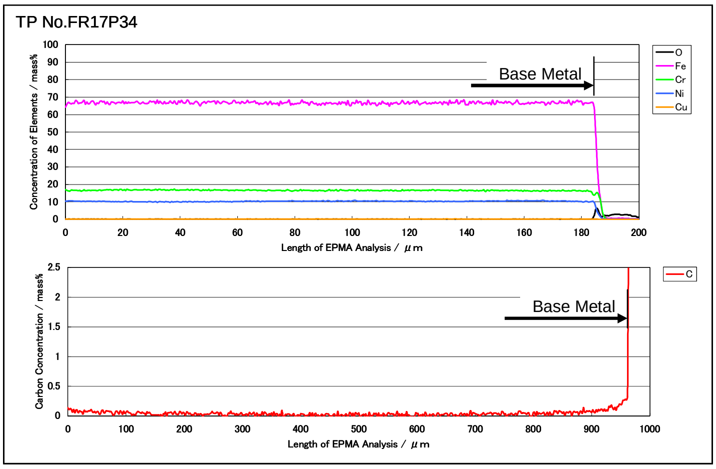

Fig. 6.9 EPMA analysis (316FR 600°C 2000hr)

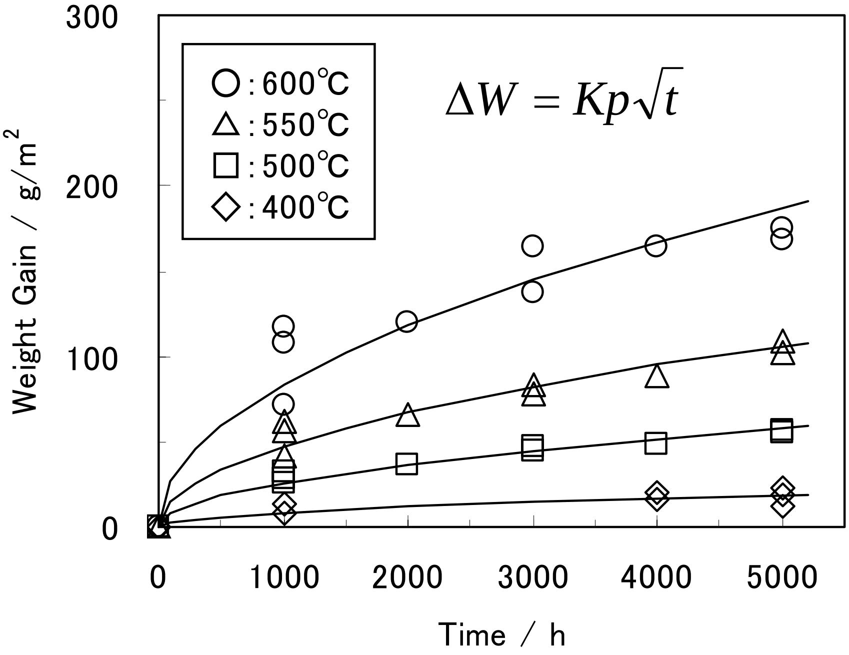

Fig. 6.10 12Cr steel weight change

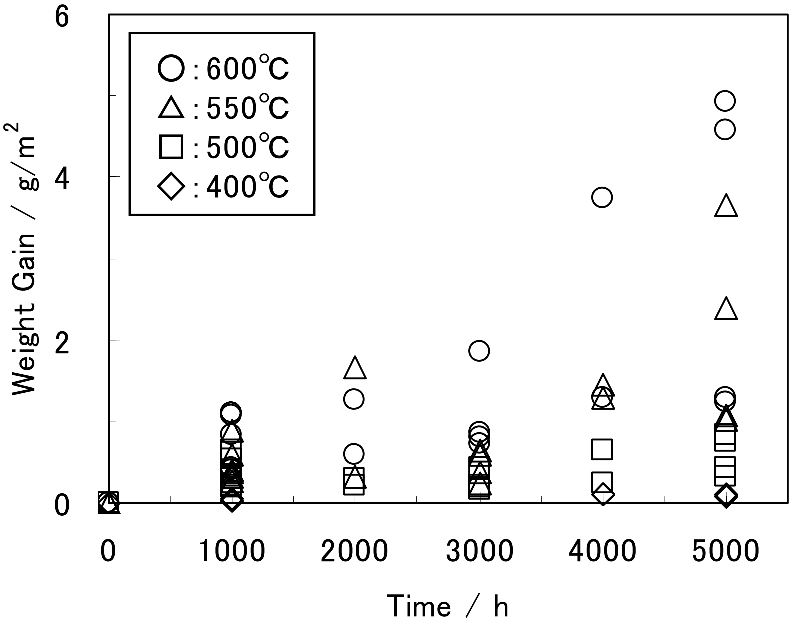

Fig. 6.11 316FR weight change

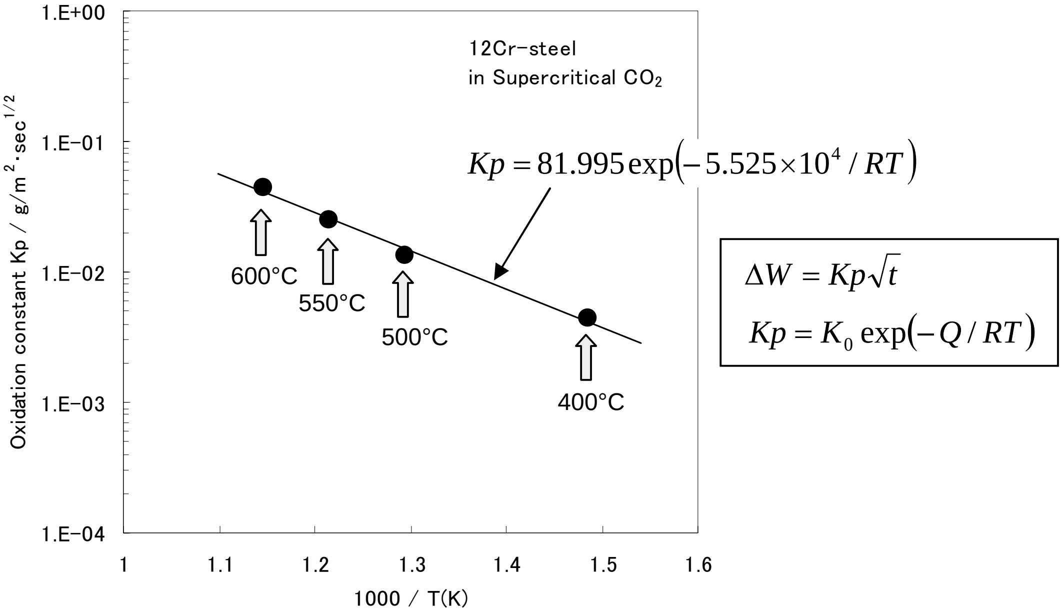

Fig. 6.12 Oxidation constant of 12Cr steel in SC-CO_2

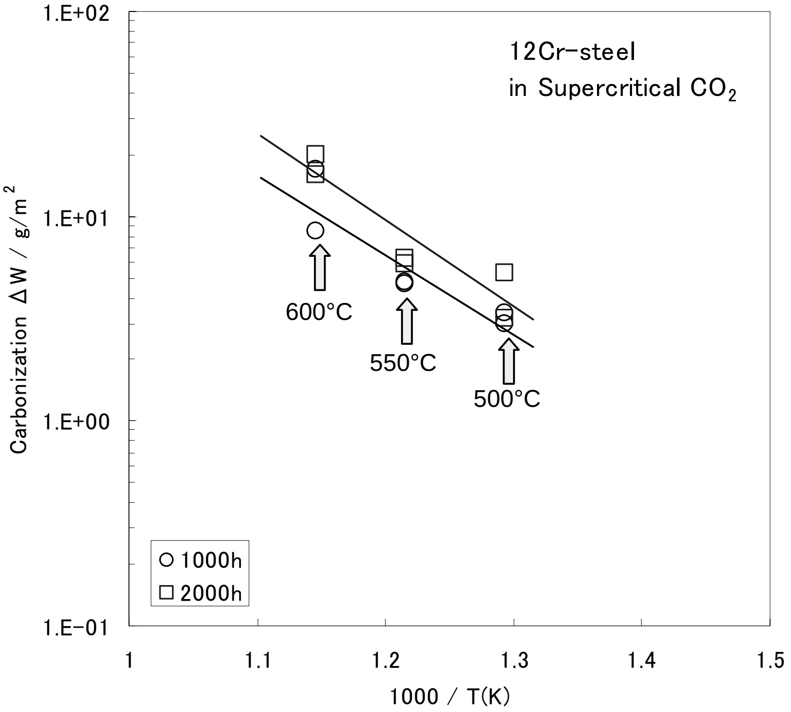

Fig. 6.13 Carbonization amount of 12Cr steel in SC-CO_2

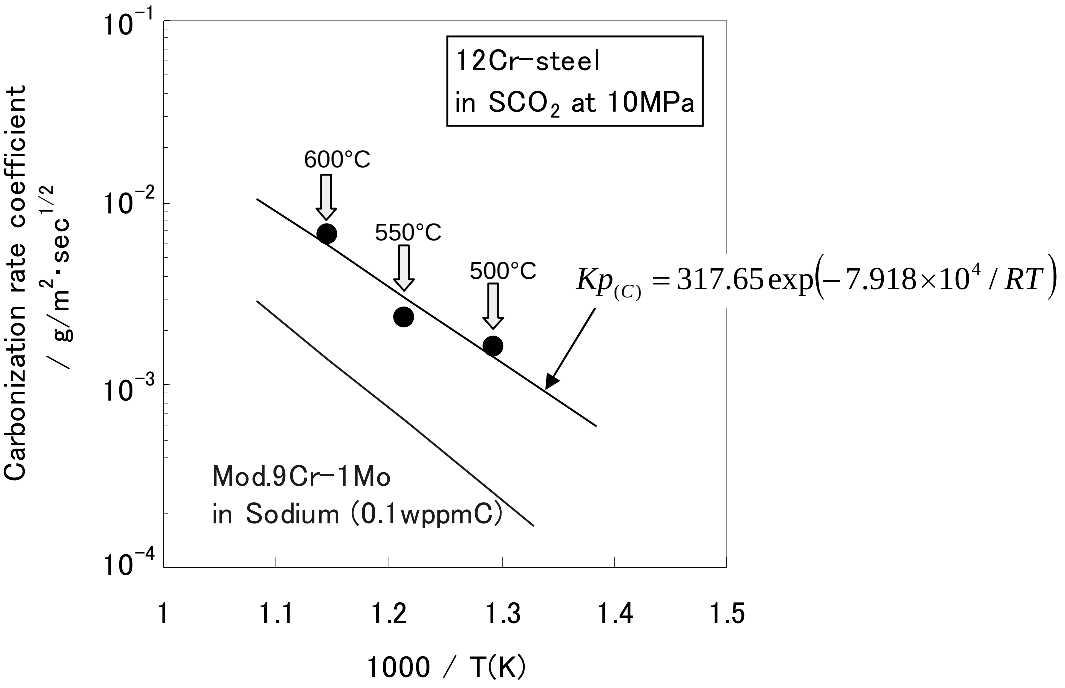

Fig. 6.14 Carbonization constant of 12Cr steel in SC-CO$_2$

7. Afterword

The SC-CO_2 turbine SFR that eliminates secondary sodium circuit was designed as a preliminary stage. The volume of the reactor building was estimated by taking account of the size and the layout of the main components. Safety evaluation for a CO_2 gas leak was also analyzed by a computer code. The fundamental experimental data have been obtained from the SC-CO_2 test loop test, the sdium/CO_2 reaction test and the material test.

These plant system design, computer calculation and tests are feasibility phase, and the more detailed design and further experiments are necessary to evaluate the SC-CO_2 SFR system performance. On the basis of the previous studies, comprehensive R&D plans hereafter will be determined.

References

[1] N. Tsuzuki , Y. Kato , and T. Ishizuka , “High Performance Heat Exchanger” , Proc. Heat SET 2005 , Heat Transfer in Components and Systems for Sustainable Energy Technologies , Grenoble , France , April 5-7 , 2005.

[2] J. W. Taylor , P. V. Trotsenberg , Proc. Int. Conf. Corr. Steel in CO_2 (1974) 180-192.

[3] A. M. Prichard , A. E. Ttruswell , Proc. Conf. Corr. Steel in CO_2 (1974) 234-246.

[4] E. Loewen and K. Weaber , Trans. ANS2003 Annual Meeting (2003) 424-425.

[5] D. R. Gaskell , Introduction to the Thermodynamics of Materials , Third Edition , ISBN 1-56032-432-5 , (1995)

This is a blank page.

国際単位系（SI）

表１．SI 基本単位

基本量	SI 基本単位	
	名称	記号
長さ	メートル	m
質量	キログラム	kg
時間	秒	s
電流	アンペア	A
熱力学温度	ケルビン	K
物質量	モル	mol
光度	カンデラ	cd

表２．基本単位を用いて表されるSI組立単位の例

組立量	SI 基本単位	
	名称	記号
面積	平方メートル	$\mathrm{m^2}$
体積	立法メートル	$\mathrm{m^3}$
速さ，速度	メートル毎秒	m/s
加速度	メートル毎秒毎秒	$\mathrm{m/s^2}$
波数	毎メートル	m-1
密度（質量密度）	キログラム毎立法メートル	$\mathrm{kg/m^3}$
質量体積（比体積）	立法メートル毎キログラム	$\mathrm{m^3/kg}$
電流密度	アンペア毎平方メートル	$\mathrm{A/m^2}$
磁界の強さ	アンペア毎メートル	A/m
（物質量の）濃度	モル毎立方メートル	$\mathrm{mol/m^3}$
輝度	カンデラ毎平方メートル	$\mathrm{cd/m^2}$
屈折率	（数の）１	1

表３．固有の名称とその独自の記号で表されるSI組立単位

組立量	SI 組立単位			
	名称	記号	他のSI単位による表し方	SI基本単位による表し方
平面角	ラジアン(a)	rad		$\mathrm{m\cdot m^{-1}=1}$(b)
立体角	ステラジアン(a)	sr(c)		$\mathrm{m^2\cdot m^{-2}=1}$(b)
周波数	ヘルツ	Hz		$\mathrm{s^{-1}}$
力	ニュートン	N		$\mathrm{m\cdot kg\cdot s^{-2}}$
圧力，応力	パスカル	Pa	$\mathrm{N/m^2}$	$\mathrm{m^{-1}\cdot kg\cdot s^{-2}}$
エネルギー，仕事，熱量	ジュール	J	N・m	$\mathrm{m^2\cdot kg\cdot s^{-2}}$
工率，放射束	ワット	W	J/s	$\mathrm{m^2\cdot kg\cdot s^{-3}}$
電荷，電気量	クーロン	C		s・A
電位差（電圧），起電力	ボルト	V	W/A	$\mathrm{m^2\cdot kg\cdot s^{-3}\cdot A^{-1}}$
静電容量	ファラド	F	C/V	$\mathrm{m^{-2}\cdot kg^{-1}\cdot s^4\cdot A^2}$
電気抵抗	オーム	Ω	V/A	$\mathrm{m^2\cdot kg\cdot s^{-3}\cdot A^{-2}}$
コンダクタンス	ジーメンス	S	A/V	$\mathrm{m^{-2}\cdot kg^{-1}\cdot s^3\cdot A^2}$
磁束	ウエーバ	Wb	V・s	$\mathrm{m^2\cdot kg\cdot s^{-2}\cdot A^{-1}}$
磁束密度	テスラ	T	$\mathrm{Wb/m^2}$	$\mathrm{kg\cdot s^{-2}\cdot A^{-1}}$
インダクタンス	ヘンリー	H	Wb/A	$\mathrm{m^2\cdot kg\cdot s^{-2}\cdot A^{-2}}$
セルシウス温度	セルシウス度(d)	℃		K
光束	ルーメン	lm	cd・sr(c)	$\mathrm{m^2\cdot m^{-2}\cdot cd=cd}$
照度	ルクス	lx	$\mathrm{lm/m^2}$	$\mathrm{m^2\cdot m^{-4}\cdot cd=m^{-2}\cdot cd}$
（放射性核種の）放射能	ベクレル	Bq		$\mathrm{s^{-1}}$
吸収線量，質量エネルギー分与，カーマ	グレイ	Gy	J/kg	$\mathrm{m^2\cdot s^{-2}}$
線量当量，周辺線量当量，方向性線量当量，個人線量当量,組織線量当	シーベルト	Sv	J/kg	$\mathrm{m^2\cdot s^{-2}}$

(a) ラジアン及びステラジアンの使用は、同じ次元であっても異なった性質をもった量を区別するときの組立単位の表し方として利点がある。組立単位を形作るときのいくつかの用例は表４に示されている。
(b) 実際には、使用する時には記号rad及びsrが用いられるが、習慣として組立単位としての記号“１”は明示されない。
(c) 測光学では、ステラジアンの名称と記号srを単位の表し方の中にそのまま維持している。
(d) この単位は、例としてミリセルシウス度m℃のようにSI接頭語を伴って用いても良い。

表４．単位の中に固有の名称とその独自の記号を含むSI組立単位の例

組立量	SI 組立単位		
	名称	記号	SI 基本単位による表し方
粘度	パスカル秒	Pa・s	$\mathrm{m^{-1}\cdot kg\cdot s^{-1}}$
力のモーメント	ニュートンメートル	N・m	$\mathrm{m^2\cdot kg\cdot s^{-2}}$
表面張力	ニュートン毎メートル	N/m	$\mathrm{kg\cdot s^{-2}}$
角速度	ラジアン毎秒	rad/s	$\mathrm{m\cdot m^{-1}\cdot s^{-1}=s^{-1}}$
角加速度	ラジアン毎平方秒	$\mathrm{rad/s^2}$	$\mathrm{m\cdot m^{-1}\cdot s^{-2}=s^{-2}}$
熱流密度，放射照度	ワット毎平方メートル	$\mathrm{W/m^2}$	$\mathrm{kg\cdot s^{-3}}$
熱容量，エントロピー	ジュール毎ケルビン	J/K	$\mathrm{m^2\cdot kg\cdot s^{-2}\cdot K^{-1}}$
質量熱容量（比熱容量），質量エントロピー	ジュール毎キログラム毎ケルビン	J/(kg・K)	$\mathrm{m^2\cdot s^{-2}\cdot K^{-1}}$
質量エネルギー（比エネルギー）	ジュール毎キログラム	J/kg	$\mathrm{m^2\cdot s^{-2}\cdot K^{-1}}$
熱伝導率	ワット毎メートル毎ケルビン	W/(m・K)	$\mathrm{m\cdot kg\cdot s^{-3}\cdot K^{-1}}$
体積エネルギー	ジュール毎立方メートル	$\mathrm{J/m^3}$	$\mathrm{m^{-1}\cdot kg\cdot s^{-2}}$
電界の強さ	ボルト毎メートル	V/m	$\mathrm{m\cdot kg\cdot s^{-3}\cdot A^{-1}}$
体積電荷	クーロン毎立方メートル	$\mathrm{C/m^3}$	$\mathrm{m^{-3}\cdot s\cdot A}$
電気変位	クーロン毎平方メートル	$\mathrm{C/m^2}$	$\mathrm{m^{-2}\cdot s\cdot A}$
誘電率	ファラド毎メートル	F/m	$\mathrm{m^{-3}\cdot kg^{-1}\cdot s^4\cdot A^2}$
透磁率	ヘンリー毎メートル	H/m	$\mathrm{m\cdot kg\cdot s^{-2}\cdot A^{-2}}$
モルエネルギー	ジュール毎モル	J/mol	$\mathrm{m^2\cdot kg\cdot s^{-2}\cdot mol^{-1}}$
モルエントロピー，モル熱容量	ジュール毎モル毎ケルビン	J/(mol・K)	$\mathrm{m^2\cdot kg\cdot s^{-2}\cdot K^{-1}\cdot mol^{-1}}$
照射線量（Ｘ線及びγ線）	クーロン毎キログラム	C/kg	$\mathrm{kg^{-1}\cdot s\cdot A}$
吸収線量率	グレイ毎秒	Gy/s	$\mathrm{m^2\cdot s^{-3}}$
放射強度	ワット毎ステラジアン	W/sr	$\mathrm{m^4\cdot m^{-2}\cdot kg\cdot s^{-3}=m^2\cdot kg\cdot s^{-3}}$
放射輝度	ワット毎平方メートル毎ステラジアン	$\mathrm{W/(m^2\cdot sr)}$	$\mathrm{m^2\cdot m^{-2}\cdot kg\cdot s^{-3}=kg\cdot s^{-3}}$

表５．SI 接頭語

乗数	接頭語	記号	乗数	接頭語	記号
10^{24}	ヨタ	Y	10^{-1}	デシ	d
10^{21}	ゼタ	Z	10^{-2}	センチ	c
10^{18}	エクサ	E	10^{-3}	ミリ	m
10^{15}	ペタ	P	10^{-6}	マイクロ	μ
10^{12}	テラ	T	10^{-9}	ナノ	n
10^{9}	ギガ	G	10^{-12}	ピコ	p
10^{6}	メガ	M	10^{-15}	フェムト	f
10^{3}	キロ	k	10^{-18}	アト	a
10^{2}	ヘクト	h	10^{-21}	ゼプト	z
10^{1}	デカ	da	10^{-24}	ヨクト	y

表６．国際単位系と併用されるが国際単位系に属さない単位

名称	記号	SI 単位による値
分	min	1 min=60s
時	h	1h =60 min=3600 s
日	d	1 d=24 h=86400 s
度	°	1°=(π/180) rad
分	’	1’=(1/60)°=(π/10800) rad
秒	”	1”=(1/60)’=(π/648000) rad
リットル	l、L	$\mathrm{1l=1\ dm^3=10^{-3}m^3}$
トン	t	$\mathrm{1t=10^3\ kg}$
ネーパ	Np	1Np=1
ベル	B	1B=(1/2)ln10(Np)

表７．国際単位系と併用されこれに属さない単位で
SI単位で表される数値が実験的に得られるもの

名称	記号	SI 単位であらわされる数値
電子ボルト	eV	$\mathrm{1eV=1.60217733(49)\times10^{-19}J}$
統一原子質量単位	u	$\mathrm{1u=1.6605402(10)\times10^{-27}kg}$
天文単位	ua	$\mathrm{1ua=1.49597870691(30)\times10^{11}m}$

表８．国際単位系に属さないが国際単位系と
併用されるその他の単位

名称	記号	SI 単位であらわされる数値
海里		1海里=1852m
ノット		1ノット=1海里毎時=(1852/3600)m/s
アール	a	$\mathrm{1\,a=1\ dam^2=10^2m^2}$
ヘクタール	ha	$\mathrm{1\,ha=1\ hm^2=10^4m^2}$
バール	bar	$\mathrm{1\,bar=0.1MPa=100kPa=1000hPa=10^5Pa}$
オングストローム	Å	1 Å=0.1nm=10^{-10}m
バーン	b	$\mathrm{1\,b=100fm^2=10^{-28}m^2}$

表９．固有の名称を含むCGS組立単位

名称	記号	SI 単位であらわされる数値
エルグ	erg	$\mathrm{1\ erg=10^{-7}\ J}$
ダイン	dyn	$\mathrm{1\ dyn=10^{-5}N}$
ポアズ	P	$\mathrm{1\ P=1\ dyn\cdot s/cm^2=0.1Pa\cdot s}$
ストークス	St	$\mathrm{1\ St\ =1cm^2/s=10^{-4}m^2/s}$
ガウス	G	1 G ≙ 10^{-4}T
エルステッド	Oe	1 Oe ≙ (1000/4π)A/m
マクスウェル	Mx	1 Mx ≙ 10^{-8}Wb
スチルブ	sb	$\mathrm{1\ sb\ =1cd/cm^2=10^4cd/m^2}$
ホト	ph	$\mathrm{1\ ph=10^4lx}$
ガル	Gal	$\mathrm{1\ Gal\ =1cm/s^2=10^{-2}m/s^2}$

表10．国際単位に属さないその他の単位の例

名称	記号	SI 単位であらわされる数値
キュリー	Ci	$\mathrm{1\ Ci=3.7\times10^{10}Bq}$
レントゲン	R	$\mathrm{1\ R\ =\ 2.58\times10^{-4}C/kg}$
ラド	rad	$\mathrm{1\ rad=1cGy=10^{-2}Gy}$
レム	rem	$\mathrm{1\ rem=1\ cSv=10^{-2}Sv}$
X線単位		$\mathrm{1X\ unit=1.002\times10^{-4}nm}$
ガンマ	γ	$\mathrm{1\gamma=1\ nT=10^{-9}T}$
ジャンスキー	Jy	$\mathrm{1\ Jy=10^{-26}W\cdot m^{-2}\cdot Hz^{-1}}$
フェルミ		$\mathrm{1\ fermi=1\ fm=10^{-15}m}$
メートル系カラット		$\mathrm{1\ metric\ carat\ =\ 200\ mg\ =\ 2\times10^{-4}kg}$
トル	Torr	1 Torr = (101 325/760) Pa
標準大気圧	atm	1 atm = 101 325 Pa
カロリー	cal	
ミクロン	μ	1 μ=1μm=10^{-6}m

（第７版，1998年改訂）